

ENHANCED LIGHT COLLECTION FROM SINGLE TRAPPED
IONS

by
Jonathan David Sterk

A dissertation submitted in partial fulfillment
of the requirements for the degree of
Doctor of Philosophy
(Electrical Engineering)
in The University of Michigan
2011

Doctoral Committee:

Professor Christopher R. Monroe, Co-Chair, University of Maryland
Professor Duncan G. Steel, Co-Chair
Professor Georg A. Raithel
Professor Yaoyun Shi
Professor Kim Winick

“I am a quantum engineer, but on Sundays I have principles.”
—John S. Bell, from his “underground colloquium”, March 1983, as recounted by Nicolas Gisin

© Jonathan David Sterk
All Rights Reserved
2011

To my family.

ACKNOWLEDGEMENTS

I would not be writing this thesis if it weren't for the tremendous amount of support and instruction from many people in my life. Between my family, friends, teachers, and colleagues, I have been blessed to have such wonderful people encourage and challenge me to achieve what I could.

I suppose this whole mess got started in elementary school, where one of my science fair projects was to see if light bent when sent through water. This one little experiment was the first that had gotten me interested in light and optics. This interest resurfaced again during my undergraduate years. The introductory engineering course on lasers and its applications first exposed me to the world of lasers, how they are built, and what they can do. Later, I was quite fortunate to work in Michal Lipson's lab working on silicon nanophotonics where I was exposed to engineering research. I would like to thank the professors at Cornell for supporting my interest in lasers and optics: Michal Lipson, Clif Pollock, Frank Wise, and Chung Tang.

Entering the graduate program at the University of Michigan, I had no idea about atomic physics, quantum information, and quantum optics. Thankfully, Chris Monroe was more than willing to cross fields and hire an engineering student. I could have not asked for a better advisor, as his enthusiasm for the field and keen insight has made working in his lab a pleasure.

One's research experience is not only dependent upon their advisor, but also the

quality of co-workers. The first few years at Michigan, I worked closely with Dan Stick, Winni Hensinger, and Louis Deslauriers. All three are amazing to work with. Dan seemed to have a knack for putting in just the right amount of effort to get something to work without going overboard. I am still in awe of Winni's work ethic and insistence of overnight shipment (which is already a day late). I remember the late nights working with Louis, learning the experiment and how to be safe in the lab.

As I was starting to take over the experiment, I worked with Yisa Rumala and Simcha Korenblit, two younger graduate students. As I was teaching them the experiment, they taught me patience. Those last few months at Michigan, I worked with Ming-Shien Chang where we both learned much about Raman transitions.

In Maryland, I was blessed to spend time with Peter Maunz whose expertise and knowledge were invaluable. Almost anytime I had a question regarding optics or had difficulty doing something related to the experiment, Peter knew not only how to do it, but also do it correctly the first time around.

Much of my experimental apparatus at Maryland would not have been possible without Andrew Manning. His dedicated work in the design of the chamber, as well as the machining, soldering, and all the little things that are needed helped the experiment immensely. Likewise, much of what I accomplished would not have been possible without Le Luo, whose hard work really paid off when the experiment was working. Although we got into many arguments, he is a very creative scientist who is always thinking about future experiments.

Although I did not work closely with everyone in the lab, I would like to thank them all for being around to bounce ideas off of, discuss theory, and their experimental suggestions: Mark Acton, Boris Blinov, Kathy-Anne Brickman, Wes Campbell,

Andrew Chew, Susan Clark, Dan Cook, Shantanu Debnath, Emily Edwards, Brian Fields, Paul Haljan, Dave Hayes, David Hucul, Rajibul Islam, Kihwan Kim, Rudy Kohn Jr., Aaron Lee, Kenny Lee, Patty Lee, Martin Madsen, Dzmitry Matsukevich, David Moehring, Steve Olmschenk, Liz Otto, Qudisa Quraishi, Jim Rabchuck, Yisa Rumala, Crystal Senko, Mark Yeo, and Kelly Younge.

Finally, I would like to thank my family and friends. I don't think I would have survived graduate school without them. My parents gave me encouragement when I came to terms with experimental failure. My brother would remind me that very few people understand what I am studying and have the opportunity to work in the field. I am indebted to them for making me the person who I am giving me the opportunity to study the interactions of light and matter.

TABLE OF CONTENTS

DEDICATION	ii
ACKNOWLEDGEMENTS	iii
LIST OF TABLES	viii
LIST OF FIGURES	ix
LIST OF APPENDICES	xi
ABSTRACT	xii
CHAPTER	
I. Introduction	1
II. The atom–photon interface	6
2.1 Atomic qubits: YbII	7
2.2 Photonic qubits	10
2.3 Linking atoms together for quantum networks	16
III. Light collection	22
3.1 Collection of light with a parabolic mirror	23
3.2 Optical Cavities	27
3.3 Enhanced Spontaneous Emission	32
3.4 Cavity QED	35
3.5 Photon emission from an optical cavity	40
IV. Ion trapping	55
4.1 Basis functions for the electric potential	56
4.2 Motion of a charged particle in an ion trap	59
4.3 Ion trap for enhanced light collection	65
V. Experimental System	76
5.1 UHV Chamber	77
5.2 Laser system	81
5.3 Imaging System	83
5.4 Mirror Experiment	85
5.5 Optical Cavity	86

5.6 Ion Cavity Experiment	93
VI. Outlook and Conclusions	100
APPENDICES	103
BIBLIOGRAPHY	114

LIST OF TABLES

Table

3.1	Relevant Cavity Parameters	31
3.2	Gaussian mode parameters for an optical cavity	32
4.1	Steps for the lithographic process in order to pattern gold on one side of the substrate.	70
5.1	Spot-welding parameters	79
5.2	Cavity QED parameters for the initial finesse and degraded finesse.	94

LIST OF FIGURES

Figure

2.1	Neutral ytterbium energy levels	8
2.2	Ytterbium ion energy levels	11
2.3	Initialization and detection of the ytterbium qubit	12
2.4	Protocols to generate atom-photon entanglement	13
2.5	Interference of photons on a beamsplitter	17
3.1	Geometry for an ion at the focus of a parabolic mirror	24
3.2	Reflected modes from a parabolic mirror	25
3.3	Mode overlap of σ transition with Gaussian mode	26
3.4	Signal flow diagram for an optical cavity	29
3.5	Energy levels of an excited two-level system in cavity	40
3.6	Plots of emission probability for an initially excited atom coupled to a cavity	44
3.7	Emission rates and collection efficiencies for a driven two-level system	47
3.8	Protocol to generate polarization-entangled photons in a cavity.	49
3.9	Photon collection efficiency for entanglement protocol	50
3.10	Illustration of generating frequency and time-bin qubits from an optical cavity.	53
4.1	Ideal hyperbolic electrode shape for 3D quadrupole	58
4.2	Stability diagram for 3D quadrupole trap	63
4.3	Ion trap geometry for the double fork trap	67
4.4	RF Ponderomotive potential for electrode spacing $2x_0 = 180 \mu\text{m}$	68
4.5	Helical quarter wave resonator used in ion trap experiments.	73
4.6	Calibration of the HP8472B Crystal detector	74

4.7	Secular frequency versus bias voltage	75
4.8	Voltage efficiency versus separation	75
5.1	The ion-cavity vacuum chamber	78
5.2	Schematic of laser layout for the cavity experiment.	82
5.3	Imaging system used in the experiments.	84
5.4	Image of ion and mirror	86
5.5	Measured transfer function of the piezo in a voltage divider configuration.	89
5.6	Piezo impedance	90
5.7	Cavity full width at half-maximum measurement	91
5.8	Layout of cavity coupling, detection, and locking	92
5.9	Initial observation of ion fluorescence from a cavity	98
5.10	Measurement of ion fluorescence from the cavity versus cavity detuning	99

LIST OF APPENDICES

Appendix

A. Simulation Code	104
------------------------------	-----

ABSTRACT

ENHANCED LIGHT COLLECTION FROM SINGLE TRAPPED IONS

by
Jonathan David Sterk

Co-Chairs: Christopher R. Monroe and Duncan G. Steel

Long-range transport of quantum information across a network is most readily achieved through the use of photons as the information carriers. The nodes of such a quantum network are most naturally a quantum memory or information processor, which typically do not rely upon photonic qubits. Realizing a large-scale distributed quantum network therefore requires an efficient interface between the two physical manifestations of the quantum information.

The most promising platform for realizing a quantum computer is the manipulation of trapped atomic ions, as this system has demonstrated all the fundamental requirements to realize a quantum computer. Additionally, trapped ions possess long coherence times necessary for quantum memories. The interface between atomic and photonic qubits relies on a high photon emission rate into the collected solid angle. Most methods of photon collection for quantum networks use a high numerical aperture microscope objective, which only collects on the order of 1% of all the emitted photons. This results in a small probability of successfully linking two quantum nodes.

In this work, I present the design, simulation, and implementation of a trapped ion cavity QED system capable of improving the photon collection efficiency. A single ytterbium ion is coupled to a high-finesse optical cavity. The photon scatter rate into the cavity mode is enhanced by a factor of 130 over the free-space scatter rate into the cavity solid angle. This represents the first step towards realizing a protocol to entangle the polarization of an emitted photon to the Zeeman sublevels of the ion with high photon collection efficiency. Simulations of the experimental system indicate that with an optical cavity up to 4% of the light emitted by the ion can be collected.

CHAPTER I

Introduction

Quantum technologies are the application and control of complex quantum systems for practical endeavors. The ability to detect and manipulate quantum states of atoms, photons and other quantum systems has developed alongside their application in computation [1], cryptography [2] and metrology [3].

In 1994, Peter Shor introduced a factoring algorithm utilizing quantum features [4]. This discovery provided an impetus to the practical realization of quantum technologies. That same year, Cirac and Zoller proposed the use of individual trapped ions for quantum computation [5]. By this time, the ability to control and manipulate ions from atomic clockwork had progressed to the point where the first quantum gate between trapped ions was performed later that year [6].

The Cirac–Zoller proposal for quantum information processing with trapped ions considered a string of trapped ions in a linear array. The information is stored in the internal states of the ions, such as hyperfine ground states. The qubits are initialized through optical pumping techniques and read out via state dependent fluorescence detection. Single qubit gates can be achieved through direct application of microwave radiation at the qubit frequency, or through stimulated Raman transitions.

A crystal of N ions has $3N$ normal modes. Typically, two dimensions are tightly

confined such that the ions are in a linear chain. Quantum gates between ions uses these normal modes as a quantum bus. The Cirac–Zoller gate uses one normal mode to be in the ground vibrational state, and transfers coherence from one ion onto that mode. This mode then can interact with another ion to acquire a spin-dependent phase shift, and then be mapped back onto the original ion. Other gates exist for ions, but they all rely upon the Coulomb coupling and spin-dependent forces.

Trapped ions are not the only platform for quantum computation. Other possible implementations include trapped neutral atoms in optical lattices [7, 8, 9], superconducting circuits with Josephson junctions [10, 11], quantum dots [12, 13], and photons [14, 15]. In general, a multipurpose quantum computer must satisfy what are known as the DiVincenzo criteria [16]:

1. A scalable physical system with well characterized qubits.
2. The ability to initialize the state of the qubits to a simple fiducial state, such as $|000\dots\rangle$.
3. Long relevant decoherence times, much longer than the gate operation time.
4. A “universal” set of quantum gates.
5. A qubit-specific measurement capability.

In plain language, the five requirements amount to the ability to have a quantum system that can be initialized to a known state, manipulated with a complete set of quantum gates faster than information loss, and reliably read out the information at the end. In principle, ion traps accomplish all of DiVincenzo’s requirements. Coherence times of trapped ion qubits can be greater than several seconds [17]. Initialization and readout fidelities are greater than 98% [18].

In order to scale trapped a ion system to a large number of qubits, Kielpinski et

al. proposed a scalable architecture based upon shuttling individual ions [19]. In this proposal, stored ions will be shuttled into a register for manipulation and shuttled out when not in use. In this manner, large number of qubits can be manipulated while only addressing a small number of ions at a time. Towards this goals has been the development of microfabricated ion traps [20, 21, 22, 23, 24], and shuttling routines [25, 26, 27].

Quantum networks provide an alternative approach to scaling trapped ion systems [28]. Rather than interacting ions with their mutual Coulomb force, quantum gates are mediated through a photonic channel. Work on this method has demonstrated ion–photon entanglement [29], interference of spontaneously emitted photons [30], remote entanglement [31], Bell-inequality violation [32], teleportation [33], and photon-mediated quantum gates [34]. A general quantum network consists of a set of quantum nodes that interact with each other across a quantum channel. The nodes are quantum systems that can be of various size. Single qubits at nodes can be used to study Bell inequalities or generate large scale entangled states [28]. A pair of qubits as nodes with a linear topology can be used as a quantum repeater. A full scale quantum computer at the nodes can realize distributed quantum computation.

In order to realize such a network, a couple requirements must be met. DiVincenzo specified two additional requirements for a quantum system for quantum communication [16]. In order to transfer quantum information across long distances, the quantum system must have:

1. The ability to interconvert stationary and flying qubits.
2. The ability to faithfully transmit flying qubits between specified locations.

Here, stationary and flying qubits are the carriers of quantum information either inside a processor or sent long distances. Generally, photons are the qubit of choice

to send long distances, and any quantum system to be used for a quantum network must have a reliable photonic interface.

Realization of a quantum network based upon trapped ions at the nodes relies upon a two-step process involving either one or two photons. First, probabilistic generation of entanglement between the ion and the photon with probability P_{ap} is created through photon scattering. Then, the subsequent entanglement swapping performed by photon interference and measurement projects the ions onto an entangled state [35].

The probability of successfully generating a remote entangled pair of ions from a two-photon process is

$$P_{suc} = \vartheta [\eta_{det} P_{ap}]^2 = \vartheta [\eta_{det} p_e p_c p_t]^2,$$

where ϑ is the probability detecting a Bell state of the two photons, η_{det} is the photon detection efficiency, p_e is the probability of generating the desired entangled atom–photon pair, p_c is the efficiency of collecting the emitted photon by the optical system, and p_t is the transmission efficiency of the entire system, including fiber coupling. For a two-photon process, the probability of generating atom–photon entanglement is squared.

In current experiments [36, 32, 33, 34], the collection efficiency, p_c is the dominant cause of failure to generate entanglement. The photons are collected with a microscope objective of numerical aperture $NA = 0.23$ and subtends 1.3% of the solid angle. Since an atom emits a photon into the whole solid angle (shaped by its radiation pattern), the collection efficiencies of these experiments is on the order of 1%.

In order to improve the probability to successfully entangle remote pairs of ions, the collection efficiency must be improved. This thesis presents the efforts and

progress towards an efficient method to collect photons entangled with individual ions. The next chapter provides a more detailed description of the atomic and photonic qubits, and protocols to entangle remote atoms. Chapter 3 details theoretical models to improve the collection efficiency. Then an overview of ion traps is presented in Chapter 4. These tools are then applied to an experimental apparatus (Chapter 5), where we demonstrate an improved collection of photons. Finally, is an brief outlook of a scalable atom–photon network for quantum information processing (Chapter 6).

CHAPTER II

The atom–photon interface

Singly ionized ytterbium is an excellent choice for quantum information processing and networking. The 171 isotope has nuclear spin $I = 1/2$ making it feasible to prepare and use the magnetic field insensitive clock states as qubit states. The atomic structure also makes it feasible to generate ion–photon entanglement for quantum networks. The hyperfine splitting of the ground state is at 12.643 GHz, allowing for high fidelity readout of the state [37, 17]. Additionally the D1 line of the ytterbium ion is at 369 nm allowing the use of optical fibers, an essential component for an ion-based quantum network.

Photons are the typical carrier for quantum information across long distances as they can in principle travel far with little attenuation and decoherence, making them good quantum information carriers to link the nodes in a quantum network.

This chapter presents the atomic physics of the ytterbium ion and how it can be used for quantum networks. Several photonic qubit encodings are described and how they can be entangled with an atomic qubit. Finally, generation of entanglement between the atomic qubits via photon interference and detection is discussed.

2.1 Atomic qubits: YbII

2.1.1 Photoionization The electronic configuration of neutral ytterbium is $[\text{Xe}]4f^{14}6s^2$, containing two valence electrons in the 1S_0 level. The ionization continuum is 6.254 eV (198 nm) above the ground state [38]. The atom has a strong line at 751 526.6 GHz (398.9113 nm) between the ground state to the 1P_1 level, as seen in figure 2.1. Because the 1P_1 state is slightly below half the ionization energy, a single laser at 398.9113 nm is unable to drive a two-photon absorption to the continuum. In our experiments, we ionize the neutral atoms through the use of the Doppler cooling beam at 811 291 GHz (369.525 nm), which carries a valence electron from the 1P_1 to the continuum with 0.2 eV of energy.

Due to its low vapor pressure the background partial pressure of ytterbium in the vacuum chamber is not enough to load ions. Therefore a high flux of neutral atoms is created through use of an atomic oven. The oven is a stainless steel tube of diameter 0.5 mm and length 20 mm. One end is clamped closed and a kapton wire is spot-welded via a Constantan flag at the end to provide an electrical lead. The tube is halfway packed with ytterbium metal. The oven is attached to the vacuum chamber by a titanium mount holding the open end.

Heating the ovens creates a beam of ytterbium atoms that is directed towards the ion trap. The oven must be oriented such that the path of the atoms intersects the ion trap. This can be tricky, as the atomic beam may be quite collimated, which requires excellent placement of the oven.

Due to the temperatures required to create an atomic flux, nearby oxygen can react with the metal, forming an oxide layer over the oven. While this is typically not an issue, novel oven designs can be susceptible to this failure mechanism.

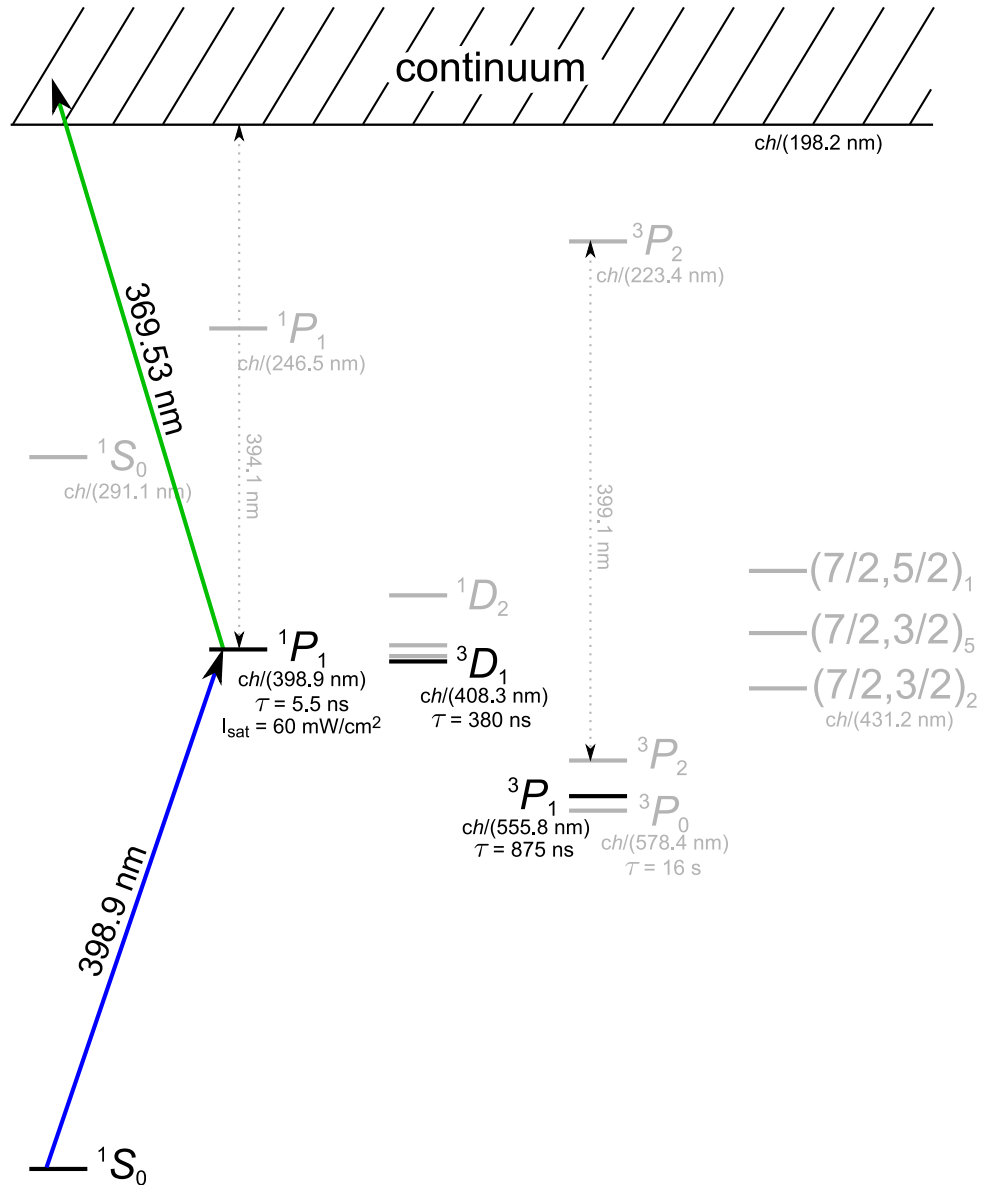


Figure 2.1: Energy levels of neutral ytterbium (to scale). Energies are quoted from the ground state in wavelengths from Ref [38], while lifetimes and saturation intensities are given in references [39, 40, 41, 42]. Driven transitions in the experiment are illustrated with solid lines. (Image courtesy of Steve Olmschenk)

The ovens are tested by placing them in a bell jar and pumping down to 10^{-6} Torr. They are electrically connected to a feedthrough whereby current can be run. Because ytterbium is known to stick to glass walls, creating a high optical density spot, we characterize how long it takes to create a visible spot on the side of a bell jar. Running the oven at 5 A for 30 min was enough to create a visible spot of ytterbium. The typical operating point is at 2.7 A, where no spot was observed over several hours.

2.1.2 Atomic structure A partial energy level diagram of singly ionized ytterbium is illustrated in Figure 2.2. Doppler cooling, detection, and optical pumping are all performed on the $^2S_{1/2} \leftrightarrow ^2P_{1/2}$ transition at 811 291 GHz. The $^2P_{1/2}$ manifold has a 0.5% probability of decaying to a low-lying $^2D_{3/2}$ level which has a 52.7 ms lifetime [17]. The population in this state is repumped to the ground state through 935 nm light at 320 572 GHz. This infrared beam drives the transition $^2D_{3/2} \leftrightarrow ^3[3/2]_{1/2}$. Occasionally, ion is found in the $^2F_{7/2}$ level, which can be cleaned out with 638.6 nm light (469 452 GHz).

For quantum information purposes, the odd isotope $^{171}\text{Yb}^+$ is used. This isotope has a nuclear spin $I = 1/2$ providing two ground state hyperfine manifolds ($F = 0, 1$), split by 12.643 GHz. The hyperfine structure is amenable to preparation and detection of first-order magnetic field insensitive qubit states (known colloquially as clock states). These states are $^2S_{1/2} |F = 0, m = 0\rangle$ and $^2S_{1/2} |F = 1, m = 0\rangle$.

While the 171 isotope of ytterbium is used for quantum information, the experiments in this thesis are done with the more abundant 174 isotope which has no nuclear spin. The lack of hyperfine structure makes it a good testbed for light collection techniques. Both the $^2S_{1/2}$ and $^2P_{1/2}$ levels have total angular momentum $J = 1/2$ with Zeeman sublevels $m_J = \pm 1/2$. In the excited state, the ion has a 2/3 probability to emit a σ -polarized photon and 1/3 probability to emit a π -polarized

photon.

2.1.3 Manipulation of qubits Although the 171 isotope is not used in the experiments in Chapter V, the protocols described in this chapter and the next rely upon the ability to initialize and detect the quantum state of the $^{171}\text{Yb}^+$ ion.

The $^{171}\text{Yb}^+$ ion can be initialized with high fidelity (98%) to the $^2\text{S}_{1/2} |0, 0\rangle$ level through optical pumping techniques. Light resonant with the $^2\text{S}_{1/2}, F = 1 \longleftrightarrow ^2\text{P}_{1/2}, F = 1$ transition excites the atom to the $^2\text{P}_{1/2}, F = 1$ manifold (figure 2.3a). This level can decay to the $^2\text{S}_{1/2} |0, 0\rangle$ level, which is not depopulated by the light.

To detect the state of the qubit, light resonant with the $^2\text{S}_{1/2}, F = 1 \longleftrightarrow ^2\text{P}_{1/2}, F = 0$ transition is applied (figure 2.3b). If the ion is in the $^2\text{S}_{1/2} |1, 0\rangle$ level, it scatters many photons. However, if the ion is in the $^2\text{S}_{1/2} |0, 0\rangle$ level, it rarely scatters photons. By detecting the number of photons scattered in the detection window, the state of the qubit can be determined with high fidelity ($> 98\%$).

Single qubit rotations can be driven by application of microwave radiation at the hyperfine splitting of 12.643 GHz or through stimulated Raman transitions.

2.2 Photonic qubits

Single photons arise naturally from excitations of atoms through energy transfer between the atom and the electromagnetic field. A single photon from a spontaneous emission event has a decaying exponential wave packet centered at the transition frequency. There are four degrees of freedom of interest to encode quantum information in a spontaneously emitted photon: photon number, polarization, frequency, time-bin [35].

These various encodings rely upon the ability for an ion to coherently move atomic excitations into the electromagnetic field. The atomic excitations are generated by

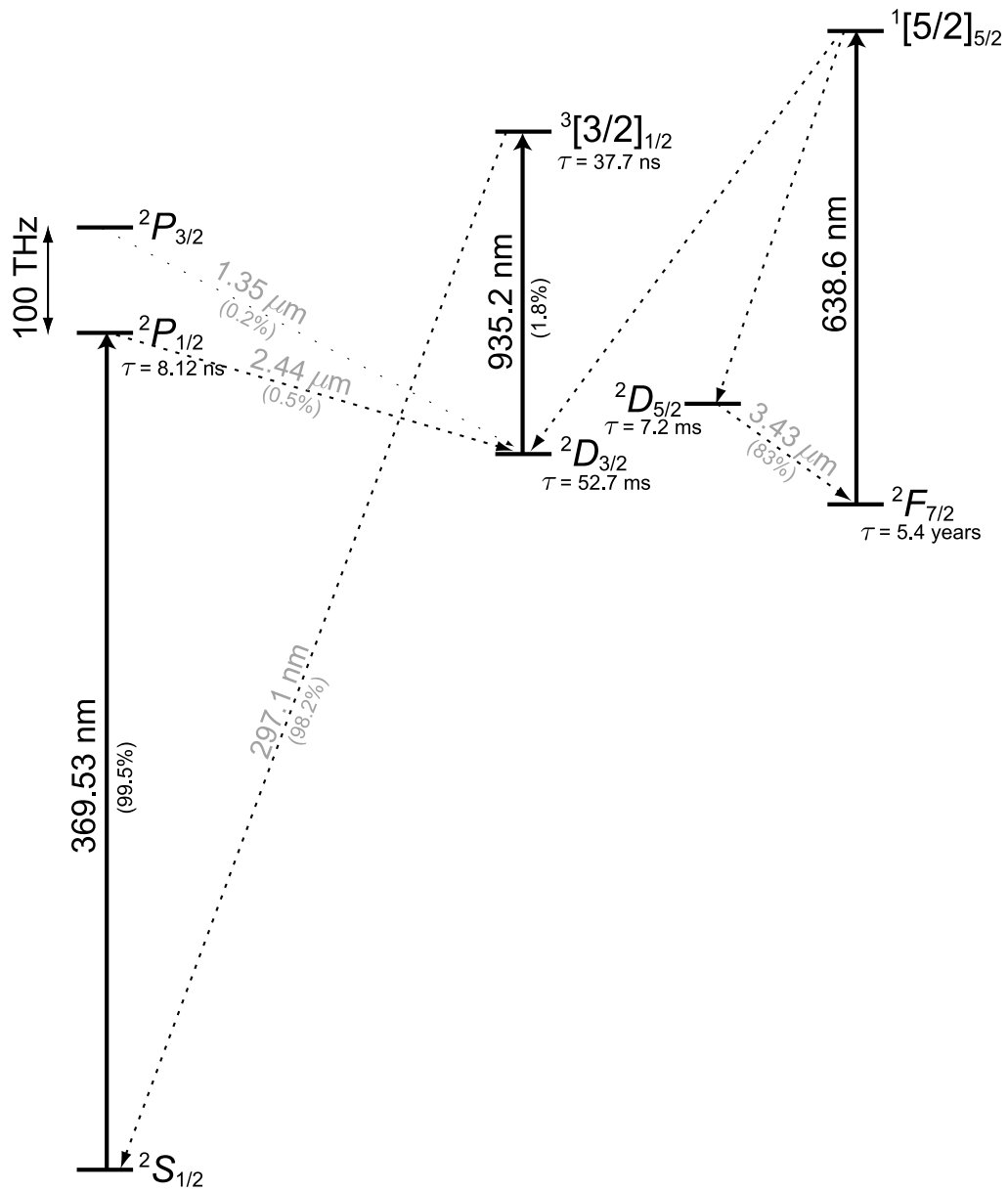


Figure 2.2: Relevant energy levels of YbII (to scale). Driven transitions are given by the solid lines, while decay paths are indicated by dotted lines. The branching ratios for the transitions are given in parenthesis. Wavelengths of the decays are given in Ref. [38], while the lifetimes are given in references [43, 44, 45, 46] and branching ratios from references [47, 43]. (Image courtesy of Steve Olmschenk)

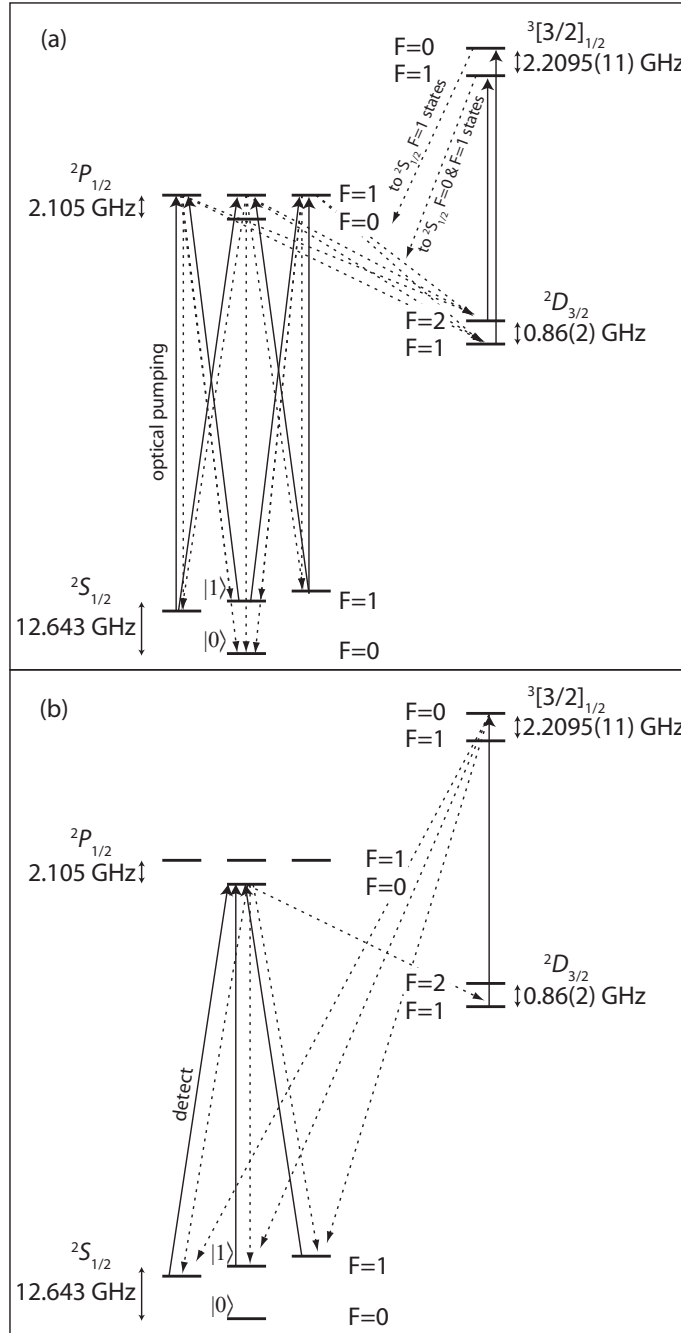


Figure 2.3: Initialization and detection of $^{171}\text{Yb}^+$. **(a)** Initialization of the ion to the $^2S_{1/2} |0,0\rangle$ level is achieved through optical pumping techniques. Application of resonant light from the $F = 1$ to $F' = 1$ manifolds populates $^2P_{1/2} F' = 1$, which has a decay path to $^2S_{1/2} |0,0\rangle$. The light is off-resonant from any transition to exit this state. **(b)** Detection is achieved by driving the $F = 1$ to $F' = 0$ transition. If the ion is in the $F = 1$ manifold, it scatters many photons and appears bright. However, the $F = 0$ level is off-resonant and cannot be driven due to selection rules. Therefore, it doesn't scatter light and appears dark.

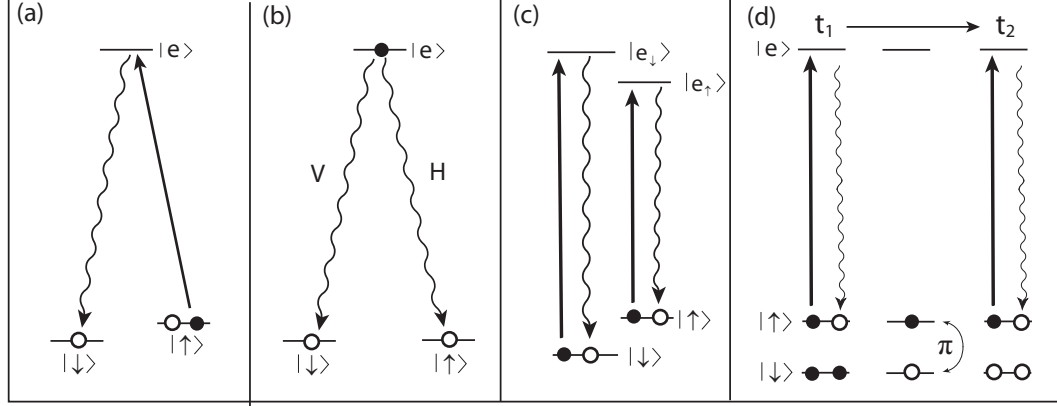


Figure 2.4: Protocols to generate atom–photon entanglement. Here, black dots represent the initial state, while white dots indicate the final state. Solid lines illustrate driven transition, while wiggly lines are decays. **(a) Photon number** The atom scatters a photon from a laser pulse with some probability, transferring the atomic state to the final. **(b) Polarization** An initially excited atom has two possible decay paths connected through two orthogonal polarizations of light. **(c) Frequency** An atom in an initial arbitrary superposition is coherently excited to the two excited states. The selection rules preserve the initial coherence. Upon decay, a photon is emitted whose frequency is entangled with the atom. **(d) Time-bin** Initially the atom is in an arbitrary superposition, and only one state is excited. After decay back to the initial state, the qubit states are flipped by a π -pulse. The atom again is excited and decays. The emission time of the photon defines the photonic qubit and is generally entangled with the atomic levels

scattering of photons of resonant or near-resonant light. If there are two distinct scattering channels correlated with two orthogonal photonic states, the ion–photon system is described by

$$|\Psi_{ap}\rangle = c_{\uparrow} |\uparrow\rangle |P_{\uparrow}\rangle + c_{\downarrow} |\downarrow\rangle |P_{\downarrow}\rangle. \quad (2.1)$$

Here, $|\uparrow\rangle$ and $|\downarrow\rangle$ represent the atomic qubit state, and $|P_{\uparrow}\rangle$ and $|P_{\downarrow}\rangle$ are the orthogonal states of the photonic qubit.

2.2.1 Photon number Entanglement between internal levels of the ion and the photon number is generated with either weak scattering or through vacuum Rabi oscillation in a strongly coupled atom–photon system. Figure 2.4a illustrates scheme to generate photon number qubits in the weak scattering case. Suppose a three-level atom in a lambda configuration is initially prepared in one of its ground states, $|\uparrow\rangle$.

A laser pulse is scattered by the atom, such that there is a small probability p_e that the atomic state is transferred to $|\downarrow\rangle$. After scattering, the final state of the atom–photon system is

$$|\Psi_{ap}\rangle = \sqrt{1-p_e} |\uparrow\rangle |0\rangle + \sqrt{p_e} |\downarrow\rangle |1\rangle. \quad (2.2)$$

For an ion strongly coupled to a single mode of the electromagnetic field, weak scattering is not necessary. A fully excited atom will undergo Rabi oscillations between the states $|\uparrow\rangle |0\rangle$ and $|\downarrow\rangle |1\rangle$. An initial superposition of the atom $(\alpha |\uparrow\rangle + \beta |\downarrow\rangle) \otimes |0\rangle$ evolves under the Jaynes–Cummings Hamiltonian (equation 3.30)

$$|\Psi_{ap}\rangle = \alpha |\downarrow\rangle |0\rangle + \beta (\cos gt |\uparrow\rangle |0\rangle - \sin gt |\downarrow\rangle |1\rangle). \quad (2.3)$$

To be useful in a quantum network, the qubit must be initially in $|\uparrow\rangle$ and coupled to a cavity for a well-specified time, leaving the ion–photon system in an maximally entangled state [48, 49]. Chapter III provides more detail regarding the theory of cavity QED systems and generation of atom–photon entanglement.

This coherent interaction between the atom and the electromagnetic field forms the basis for cavity QED approaches to quantum computation [50, 51, 52], where the single mode of the cavity acts as a quantum bus to transfer information between atoms.

2.2.2 Polarization An atom initially in an excited state $|e\rangle$ can spontaneously decay to two ground states $|\uparrow\rangle$ and $|\downarrow\rangle$ (Figure 2.4b). If the two ground states are near-degenerate and differ in their magnetic quantum number, then the polarization of the emitted photon is entangled with the two ground levels of the ion. Denoting the two orthogonal polarizations as H and V , the final atom–photon state is given by

$$|\Psi_{ap}\rangle = \sqrt{p_\uparrow} |\uparrow\rangle |1_H 0_V\rangle + \sqrt{p_\downarrow} |\downarrow\rangle |0_H 1_V\rangle. \quad (2.4)$$

Here, p_\uparrow and p_\downarrow are the probabilities of decaying through those two channels. These probabilities are given by the Clebsch–Gordan coefficients between the ground states and the excited state.

2.2.3 Frequency There are two means of generating entanglement between the frequency of the emitted photon and the ion. The first is similar to the polarization entanglement described above, where an initial excited state $|e\rangle$ can decay to two well-resolved ground levels (such as different hyperfine manifolds). While this method can be utilized to generate a quantum network, it cannot support a quantum gate operation.

The second method is to utilize two excited levels $|e_\uparrow\rangle$ and $|e_\downarrow\rangle$. In this configuration, the selection rules of the atomic transitions only allow $|\downarrow\rangle \leftrightarrow |e_\downarrow\rangle$ and $|\uparrow\rangle \leftrightarrow |e_\uparrow\rangle$. The atom is initially prepared in an arbitrary superposition state $\alpha|\uparrow\rangle + \beta|\downarrow\rangle$. A laser pulse with bandwidth large enough to cover both allowed transitions coherently excites the atom to $\alpha|e_\uparrow\rangle + \beta|e_\downarrow\rangle$. Since there is only one allowed transition, after the ion decays back to the ground state, the coherence is preserved, emitting a photon that is entangled with the two ground states

$$|\Psi_{ap}\rangle = \alpha|\uparrow\rangle|1_r0_b\rangle + \beta|\downarrow\rangle|0_r1_b\rangle. \quad (2.5)$$

In this configuration, the entanglement preserves the quantum information initially stored in the atom. Here, r and b denote the two frequency modes, r for the relatively redder transition and b for the relatively bluer transition. These two states are well resolved when $\omega_b - \omega_r \gg \gamma$, where ω_b and ω_r are the two frequencies and γ is the linewidth of the transition.

2.2.4 Time-bin The arrival (or emission) times of photons can be used as a qubit encoding and can be entangled with the ion. A spontaneously emitted photon has a bandwidth given by the linewidth of the atomic transition, and can be described as

a localized wavepacket. Considering two particular time bins at t_1 and t_2 , a photon can be in a superposition of wavepackets in the two bins. These qubit state are well-resolved when $e^{-\gamma|t_2-t_1|} \ll 1$.

Generation of the entanglement is illustrated in Figure 2.4d. The protocol begins with an initial superposition $\alpha |\uparrow\rangle + \beta |\downarrow\rangle$. In this configuration, only the transition $|\uparrow\rangle \leftrightarrow |e\rangle$ is allowed. A pulse of light drives the atom to the $|e\rangle$ state, which spontaneously decays at time t_1 . After the spontaneous decay, the state is $\alpha |\uparrow\rangle |1_{t_1}\rangle + \beta |\downarrow\rangle |0_{t_1}\rangle$. Next, a π pulse is applied to the qubit states, flipping the spins. The state is now $-\alpha |\downarrow\rangle |1_{t_1}\rangle + \beta |\uparrow\rangle |0_{t_1}\rangle$. Finally, another excitation pulse drives the atom to $|e\rangle$, which decays at time t_2 . After this decay, the atom–photon state is given by

$$|\Psi_{ap}\rangle = \beta |\uparrow\rangle |0_{t_1} 1_{t_2}\rangle - \alpha |\downarrow\rangle |1_{t_1} 0_{t_2}\rangle \quad (2.6)$$

2.3 Linking atoms together for quantum networks

These atom–photon entanglement schemes discussed above are the building blocks to construct distributed quantum networks. Entanglement of a qubit with a photon creates a quantum channel that can be used to link remote qubits together in a network.

In order to link two atoms together, their respective photons are interfered on a 50 : 50 beamsplitter as shown in figure 2.5. In contrast to post-selected entanglement schemes, where verification of entanglement requires the destruction of the entangled state, coincidence detection of photons after the beamsplitter heralds the creation of an entangled state between atoms. Photon detection destroys only the photonic degree of freedom, allowing the atomic states to be projected into an entangled state. Such heralded entanglement schemes are useful as one knows when an entangled state

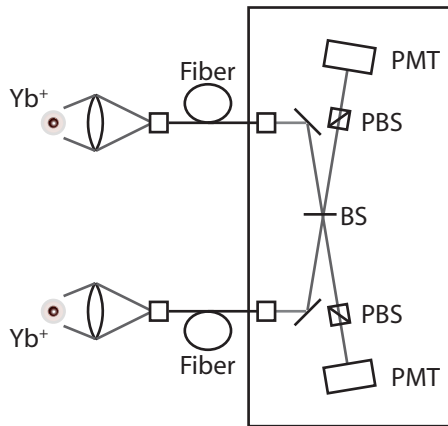


Figure 2.5: Two photons arrive at a 50 : 50 beamsplitter. If the photons are identical, no coincidence detections will occur. However, if the photons are distinguishable, there is a 50% probability for a coincidence detection. The photonic state resulting in a coincidence detection is $|\psi^-\rangle$. For photons initially entangled with their respective ions, the beamsplitter plus coincidence detection results in an entanglement swap, leaving the ions entangled.

is created without having to destroy it. This heralded entanglement technique serves as the chief resource for constructing photon-mediated quantum networks.

There are two types of heralded entanglement, distinguished by the number of photons emitted by the two atoms [53]. Type I entanglement describes the case when between the two atoms only one photon is emitted. Detection of the photon after the beamsplitter creates an entangled state as the which-path information of the photon is lost. The other method, type II, relies on both atoms emitting entangled photons. Interference of the photons allows one to select only photons that are not identical. Again the which-path information is lost, leaving the atoms in an entangled state.

Using the formalism for the scattering matrix of a mirror in Chapter III, the

photon annihilation operators obey

$$\hat{a}_3 = \frac{i}{\sqrt{2}}(\hat{a}_1 - i\hat{a}_2) \quad (2.7)$$

$$\hat{a}_4 = \frac{1}{\sqrt{2}}(\hat{a}_1 + i\hat{a}_2) \quad (2.8)$$

which is equivalent to an effective angular momentum rotation operator with an effective total angular momentum $J = N/2$, where $N = n_1 + n_2$ is the total number of photons entering the beamsplitter [54, 36]. In the Fock state formalism, the action of a beamsplitter is

$$|n\rangle_1 |m\rangle_2 \mapsto e^{-i\chi\hat{J}_y} |n\rangle_1 |m\rangle_2, \quad (2.9)$$

where $\hat{J}_y = -i(\hat{a}_1^\dagger\hat{a}_2 - \hat{a}_1\hat{a}_2^\dagger)/2$. The rotation angle is $\chi = \pi R$, where R is the reflectivity of the beamsplitter.

2.3.1 Type I This method of heralded entanglement utilizes number state qubits for the photons. Lasers pulses are applied to two atoms A and B such that each have a small probability $p_e \ll 1$ to scatter a photon and transfer its state to equation 2.2. The joint state between both atom-photon systems is

$$\begin{aligned} |\Psi_{apap}\rangle &= |\Psi_{ap}\rangle_A \otimes |\Psi_{ap}\rangle_B = (1 - p_e) |\uparrow\uparrow\rangle_{AB} |00\rangle_{AB} \\ &+ \sqrt{p_e(1 - p_e)} \left(|\uparrow\downarrow\rangle_{AB} |01\rangle_{AB} + e^{i\phi} |\downarrow\uparrow\rangle_{AB} |10\rangle_{AB} \right) \\ &+ p_e |\downarrow\downarrow\rangle_{AB} |11\rangle_{AB}. \end{aligned} \quad (2.10)$$

The relative phase $\phi = \Delta k \Delta x$, where Δk is the wave-vector difference between the excitation laser and collected photons and Δx is the optical path length difference from the atoms to the beamsplitter. After the beamsplitter, the output state containing one photon is

$$|\Psi_{apap}\rangle = \left(|\uparrow\downarrow\rangle_{AB} - e^{i\phi} |\downarrow\uparrow\rangle_{AB} \right) |01\rangle_{AB} + \left(|\uparrow\downarrow\rangle_{AB} + e^{i\phi} |\downarrow\uparrow\rangle_{AB} \right) |10\rangle_{AB} \quad (2.11)$$

This equation indicates that when one detector clicks, the atomic state is projected onto

$$|\Psi_{aa}\rangle = |\uparrow\downarrow\rangle_{AB} \pm e^{i\phi} |\downarrow\uparrow\rangle_{AB} \quad (2.12)$$

where the sign is determined by which detector clicks.

The probability to successfully generate entanglement with a type I procedure is

$$P_I = 2\eta_{QE}P_{ap} = 2\eta_{QE} [p_e p_c p_t] \quad (2.13)$$

where η_{QE} is the quantum efficiency of the detector, and $P_{ap} = p_e p_c p_t$ is the probability of generating, collecting, and transmitting to a detector the atom–photon entanglement. Note that one limit to the fidelity of this scheme is the probability that two photons were scattered but only photon detected. Given typical operating values from the remote entanglement experiments [33], the probability of successfully generating entanglement with a type I scheme would be $6 \times 10^{-4} \times p_e$, where $p_e \ll 1$ is the probability for a way scattering event.

Type I entanglement relies upon interferometric stability of the optical paths. If the fluctuations in the phase ϕ are large, it is easy to show that the overall state is not entangled [55]. One important source of decoherence is the atomic recoil from the absorption and emission of a photon. This recoil indicates which atom scattered the photon, leaving the system unentangled [56, 57]. In the Lamb–Dicke limit, where $\eta^2 \bar{n} \ll 1$, the resulting entanglement fidelity is $F = 1 - 4\eta^2(\bar{n} + 1/2)$ [58], where the Lamb–Dicke parameter $\eta = \Delta k \sqrt{\hbar/2m\omega}$ for an atom of mass m in a trap of frequency ω . Here, \bar{n} is the average number of thermal quanta of motion in the trap. To overcome this limit on fidelity, one can either collect the forward scattering (where $\Delta k = 0$) or confine the ions deep within the Lamb–Dicke regime where the recoil is small.

2.3.2 Type II Interferometric stability is difficult to achieve experimentally. Type II schemes bypass this requirement by two photon interference. The interferometric phase $k\Delta x$ then becomes common mode. Hence, type II is more robust to noise and has been successfully demonstrated in experiments [31, 32, 33, 34].

Consider two independent atoms, A and B . After each generates a photon entangled with its spin (equation 2.1), the overall quantum state of the two atom–photon system is

$$|\Psi_{apap}\rangle = \left(\alpha_A |\uparrow\rangle_A |P_\uparrow\rangle_A + \beta_A |\downarrow\rangle_A |P_\downarrow\rangle_A\right) \otimes \left(\alpha_B |\uparrow\rangle_B |P_\uparrow\rangle_B + \beta_B |\downarrow\rangle_B |P_\downarrow\rangle_B\right) \quad (2.14)$$

$$= |\tilde{\phi}^+\rangle_{aa} |\phi^+\rangle_{pp} + |\tilde{\phi}^-\rangle_{aa} |\phi^-\rangle_{pp} + |\tilde{\psi}^+\rangle_{aa} |\psi^+\rangle_{pp} + |\tilde{\psi}^-\rangle_{aa} |\psi^-\rangle_{pp} \quad (2.15)$$

The second equality collects terms into the maximally entangled Bell states $|\phi^\pm\rangle_{pp}$ and $|\psi^\pm\rangle_{pp}$. Associated with these states are the atomic states given by

$$|\phi^\pm\rangle_{pp} = \frac{1}{\sqrt{2}} \left(|P_\uparrow\rangle_A |P_\uparrow\rangle_B \pm |P_\downarrow\rangle_A |P_\downarrow\rangle_B\right) \quad (2.16)$$

$$|\psi^\pm\rangle_{pp} = \frac{1}{\sqrt{2}} \left(|P_\uparrow\rangle_A |P_\downarrow\rangle_B \pm |P_\downarrow\rangle_A |P_\uparrow\rangle_B\right) \quad (2.17)$$

$$|\tilde{\phi}^\pm\rangle_{aa} = \frac{1}{\sqrt{2}} \left(\alpha_A \alpha_B |\uparrow\rangle_A |\uparrow\rangle_B \pm \beta_A \beta_B |\downarrow\rangle_A |\downarrow\rangle_B\right) \quad (2.18)$$

$$|\tilde{\psi}^\pm\rangle_{aa} = \frac{1}{\sqrt{2}} \left(\alpha_A \beta_B |\uparrow\rangle_A |\downarrow\rangle_B \pm \beta_A \alpha_B |\downarrow\rangle_A |\uparrow\rangle_B\right) \quad (2.19)$$

$$(2.20)$$

As a consequence of the quantum interference at the beamsplitter, photons only emerge from the different ports of the beamsplitter if they are in the $|\psi^-\rangle_{pp}$ state [59, 60, 61, 62]. Therefore, upon coincidence detection, the final atomic state is

$$|\Psi_{aa}\rangle = \frac{\alpha_A \beta_B |\uparrow\downarrow\rangle_{AB} - \beta_A \alpha_B |\downarrow\uparrow\rangle_{AB}}{\sqrt{|\alpha_A \beta_B|^2 + |\beta_A \alpha_B|^2}} \quad (2.21)$$

Since this protocol requires two photons, only polarization, frequency, and time-bin qubits are available. However, the coefficients α and β for polarization qubits

are fixed by the Clebsch–Gordan coefficients for that particular transition. Alternatively, for frequency and time-bin qubits, the coefficients are given by the initial superpositions of the state. In this case, the type II protocol performs a quantum gate $\frac{1}{2}\sigma_z^A(1 - \sigma_z^A\sigma_z^B)$.

With time-bin qubits, one is able to also detect the $|\psi^+\rangle_{pp}$ state. For time-bin qubits, $|P_\uparrow\rangle = |0_{t_1}, 1_{t_2}\rangle$ and $|P_\downarrow\rangle = |1_{t_1}, 0_{t_2}\rangle$. In this case, $|\psi^+\rangle_{pp}$ state corresponds to photons going to the same detector, but at different times. In principle, if the time bins are well resolved, one can detect this photonic state.

The success rate for type II entanglement is

$$P_{II} = \vartheta(\eta_{QE}P_{ap})^2. \quad (2.22)$$

Here, ϑ is the probability to detect a particular photonic Bell state. Typically, only one of the four photonic Bell states is detectable ($|\psi^-\rangle$), giving $\vartheta = 1/4$. With well resolved time-bins for time-bin qubits, the state $|\psi^+\rangle$ can in principle be detected, and thus $\vartheta = 1/2$. Because this protocol requires two successful creations of an atom–photon entangled pair, the success probability scales as P_{ap}^2 .

In this analysis, the relative path length difference Δx was neglected. Such a difference in path length results in a relative phase factor $e^{i\Delta\omega\Delta x/c}$ in the final state, equation 2.21. For frequency qubits $\Delta\omega$ is the frequency different between the photonic qubits. As such, $\Delta\omega/c \ll k$, and thus type II entanglement is typically much more robust than type I schemes.

These entanglement protocols have been demonstrated in several experiments [31, 32, 33, 34]. However, in each of these experiments, the probability to successfully generate the atomic entanglement is on the order of 1×10^{-8} . This low success probability is dominated by the efficiency of collecting light from trapped the trapped ions.

CHAPTER III

Light collection

For type II entanglement protocols, the probability to successfully generate entanglement between two quantum nodes scales quadratically with the photon collection efficiency, p_c . Current experiments utilize a microscope objective of numerical aperture 0.23 to collect the light [31, 32, 33, 34]. Such an objective subtends only 1.3% of the solid angle, and is therefore the primary limitation for a practical trapped ion quantum network. Current implementations have a success probability of 2.2×10^{-8} . Running experiments at 70 ks results in generation of remote entangled pairs every 12 minutes [34]. Clearly this success rate is much too slow to generate useful quantum networks as the time to connect nodes is much longer than the measured coherence time of the qubits [17].

Attempts to improve the collection of light from trapped ions have centered primarily on the use of a spherical mirror [63, 64, 65] or the placement of multimode fiber near the ion [66]. A parabolic mirror should be able to collect upwards of 95% of the light emitted by the ion [67]. Shu and coworkers have observed collection efficiencies up to 10% with an ion trapped at the focus of a spherical mirror [64].

Optical cavities have been used extensively as sources of single photons [68, 69, 70, 71, 72, 73]. These methods generally use cavity-stimulated Raman transitions

where the vacuum field of the cavity mode stimulates photon emission into the cavity. Atom–photon entanglement and photon–photon entanglement with cavities have been considered both theoretically [74, 75] and experimentally [76, 77]. Trapped ions are attractive for cavity QED experiments as they have long storage times in the trap and have the ability to be well-placed in the cavity mode [78, 79]. In a cavity-assisted Raman configuration, 50% of the light can be collected [80], and single photons can be deterministically generated [73].

This chapter first describes how light collection from a parabolic mirror can be used for the entanglement protocols described in Chapter II. The rest of the chapter is devoted to the use of an optical cavities for enhancement of light collection. After a review of optical cavities, the Purcell effect and cavity QED theory is built up; culminating in an entanglement generation protocol that uses an optical cavity to collect the photon. Throughout, simulations are performed using numbers from an experimental apparatus described in Chapter V.

3.1 Collection of light with a parabolic mirror

Consider an ion placed at the focus of a parabolic mirror with the quantization axis along the symmetry axis of the paraboloid. The coordinate system is illustrated in Figure 3.1. Taking the focus to be the origin, the paraboloid is defined by $z_m(\rho) = \frac{\rho^2}{4f} - f$. The distance from the ion to the reflecting surface is $(\rho^2 + 4f^2)/4f$.

Prior to reflection, the optical fields of emitted photons associated with the three possible transitions are

$$\mathbf{E}_{\ell=1,m=0} = \frac{ie^{ikr}}{r} \sqrt{\frac{3}{16\pi}} \sin \theta \hat{\boldsymbol{\theta}} \quad (3.1)$$

$$\mathbf{E}_{\ell=1,m=\pm 1} = \frac{ie^{ikr}}{r} e^{\pm i\varphi} \sqrt{\frac{3}{16\pi}} (\pm \cos \theta \hat{\boldsymbol{\theta}} + i \hat{\boldsymbol{\varphi}}). \quad (3.2)$$

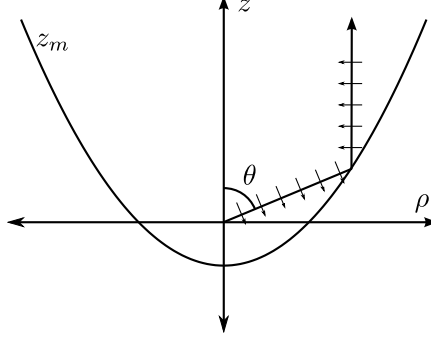


Figure 3.1: Geometry for an ion at the focus of a parabolic mirror. The azimuthal angle φ is not shown. A ray that is polarized in the $\hat{\theta}$ direction is in the $-\hat{\rho}$ direction after reflection.

After reflection, the resulting wavefronts are flat, thus the complex exponential becomes $e^{ikr} \mapsto e^{ik(z+2f)}$. From the geometry illustrated in Figure 3.1, light that was polarized in $\hat{\theta}$ will have polarization $-\hat{\rho}$, while $\hat{\varphi}$ is unchanged. The mirror maps the polar angle θ to the radial coordinate ρ . From trigonometry and the equation for the surface of the mirror,

$$\sin \theta = \frac{4f\rho}{\rho^2 + 4f^2} \quad (3.3)$$

$$\cos \theta = \frac{\rho^2 - 4f^2}{\rho^2 + 4f^2} \quad (3.4)$$

Then, the emitted fields from the ion leaving the mirror are

$$\mathbf{E}_{10} \longrightarrow -\frac{i4f}{\rho^2 + 4f^2} \sqrt{\frac{3}{16\pi}} \frac{4f\rho}{\rho^2 + 4f^2} \hat{\rho} \quad (3.5)$$

$$\mathbf{E}_{1\pm 1} \longrightarrow \pm \frac{i4f}{\rho^2 + 4f^2} e^{\pm i\varphi} \sqrt{\frac{3}{16\pi}} \left(-\frac{\rho^2 - 4f^2}{\rho^2 + 4f^2} \hat{\rho} \pm i\hat{\varphi} \right), \quad (3.6)$$

which is in agreement with Lindlein et al [67].

The irradiance and polarization distribution of these fields are illustrated in Figure 3.2. The $\Delta m = 0$ transition leads to radially polarized doughnut mode, while the $\Delta m = \pm 1$ transitions have a Lorentzian-like profile, yet have a complicated polarization pattern. The polarization of the $\Delta m = \pm 1$ transition is circular at the center and becomes more elliptical until it reaches purely azimuthal polarization at

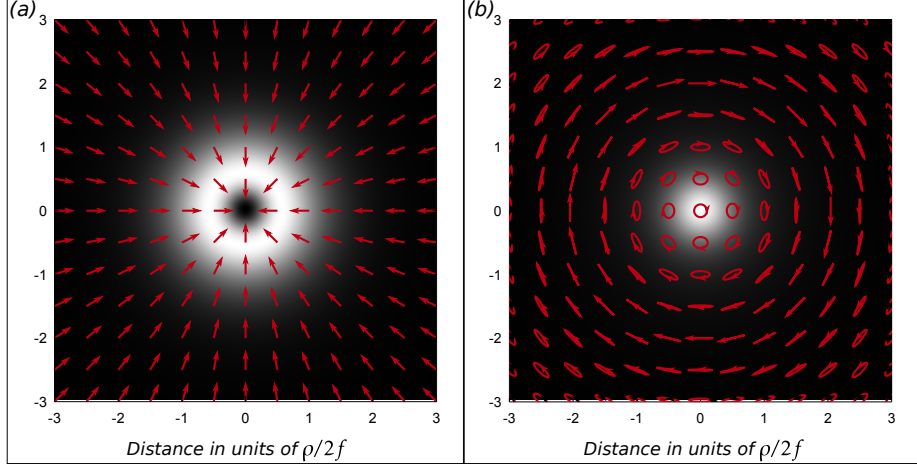


Figure 3.2: Irradiance and polarization plot of the reflected light from (a) a $\Delta m = 0$ transition and (b) a $\Delta m = \pm 1$ transition.

$\rho = 2f$. Past this point, it becomes elliptical of the other handedness and gradually becomes more circular as $\rho \rightarrow \infty$.

Implementations of the type II protocol rely upon fiber coupling in order to clean up the spatial mode. To get an indication how well these modes can be coupled into a single mode fiber the mode overlap with a generic Gaussian mode can be calculated. The overlap between a Gaussian mode $\mathbf{G}(\rho) = e^{-\rho^2/w^2}(a\hat{\mathbf{x}} + b\hat{\mathbf{y}})$ and the reflected field is defined by

$$T_{\ell,m} = \frac{\left| \int_0^{2\pi} \int_0^{\rho_0} d\varphi d\rho \rho \mathbf{E}_{\ell,m} \cdot \mathbf{G} \right|^2}{\int_0^{2\pi} \int_0^{\infty} d\varphi d\rho \rho \mathbf{E}_{\ell,m} \cdot \mathbf{E}_{\ell,m} \int_0^{2\pi} \int_0^{\infty} d\varphi d\rho \rho \mathbf{G} \cdot \mathbf{G}}, \quad (3.7)$$

where ρ_0 is the maximum radial extent of the mirror.

Assuming the irradiance and polarization of the Gaussian mode only depends on ρ , then the only dependence on φ in T_{10} is the unit vector $\hat{\rho}$, causing the integral to vanish. Therefore, without additional optics, light from a $\Delta m = 0$ transition cannot be coupled into a fiber aligned with the axis of symmetry. The overlap integral, $T_{1,\pm 1}$

can be evaluated, giving a fiber coupling efficiency

$$T_{1,\pm 1} = \frac{3}{2} \left(\frac{2f}{w} \right)^6 |a \pm ib|^2 e^{2(2f/w)^2} \left| \Gamma(-1, (2f/w)^2) - \Gamma(-1, (\rho^2 + (2f)^2)/w^2) \right|^2, \quad (3.8)$$

where $\Gamma(a, t_0)$ is the incomplete Gamma function, defined as

$$\Gamma(a, t_0) = \int_{t_0}^{\infty} dt t^{a-1} e^{-t}$$

Equation 3.8 shows that the light from a σ^+ (σ^-) transition couples to the left (right) handed polarization mode of the fiber. In the limit of an infinite extent paraboloidal mirror $\rho_0 \rightarrow \infty$, the mode overlap approaches a limit near 50%. Figure 3.3 illustrates the value of the overlap integral versus focal length and mirror extent.

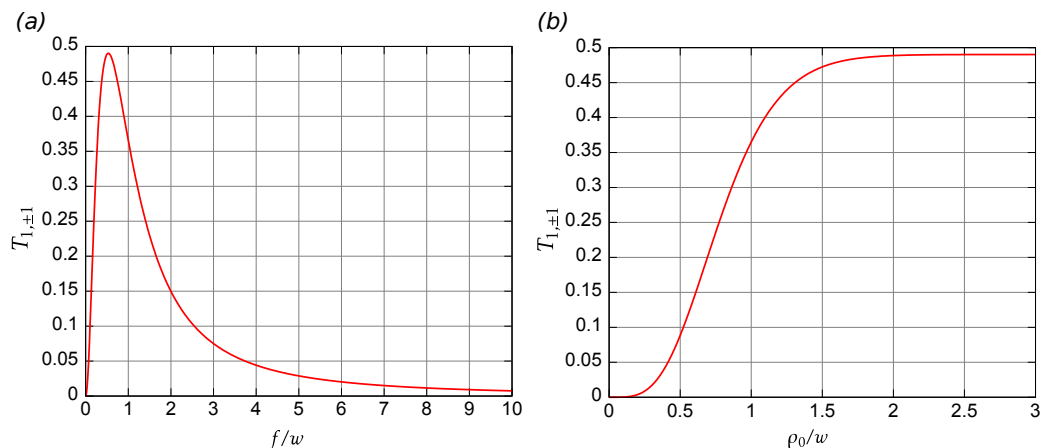


Figure 3.3: Evaluation of the overlap integral for a σ transition with a circularly polarized Gaussian mode. **(a)** Mode overlap as a function of parabolic mirror focus. The peak occurs when $f = f_{max} \approx 0.532w$. **(b)** Mode overlap as a function of extent ρ_0 of parabolic mirror when $f = f_{max}$. The overlap asymptotes to ≈ 0.49 for $\rho_0 > 3w$.

In principle, all four protocols described in Chapter II can be realized. Weak excitation (number qubits) simply relies upon the ability to collect light. Polarization qubits are possible because the $\Delta m = \pm 1$ transitions couple to different polarization modes of a Gaussian beam, allowing polarization discrimination. Frequency qubits

can be realized by utilizing only one polarization of light, as is performed in reference [31]. The ion can be initially excited to the ${}^2P_{1/2} |F = 1, m_F = -1\rangle$ level, and the mirror can collect the σ^- polarized photons.

To use the initial coherence of the ion to perform quantum gates, $\Delta m = 0$ transitions must be used. This is the case for gates with frequency qubits as well as time-bin qubits. Correction to the $\Delta m = 0$ transition light and filtering of the other transitions must be performed prior to coupling the light into a fiber.

3.2 Optical Cavities

Optical cavities are an important part of any atomic physics experiment, as they can be used for laser frequency stabilization and monitoring. Additionally, high finesse optical cavities have been playing an increasingly important role in quantum optics and quantum information [48, 49, 81, 52, 82]. The presence of optical mirrors changes the electromagnetic mode structure such that a single mode can be strongly coupled to an atom. The mode structure can lead to altered spontaneous emission rates [83]. This section reviews several of the essential parameters for optical cavities that play an important role in cavity QED experiments.

3.2.1 S matrix for a mirror A mirror is a two-port network with a corresponding S-matrix

$$S_m = \begin{pmatrix} r_{11} & t_{12} \\ t_{21} & r_{22} \end{pmatrix}.$$

Here, r_{ii} is the electric field reflection coefficient on the i -th port, and t_{ij} is the electric field transmission from port j to port i [84, 85]. Due to reciprocity, $t_{ij} = t_{ji}$. For lossless mirrors, the scattering matrix must be unitary, which requires $|r_{11}| = |r_{22}|$, and an overall π phase shift between transmission and reflection. The two conventions

often used are the purely real and complex symmetric forms

$$S_m = \begin{pmatrix} r & t \\ t & -r \end{pmatrix} \quad S_m = \begin{pmatrix} r & it \\ it & r \end{pmatrix},$$

where r and t are both real, and satisfy the condition $|r|^2 + |t|^2 = 1$. The power reflection and transmission coefficients are $R = |r|^2$ and $T = |t|^2$. For mirrors with total absorption and scattering losses ℓ , power conservation results in

$$R + T + \ell = 1$$

For simplicity, the complex-symmetric form will be used. By suitable choice of reference planes, the scattering matrix for a mirror/beamsplitter can always be placed into this form [85].

3.2.2 Transfer Functions An optical cavity is formed by placing two mirrors of reflectivities $R_{1,2}$ a distance L apart (see figure 3.4a). With incident fields $E_{1,2}$ on the two sides of the cavity, the circulating field \tilde{E}_c and output fields $\tilde{E}_{3,4}$ are easily found from the signal flow diagram (figure 3.4b) to be

$$\tilde{E}_c = \left(\frac{it_1}{1 - r_1 r_2 e^{i2kL}} \right) \tilde{E}_1 + \left(\frac{ir_1 t_2 e^{ikL}}{1 - r_1 r_2 e^{i2kL}} \right) \tilde{E}_2 \quad (3.9)$$

$$\tilde{E}_3 = \left(\frac{-t_1 t_2 e^{i2\pi\nu L/c}}{1 - r_1 r_2 e^{i4\pi\nu L/c}} \right) \tilde{E}_1 + \left(r_2 - \frac{r_1 t_2 t_2 e^{i4\pi\nu L/c}}{1 - r_1 r_2 e^{i4\pi\nu L/c}} \right) \tilde{E}_2 \quad (3.10)$$

$$\tilde{E}_4 = \left(r_1 - \frac{t_1 t_1 r_2 e^{i4\pi\nu L/c}}{1 - r_1 r_2 e^{i4\pi\nu L/c}} \right) \tilde{E}_1 - \left(\frac{t_1 t_2 e^{i2\pi\nu L/c}}{1 - r_1 r_2 e^{i4\pi\nu L/c}} \right) \tilde{E}_2 \quad (3.11)$$

where \tilde{E}_c is defined just to the right of mirror 1, heading towards mirror 2.

Most uses of optical cavities only excite the cavity from one side and use the opposite port for output. Setting $\tilde{E}_2 = 0$ in equation 3.9 gives the transfer function for the circulating field given a signal originating on port 1 of the cavity:

$$H_c(\nu) = \frac{\tilde{E}_c}{\tilde{E}_1} = \frac{i\sqrt{T_1}}{1 - R e^{i4\pi\nu L/c}}, \quad (3.12)$$

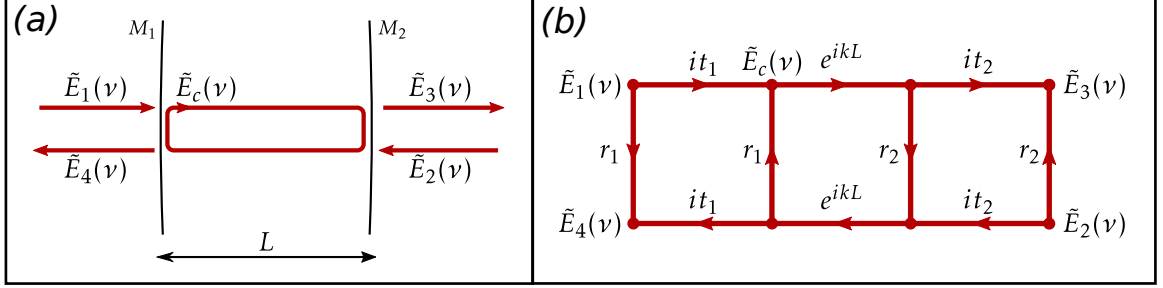


Figure 3.4: **(a)** A cavity is formed from two mirrors M_1 and M_2 a distance L apart. Incident fields are $\tilde{E}_{1,2}$ from the left and right of the cavity. The output fields are $\tilde{E}_{3,4}$, while the circulating field \tilde{E}_c is defined just to the right of M_1 heading towards M_2 . **(b)** The corresponding signal flow diagram for an optical cavity.

where $k = 2\pi\nu/c$ and $R = \sqrt{R_1 R_2} = r_1 r_2$. Note R is the geometrical mean reflectivity of the two mirrors.

Likewise, the transfer functions for the transmitted and reflected fields (\tilde{E}_3 and \tilde{E}_4) are

$$H_t(\nu) = \frac{\tilde{E}_3}{\tilde{E}_1} = \frac{-\sqrt{T_1 T_2} e^{i2\pi\nu L/c}}{1 - R e^{i4\pi\nu L/c}} \quad (3.13)$$

$$H_r(\nu) = \frac{\tilde{E}_4}{\tilde{E}_1} = \left(\sqrt{R_1} - \frac{\sqrt{T_1 T_1 R_2} e^{i4\pi\nu L/c}}{1 - R e^{i4\pi\nu L/c}} \right) \quad (3.14)$$

Taking the inverse Fourier transform of the transfer functions (equations 3.12, 3.14, and 3.13) gives the impulse response functions for the circulating, reflected, and transmitted fields of the cavity. The impulse response function for the circulating field is

$$h_c(t) = it_1 \sum_{n=0}^{\infty} R^n \delta(t - n/\nu_{fsr}) \Theta(t), \quad (3.15)$$

where $\nu_{fsr} = c/2L$ is the free-spectral range and $t_{rt} = 1/\nu_{fsr}$ is the time it takes for light to make a round trip in the cavity. Here, the reflection and transmission coefficients are assumed constant as they are generally flat across tens of nanometers. $\Theta(t)$ is the unit step function, ensuring causality. This impulse response function for the circulating field intuitively makes sense, as an impulse into the cavity undergoes

transmission it_1 , then an infinite number of reflections. Each reflection takes a time $1/\nu_{fsr}$. Similar expressions can be written for the reflected and transmitted signals.

For monochromatic excitation of frequency ν_L , the ratio of the circulating to incident irradiance is the modulus square of the value of the transfer function. This can be cast into two forms

$$|H_c(\nu_L)|^2 = \frac{I_c}{I_1} = \frac{B}{1 + F \sin^2(\pi\nu_L/\nu_{fsr})} = \sum_n \frac{\kappa^2}{\kappa^2 + (2\pi(\nu_L - n\nu_{fsr}))^2}, \quad (3.16)$$

where $B = T_1/(1 - R)^2$ is the cavity buildup factor, and $F = 4R/(1 - R)^2$ is known as the coefficient of finesse. The second form can be derived by using the convolution property of the Fourier transform and performing the convolution $h_c(t) * h_c^*(-t)$ and transforming back. The second equality shows that each mode of the cavity is a Lorentzian of full width $\Delta\nu_{fwhm} = \kappa/\pi$. For a good cavity, there is negligible overlap between various modes.

Two important experimental parameters of an optical cavity are the free-spectral range and the full width at half-maximum. From these, the cavity finesse, photon lifetime, and overall losses can be known. The total losses of the cavity are $\mathcal{L} = T_1 + T_2 + \ell_1 + \ell_2$, resulting in $R = e^{-\mathcal{L}/2}$. The relevant cavity parameters are listed in table 3.1, as well as the experimentally realized values.

3.2.3 Gaussian modes of the cavity In order for the optical field inside a cavity to build up, there must be a stable spatial mode profile. After a round trip, the spatial distribution of the light must be proportional to the initial shape. For an open Fabry–Pérot resonator under the paraxial approximation, the stable mode functions are approximately Hermite–Gaussian modes [84].

Ray transfer matrix analysis can be used to determine the shape of the Gaussian modes. For a Gaussian mode, after a round trip, the complex radius of curvature, q ,

Parameter	Symbol	Expression	Value
Reflectivity of mirror i	R_i	$r_i^2 \approx e^{-(T_i + \ell_i)}$	0.9982, 0.9975
Total Losses	\mathcal{L}	$T_1 + T_2 + \ell_1 + \ell_2$	4278 ppm
Cavity Length	L		2126 μm
Mean reflectivity	R	$\sqrt{R_1 R_2} = r_1 r_2 \approx e^{-\mathcal{L}/2}$	0.9978
Free Spectral Range	ν_{fsr}	$c/2L$	70.503 GHz
Round-trip time	t_{rt}	$1/\nu_{fsr}$	14.2 ps
Finesse	\mathfrak{F}	$\nu_{fsr}/\Delta\nu_{fwhm} \approx 2\pi/\mathcal{L} \approx \frac{\pi\sqrt{R}}{1-R}$	1469
Coefficient of Finesse	F	$4R/(1-R)^2 \approx (2\mathfrak{F}/\pi)^2$	874365
Full-width at half-max	$\Delta\nu_{fwhm}$	$2\nu_{fsr} \arcsin(1/\sqrt{F})/\pi \approx \kappa/\pi$	48 MHz
Electric field decay rate	κ	$\nu_{fsr} \ln(1/R) = c\mathcal{L}/4L$	$150.8 \times 10^6 \text{ s}^{-1}$
Photon lifetime	τ_{ph}	$1/2\kappa$	3.3 ns
Buildup	B	$\frac{T_1}{(1-R)^2}$	65.7

Table 3.1: Table of relevant cavity parameters. The experimental values are derived from the cavity constructed in Chapter V.

of the beam must be identical to the input. Hence, by the ABCD law,

$$q = \frac{Aq + B}{Cq + D} \implies q = \frac{A - D}{2C} \pm \frac{\sqrt{(A - D)^2 + 4BC}}{2C} \quad (3.17)$$

where $ABCD$ are the matrix elements of the round trip ray transfer matrix. For a symmetric cavity, where two mirrors have the same radius of curvature \mathcal{R} , the solution for q at the center of the cavity is

$$q(z = 0) = iz_R = i\frac{1}{2}\sqrt{L(2\mathcal{R} - L)} \quad (3.18)$$

where at the focus ($z = 0$), q is equal to the Rayleigh range. The waist of the Gaussian mode is $w_0 = \sqrt{\lambda z_R/\pi}$.

A Gaussian standing wave in a cavity with m anti-nodes has the mode function

$$u_m(r, z) = \frac{w_0}{w(z)} e^{-r^2/w^2(z)} \cos \left[kz - \frac{kr}{2R(z)} - \arctan \left(\frac{z}{z_R} \right) + (m - 1)\frac{\pi}{2} \right]$$

For a near planar cavity where $L \ll z_R$, the mode function can be approximated as

$$u_m(r, z) = e^{-r^2/w_0^2} \cos [kz + (m - 1)\pi/2]. \quad (3.19)$$

where the static phase $(m - 1)\pi/2$ determines if there is a node or anti-node at the middle of the cavity. The volume of the mode is then calculated as

$$V = \int d^3\mathbf{r} |u_m(r, z)|^2 = \frac{\pi}{4} w_0^2 L \quad (3.20)$$

Beam Parameter	Symbol	Expression	Value
Rayleigh Range	z_R	$\frac{1}{2}\sqrt{L(2\mathcal{R}-L)}$	5044 μm
Waist	w_0	$\sqrt{\frac{\lambda z_R}{\pi}}$	24.36 μm
Mode Volume	V	$\pi w_0^2 L/4$	990 850 μm^3
Divergence	θ	$\lambda/\pi w_0$	4.829×10^{-3} rad = 0.277°
Solid Angle	$\Delta\Omega_{\text{cav}}$	$2\lambda^2/\pi w_0^2$	1.465×10^{-4} sr

Table 3.2: Table of Gaussian parameters for a symmetric Fabry–Pérot cavity. The experimental values are derived from the cavity constructed in chapter V.

The factor of $1/4$ in the mode volume makes intuitive sense: the irradiance of the mode has a radius of $w_0/\sqrt{2}$, so the mode has an area of $\pi w_0^2/2$. The cosine-squared averages to $L/2$, leading to a volume as seen in equation 3.20.

The divergence of the Gaussian mode is $\theta = \lambda/\pi w_0$. The solid angle subtended by the cavity mode is

$$\Delta\Omega_{\text{cav}} = 4\pi(1 - \cos(\theta)) \approx 2\pi\theta^2 = \frac{2\lambda^2}{\pi w_0^2} \quad (3.21)$$

Table 3.2 summarizes the relevant beam Gaussian mode parameters for an optical cavity.

3.3 Enhanced Spontaneous Emission

In 1946, E. M. Purcell noted that the spontaneous emission rate of a nuclear magnetic moment can be increased significantly by coupling it to a high Q electrical circuit [83]. The spontaneous emission rate would be increased by a factor

$$2C = \frac{3Q\lambda^3}{4\pi^2 V}, \quad (3.22)$$

where V is the mode volume of the resonator, and C is the single-atom cooperativity. In fact, this effect occurs for any dipole oscillator coupled to a high- Q resonator. Similarly, when the cavity mode is off resonant, spontaneous emission can be inhibited [86, 87, 88], and has been used to increase the T_1 time of superconducting qubits by at least an order of magnitude [89].

Early development of the theory was carried out by Bloembergen and Pound [90], Power [91], Morawitz [92], Barton [93], and Stehle [94]. Experimentally, the first observations of modified radiation rates were done by Feher et. al. at microwave frequencies [95], and by Drexhage et. al. in the visible [96]. Gabrielse and Dehmelt observed the first inhibition of spontaneous emission by coupling a trapped electron to a microwave cavity [87].

It is interesting to note that identical results can be derived from purely classical arguments [97, 98, 92], where a dipole antenna is placed inside a cavity. Here, the radiation induces an external force on the dipole's motion, analogous to a friction force. Alternatively, it can be seen as a cooperative effect where the image dipole oscillators behind the mirror add coherently along the cavity axis [98, 99].

Spontaneous emission was first introduced by Einstein [100] in a treatment of a gas of atoms in thermal equilibrium with the electromagnetic field. Through detailed balancing, he was able to arrive at Planck's radiation law. In 1930, Weisskopf and Wigner were able to calculate the spontaneous emission rate by applying perturbation theory to the interaction between atoms and quantized field modes [101]. This perturbative solution relies upon summing over all available photon modes. The presence of the mirrors alters the density of photon states, and hence the emission rate. Below, we follow Heinzen [88, 102] to derive the enhanced spontaneous emission rate. The spontaneous emission rate γ from an atom in an excited state is

$$\gamma = 2\pi \int \sum_{\lambda} \frac{|\boldsymbol{\mu} \cdot \boldsymbol{\epsilon}_{k,\lambda}|^2}{\hbar^2} \frac{\hbar\omega_k}{2\pi\epsilon_0 V} \delta(\omega_0 - \omega_k) \rho(\omega_k, \mathbf{k}) d\Omega_k d\omega_k. \quad (3.23)$$

Here, $\boldsymbol{\mu} = \langle e | \hat{\boldsymbol{\mu}} | g \rangle$ is the dipole moment matrix element between the two states, and $\rho(\omega_k, \mathbf{k})$ is the density of photon states. The density of states for free-space is $\rho_{\text{free}}(\omega) = V\omega^2/(2\pi)^3 c^3$.

An open optical cavity modifies the density of states for \mathbf{k} -vectors in the solid

angle subtended by the cavity mode, $\Delta\Omega_{\text{cav}}$ (defined in equation 3.21). Outside the subtended solid angle, the density of states is that of free space. Hence, the density of states is

$$\rho_{\text{cav}}(\omega) = \begin{cases} \rho_{\text{free}}(\omega)\ell(\omega), & \mathbf{k} \text{ in } \Delta\Omega_{\text{cav}} \\ \rho_{\text{free}}(\omega), & \mathbf{k} \text{ not in cavity} \end{cases} \quad (3.24)$$

Here, the lineshape function $\ell(\omega)$ is normalized such that the average mode density over a free spectral range is that same as free space. Using this density of states yields a spontaneous emission rate

$$\gamma_{\text{cav}} = \gamma(1 - f) + \gamma f \ell(\omega_0), \quad (3.25)$$

where f is a function of the subtended solid angle of the cavity mode, and is given by $f = (3/8\pi)\Delta\Omega_{\text{cav}}$ for a small solid angle. The first term describes the spontaneous emission rate out the side of the cavity, while the second describes the emission rate into the cavity mode. On resonance, one can show that the second term is equal to the Purcell factor (equation 3.22), and is twice the single atom cooperativity. Neglecting the reduction in emission rate due to the solid angle, the ratio of scattered light into the cavity mode to the total scatter rate is $2C/(1 + 2C)$, and is equivalent to the laser beta factor [103].

From a geometrical standpoint, for an atom scattering photons at a rate Γ_{sc} , the photon scatter rate into the cavity mode is simply $2C\Gamma_{\text{sc}}$. The photon collection efficiency is then

$$p_c = \frac{T_2}{\mathcal{L}} \frac{2C}{1 + 2C} \quad (3.26)$$

This equation holds well when the ion is very weakly coupled to the cavity and the cavity is quite lossy. That is, the cavity can be treated as a small perturbation.

The fraction T_2/\mathcal{L} is the outcoupler efficiency, and it is the ratio of light that is

transmitted through the outcoupler to the other cavity loss mechanisms.

3.4 Cavity QED

The effect of enhanced spontaneous emission is due to the cavity mode and appears once one traces out the photonic loss channels (see, for example [104]). When the atom is coupled well enough to the cavity such that the atom has a non-negligible probability to re-absorb the emitted photon, the cavity cannot be treated as a first-order perturbation. Instead, the quantum nature of the cavity must be taken into account. Additionally, for the quantum networking protocols described in the previous chapter, the quantum nature of the mode is essential.

3.4.1 Interaction Hamiltonian The interaction of a two-level atom with a single mode of electromagnetic radiation was first given by Jaynes and Cummings [105]. Under the dipole approximation, the interaction Hamiltonian is $\hat{H}_{int} = -\hat{\boldsymbol{\mu}} \cdot \hat{\mathbf{E}}$. Here, both the dipole moment and the electric field are operators. The electric field operator for a single mode is [106]

$$\hat{\mathbf{E}} = \hat{\mathbf{E}}^{(+)} + \hat{\mathbf{E}}^{(-)} = i\sqrt{\frac{\hbar\omega_c}{2\epsilon_0 V}}u(\mathbf{r})\epsilon\hat{a} - i\sqrt{\frac{\hbar\omega_c}{2\epsilon_0 V}}u(\mathbf{r})\epsilon^*\hat{a}^\dagger \quad (3.27)$$

where V is the mode volume, $u(\mathbf{r})$ is the spatial eigenmode of the optical cavity (equations 3.20 and 3.19). In a two level approximation, the dipole moment operator $\hat{\boldsymbol{\mu}}$ can be written as

$$\hat{\boldsymbol{\mu}} = \boldsymbol{\mu}\hat{\sigma} + \boldsymbol{\mu}^*\hat{\sigma}^\dagger \quad (3.28)$$

where $\hat{\sigma} = |g\rangle\langle e|$ is the atomic lowering operator and $\boldsymbol{\mu} = \langle g|\hat{\boldsymbol{\mu}}|e\rangle$ is the dipole matrix element. Under the rotating wave approximation, the interaction Hamiltonian

becomes

$$\hat{H}_{int} = i(\boldsymbol{\mu} \cdot \boldsymbol{\epsilon}^*) \sqrt{\frac{\hbar\omega_c}{2\epsilon_0 V}} u(\mathbf{r}) \hat{\sigma} \hat{a}^\dagger - i(\boldsymbol{\mu}^* \cdot \boldsymbol{\epsilon}) \sqrt{\frac{\hbar\omega_c}{2\epsilon_0 V}} u(\mathbf{r}) \hat{\sigma}^\dagger \hat{a} \quad (3.29)$$

$$= i\hbar u(\mathbf{r})(g_0 \hat{\sigma} \hat{a}^\dagger - g_0^* \hat{\sigma}^\dagger \hat{a}) \quad (3.30)$$

The coupling constant $g_0 = (\boldsymbol{\mu} \cdot \boldsymbol{\epsilon}^*) \sqrt{\frac{\omega_c}{2\hbar\epsilon_0 V}}$ describes how well coupled a two level system is to the optical mode. It is the rate at which energy is transferred between the dipole and the electromagnetic field. The coupling constant g_0 is typically taken to be real. This amounts to taking $\boldsymbol{\mu} \cdot \boldsymbol{\epsilon}^* = \boldsymbol{\mu}^* \cdot \boldsymbol{\epsilon}$.

The total coherent coupling rate, $g = g_0 u(\mathbf{r})$, is a position dependent coupling rate. This implies that the strength of the coupling of an atom to a cavity depends on the position of the atom in the mode. For a tightly confined ion well within the Lamb–Dicke limit, we take the position to be the mean position of the ion, \mathbf{r}_{ion} . Then the coherent coupling rate is $g = g_0 u(\mathbf{r}_{ion})$.

For a thermal state of ion motion, the probability distribution of the ion position is normally distributed with variance $x_0^2(2\bar{n} + 1)$. Here $x_0 = \sqrt{\hbar/2m\omega_t^2}$ is the ground state spread of the motional wavepacket, and \bar{n} is the mean thermal occupation number of a harmonic trap. In general, the coupling rate must be averaged over the probability density of the ion’s position, resulting in an overall effective coupling rate. A simple method to see how the coupling rate decreases is to take the ion to have a classical harmonic trajectory along the cavity axis, $z(t) = z_0 + z_1 \cos(\omega_s t + \varphi)$. Then the coherent coupling rate is

$$g = g_0 \cos \left[kz_0 + kz_1 \cos(\omega_s t + \varphi) + (m - 1) \frac{\pi}{2} \right]$$

Utilizing the Jacobi–Anger formula to expand the time variation, and averaging over the phase φ , the coherent coupling rate is reduced to

$$g = g_0 J_0(kz_1) \cos(kz_0 + (m - 1)\pi/2)$$

Thus, it is important to minimize the size of the ion's thermal excursions as well as to place the mean value at an anti-node.

3.4.2 Pump Hamiltonian In order to provide energy into the system, the atom-cavity system must be driven by some pumping mechanism. Often, in neutral atom cavity QED experiments, the cavity mode is driven by a classical beam and modifications of the transmission provide information regarding the dynamics of the atom-cavity system. To generate and collect photons entangled with the atom, we instead drive the atom with a semiclassical beam. The interaction of a two level system with a classical beam is given by $\hat{H}_p = -\hat{\boldsymbol{\mu}} \cdot \mathbf{E}_p$, where the electric field is a classical quantity and is given by equation

$$\mathbf{E}_p = \frac{1}{2}\boldsymbol{\epsilon}\mathcal{E}_p e^{-i\omega_L t} + \frac{1}{2}\boldsymbol{\epsilon}^*\mathcal{E}_p^* e^{i\omega_L t} \quad (3.31)$$

Under the rotating wave approximation, and using a two-level approximation, the pumping Hamiltonian is given by

$$\hat{H}_p = \frac{1}{2}\boldsymbol{\mu} \cdot \boldsymbol{\epsilon}^*\mathcal{E}_p^* \hat{\sigma} e^{i\omega_L t} + \frac{1}{2}\boldsymbol{\mu}^* \cdot \boldsymbol{\epsilon}\mathcal{E}_p \hat{\sigma}^\dagger e^{i\omega_L t} \quad (3.32)$$

$$= \hbar\eta \hat{\sigma} e^{i\omega_L t} + \hbar\eta^* \hat{\sigma}^\dagger e^{-i\omega_L t}, \quad (3.33)$$

where $\eta = (\boldsymbol{\mu} \cdot \boldsymbol{\epsilon}^*)\mathcal{E}_p^*/2\hbar$ is half the Rabi frequency. For simplicity, we shall take it to be purely a real quantity. The pump rate η can be related to the saturation irradiance [107],

$$I_{sat} = \frac{\gamma_\perp \hbar\omega}{\sigma_{abs}},$$

where $\sigma_{abs} = 6\pi(\lambda/2\pi)^2$ is the resonant absorption cross-section, and γ_\perp is the dipole decay rate. Then,

$$\eta = \frac{1}{2}\sqrt{\gamma_\perp \gamma_\parallel} s = \frac{\gamma}{2}\sqrt{\frac{s}{2}} \quad (3.34)$$

where the last equation holds for a radiatively broadened transition, and $s = I_p/I_{sat}$ is the saturation parameter. Note: $\gamma_\parallel = \gamma$ is the spontaneous emission rate.

3.4.3 Master Equation for the atom–cavity system In addition to the unitary evolution of the system due to the Hamiltonian dynamics, dissipative effects must be taken into account. Both the atom and cavity mode are coupled to a bath of electromagnetic modes. Tracing out these mode leads to spontaneous emission out the side of the cavity, as well as transmitted light out the cavity. Under the Born and Markov approximations, the density matrix for the system evolves under the master equation [108]

$$\dot{\rho} = \frac{1}{i\hbar}[\hat{H}, \rho] + \sum_k \left\{ \hat{C}_k \rho \hat{C}_k^\dagger - \frac{1}{2} \left(\hat{C}_k^\dagger \hat{C}_k \rho + \rho \hat{C}_k^\dagger \hat{C}_k \right) \right\}. \quad (3.35)$$

The operators \hat{C}_k are the collapse (or quantum jump) operators. These operators are responsible for the jumps between quantum states. The collapse operators relevant for the atom–cavity system are $\hat{C}_c = \sqrt{2\kappa}\hat{a}$, $\hat{C}_0 = \sqrt{\gamma_{\parallel}}\hat{\sigma}$, and $\hat{C}_\varphi = \sqrt{\gamma_\varphi/2}\hat{\sigma}_z$. The first describes cavity photon loss at a rate 2κ . This combines the effect of both transmission and absorption/scattering of photons. The next, \hat{C}_0 describes spontaneous emission at a rate γ_{\parallel} . The third is a dephasing operator, where the dipole dephases at a rate γ_φ . The overall dipole decay rate is then $\gamma_{\perp} = \gamma_{\parallel}/2 + \gamma_\varphi$. Dephasing mechanisms could include various broadening mechanisms such as collisional broadening. For trapped ions in ultrahigh vacuum, the atom is only radiatively broadened, so $\gamma_{\perp} = \gamma_{\parallel}/2$.

3.4.4 Cavity QED Parameters There are two parameters in cavity QED that are important for the dynamics of the system. The first is the saturation photon number, n_{sat} . The Rabi frequency for n photons is $2g\sqrt{n} = \sqrt{\gamma_{\perp}\gamma_{\parallel}s}$. At saturation, $s = 1$ and $n = n_{sat}$. This leads to a saturation photon number

$$n_{sat} = \frac{\gamma_{\perp}\gamma_{\parallel}}{4g^2} = \frac{V I_{sat}}{c \hbar\omega_0}. \quad (3.36)$$

Equivalently, $I_{sat} = \hbar\omega_0 n_{sat}(c/V)$. The saturation photon number determines the size of the system and scales the energy inside the cavity [109]. For atoms averaged over the Gaussian mode, n_{sat} has an additional geometric factor of 2/3 [110, 111].

The other parameter is the cooperativity, $C = g^2/2\kappa\gamma_\perp$. This parameter describes the strength of the coupled atom–cavity system relative to the dissipative rates. In terms of the Q of the resonator, it is half the Purcell factor (Equation 3.22). In other forms, it is the ratio of the absorption cross section of the atom to the area of the mode:

$$C = \frac{g^2}{2\kappa\gamma_\perp} = \frac{1}{2} \frac{3Q\lambda^3}{4\pi^2V} = \frac{\mathfrak{F}}{2\pi} \frac{2\sigma_{abs}}{\pi w_0^2/2}. \quad (3.37)$$

Occasionally the critical atom number $N_c = 1/C$ is given instead of the cooperativity, as it quantifies the number of atoms that must be present in the cavity to have a large effect on the transmission of the cavity [111].

There are three experimental regimes in cavity QED. The regimes are

1. Strong Coupling: $g \gg \kappa, \gamma$. Here, $C \gg 1$ and $n_{sat} < 1$. In this regime, the vacuum Rabi splitting is observable [112, 113] and the atom and photon exchange energy. The output wavepacket has modulations at the Rabi frequency.
2. Bad-cavity limit: $\kappa \gg g \gg \gamma$. In this regime, the decay rate out the cavity is much larger than any coherent dynamics. Thus the cavity mode is essentially never populated as any excitation of the cavity mode is immediately lost. In this manner, the cavity acts as a reservoir and can be traced out. Due to the strength of the atom–cavity coupling, the atom exhibits enhanced spontaneous emission. Note: in this limit, it can be difficult to get a large cooperativity [104].
3. Intermediate Regime: Neither strong coupling nor bad-cavity. The coherent and dissipative rates are close to the same strength. In this case, neither the coherent dynamics nor the dissipation is dominant.

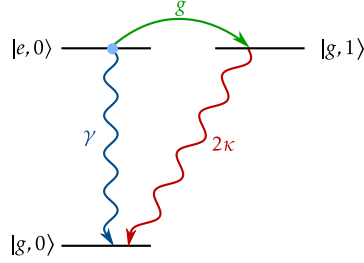


Figure 3.5: Relevant energy levels of a two-level system coupled to a harmonic oscillator. The atom is initially in the excited state $|e, 0\rangle$ and either decays to the ground state $|g, 0\rangle$ by emitting a photon out the side of the cavity at a rate γ , or transfers the excitation to the cavity mode which decays at a rate 2κ .

3.5 Photon emission from an optical cavity

With the tools to describe the atom–cavity system, it is possible to present methods to collect light from the optical cavity. First is a discussion of photon emission from a cavity given an initially excited atom. This model is then extended to a driven two level atom in a cavity. Finally is a presentation of generating polarization qubits from $^{171}\text{Yb}^+$ coupled to a cavity.

3.5.1 Initially excited two-level atom Take a two-level atom coupled to a cavity that is resonant with the transition, and is initially in the excited state with no photons in the cavity ($|\psi(0)\rangle = |e, 0\rangle$). The state of the atom–cavity system can be written in terms of three levels, $|\psi(t)\rangle = c_e(t)|e, 0\rangle + c_g(t)|g, 1\rangle + c_0(t)|g, 0\rangle$. Figure 3.5 illustrates the energy levels of the system under consideration.

In a rotating frame, the Hamiltonian reduces to

$$\hat{H} = i\hbar g(\hat{\sigma}\hat{a}^\dagger - \hat{\sigma}^\dagger\hat{a}), \quad (3.38)$$

where the atom and cavity are co-resonant. The resulting master equation shows that the state $|g, 0\rangle$ only couples to the other states through dissipative means, and plays no role in the dynamics of the other two levels. In fact, the differential equations for the populations and coherences of interest ($\rho_{e0,e0}$, $\rho_{g1,g1}$, $\rho_{g1,e0}$, and

$\rho_{e0,g1}$) can be derived from the Schrödinger equation with phenomenologically added decay mechanisms:

$$\dot{c}_e = -gc_g - \frac{1}{2}\gamma c_e \quad (3.39)$$

$$\dot{c}_g = gc_e - \kappa c_g. \quad (3.40)$$

This is possible because the final state in the decay channels does not play a role in the dynamics of the system. It only acts as a reservoir for the population [104].

This system is easily solved with Laplace transforms. Taking these equations to the s -domain and solving with initial conditions $c_e(0) = 1$ and $c_g(0) = 0$ yields

$$C_g(s) = \frac{g}{(s + \kappa)(s + \gamma/2) + g^2} \quad (3.41)$$

$$C_e(s) = \frac{s + \kappa}{(s + \kappa)(s + \gamma/2) + g^2}. \quad (3.42)$$

The poles of the system are $r_{\pm} = -\frac{1}{2}(\kappa + \gamma/2) \pm i\frac{1}{2}\Omega_s$, where $\Omega_s = \sqrt{4g^2 - (\kappa - \gamma/2)^2}$ is the normal mode splitting. This is the energy splitting of the two decoupled dressed states. Note that when $\gamma = \kappa = 0$, the splitting is $2g$, agreeing with the dressed state splitting in the Jaynes–Cummings model. However, Ω_s can be imaginary if the decay rate is larger than the coupling. Drawing an analogy between the equations of motion of the amplitudes to a harmonic oscillator, the case of $\Omega_s \in \mathbb{R}$ corresponds to an underdamped oscillator, while Ω_s purely imaginary corresponds to an overdamped oscillator. Critical coupling is when $2g = |\kappa - \gamma/2|$.

Expanding $C_e(s)$ and $C_g(s)$ in partial fractions and inverse transforming back to the time domain gives the amplitudes of $|g, 1\rangle$ and $|e, 0\rangle$ for times $t > 0$.

$$c_g(t) = \frac{-ig}{\sqrt{4g^2 - (\kappa - \gamma/2)^2}} (e^{r_+t} - e^{r_-t}) \quad (3.43)$$

$$c_e(t) = \frac{(\kappa - \gamma/2) + i\Omega_s}{i2\Omega_s} e^{r_+t} - \frac{(\kappa - \gamma/2) - i\Omega_s}{i2\Omega_s} e^{r_-t}. \quad (3.44)$$

The populations of the states are

$$\rho_{g1,g1}(t) = |c_g(t)|^2 = \frac{2g^2}{4g^2 - (\kappa - \gamma/2)^2} e^{-(\kappa+\gamma/2)t} [1 - \cos(\Omega_s t)] \quad (3.45)$$

$$\begin{aligned} \rho_{e0,e0}(t) = |c_e(t)|^2 &= \frac{2g^2}{4g^2 - (\kappa - \gamma/2)^2} e^{-(\kappa+\gamma/2)t} \\ &\times \left[1 + \frac{2g^2 - (\kappa - \gamma/2)^2}{2g^2} \cos(\Omega_s t) + \frac{(\kappa - \gamma/2)\Omega_s}{2g^2} \sin(\Omega_s t) \right] \end{aligned} \quad (3.46)$$

If the system were overdamped, then Ω_s is purely imaginary, and $\cos \rightarrow \cosh$ and $\sin \rightarrow i \sinh$. The populations are still real as the sine term has a factor of Ω_s . These hyperbolic cosine and sine behavior leads to an enhanced decay rate

$$\Gamma_{\text{eff}} = \frac{1}{2}\gamma + \kappa - \sqrt{(\kappa - \gamma/2)^2 - 4g^2} \approx \gamma + \frac{2g^2}{(\kappa - \gamma/2)} \approx \gamma(1 + 2C) \quad (3.47)$$

The probability to emit a photon from the cavity in the time interval $[t, t + dt]$ is $p_E(t)dt = 2\kappa \langle \hat{a}^\dagger \hat{a} \rangle dt$. In this system, this reduces to

$$p_E(t)dt = 2\kappa \langle \hat{a}^\dagger \hat{a} \rangle dt = 2\kappa \rho_{g1,g1}(t)dt \quad (3.48)$$

This emission probability is plotted in Figure 3.6a for both strong coupling where there are vacuum Rabi oscillations, and the experimentally realized cavity. Since $p_E(t)$ describes the probability density of a photon out the cavity mode it is proportional to the emitted photon wavepacket and describes the photon arrival time distribution [114].

Integrating from $t = 0$ to a time t gives the cumulative probability for emitting a photon in the interval $[0, t)$

$$\begin{aligned} P_E(t) &= 2\kappa \int_0^t d\tau \rho_{g1,g1}(\tau) \\ &= \frac{g^2 \kappa}{(\kappa + \gamma/2)(g^2 + \kappa\gamma/2)} \\ &\quad - \frac{4g^2 \kappa}{4g^2 - (\kappa - \gamma/2)^2} e^{-(\kappa+\gamma/2)t} \left[\frac{1}{\kappa + \gamma/2} - \frac{(\kappa + \gamma/2) \cos(\Omega_s t) + \Omega_s \sin(\Omega_s t)}{4g^2 + 2\kappa\gamma} \right]. \end{aligned} \quad (3.49)$$

This expression is plotted in Figure 3.6b for strong coupling and the experimentally realized cavity described in Chapter V. While there are small oscillations in the total emission probability, it quickly asymptotes to the final value given by $P_E(t \rightarrow \infty)$. The total collection efficiency is the final emission probability ($P_E(t \rightarrow \infty)$) multiplied by the fraction of the total losses that is transmission through the outcoupling mirror.

$$p_c = \frac{T_2}{\mathcal{L}} \frac{g^2 \kappa}{(\kappa + \gamma/2)(g^2 + \kappa\gamma/2)} = \frac{T_2}{\mathcal{L}} \left(\frac{2\kappa}{2\kappa + \gamma} \right) \left(\frac{2C}{1 + 2C} \right) \quad (3.50)$$

Here, we see the factor $2C/(1 + 2C)$ that is typically quoted. However, it is modified by a factor $2\kappa/(2\kappa + \gamma)$, which is the ratio of the dissipation rate out of the cavity versus the total dissipation rate. While this method gives the emission rate, a more sophisticated approach using the master equation can give the spectrum of fluorescence out of the cavity [104].

This expression indicates the probability that a photon is emitted out the cavity given an initially excited ion. In order to achieve this experimentally, the ion would have to be excited by a pulsed laser, such as is done in the remote entanglement experiments. Equation 3.50 is an exact expression for an initially excited two-level atom regardless of the regime. It is not valid for a ground state atom that is being driven continuously.

In order to extract photons efficiently, one would design the experimental apparatus to be in the bad-cavity limit, where $\kappa \gg g^2/\gamma \gg \gamma$. A large coherent coupling rate is needed to coherently exchange the excitation into the cavity. A short photon lifetime $1/2\kappa$ is needed such that the photon in the cavity is emitted faster than it can be re-absorbed by the atom.

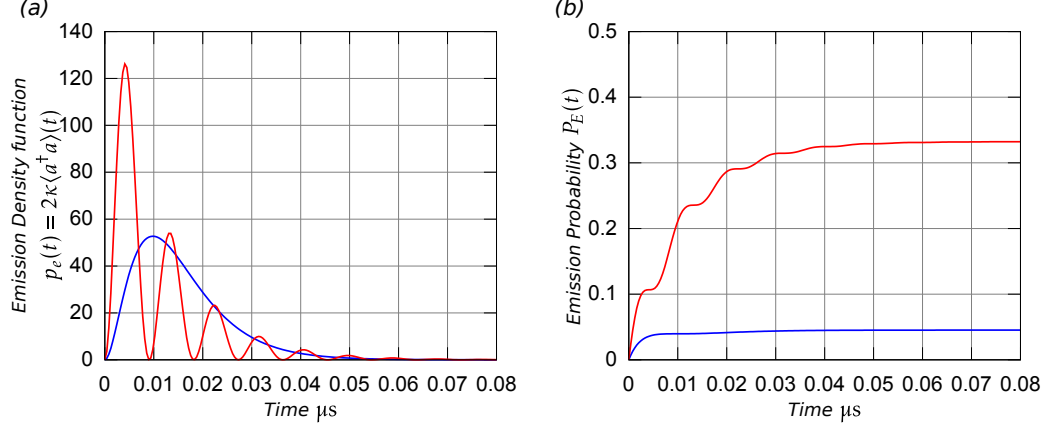


Figure 3.6: **(a)** Probability density function $2\kappa\langle a^\dagger a \rangle(t)$ for photon to be emitted by the cavity in the interval $[t, t + dt)$ given an initially excited atom. *Red curve*: Strong coupling regime where $(g, \kappa, \gamma)/2\pi = (55, 5, 19.7)$ MHz. Oscillations indicate modulation of the photon wavepacket. *Blue curve*: Emission density function for the experimentally realized cavity, with $(g, \kappa, \gamma)/2\pi = (4, 24, 19.7)$ MHz. **(b)** Cumulative emission probability (equation 3.49) for both strong coupling (*red*) and the experimentally realized system (*blue*).

3.5.2 Driven Two-level system Now consider a driven two level system coupled to a cavity. In a rotating frame, the Hamiltonian is given by

$$\hat{H} = \hbar\delta_c \hat{a}^\dagger \hat{a} + \hbar\delta_0 \hat{\sigma}^\dagger \hat{\sigma} + i\hbar g(\hat{\sigma} \hat{a}^\dagger - \hat{\sigma}^\dagger \hat{a}) + \hbar\eta(\hat{\sigma} + \hat{\sigma}^\dagger). \quad (3.51)$$

Here, $\delta_c = \omega_c - \omega_L$ is the detuning of the cavity from the laser driving the atom, and $\delta_0 = \omega_0 - \omega_L$ is the detuning of the atom from the laser. From the master equation (equation 3.35), the differential equations for the expectation values of the cavity field, dipole moment, and inversion are

$$\langle \dot{\hat{a}} \rangle = -(\kappa + i\delta_c) \langle \hat{a} \rangle - g \langle \hat{\sigma} \rangle \quad (3.52)$$

$$\langle \dot{\hat{\sigma}} \rangle = -(\gamma_\perp + i\delta_0) \langle \hat{\sigma} \rangle - g \langle \hat{a} \hat{\sigma}_z \rangle + i\eta \langle \hat{\sigma}_z \rangle \quad (3.53)$$

$$\langle \dot{\hat{\sigma}}_z \rangle = -\gamma_\parallel (1 + \langle \hat{\sigma}_z \rangle) + 2g(\langle \hat{a} \hat{\sigma}^\dagger \rangle + \langle \hat{a}^\dagger \hat{\sigma} \rangle) + i2\eta(\langle \hat{\sigma} \rangle + \langle \hat{\sigma}^\dagger \rangle) \quad (3.54)$$

It is difficult to solve this system, as these differential equations couple to higher order correlations of the atom and the cavity field. A simple approximation is the semiclassical approximation, where the quantum correlation between the atom and field

is neglected, allowing factorization of the expectation values: $\langle \hat{a}\hat{\sigma}^\dagger \rangle = \langle \hat{a} \rangle \langle \hat{\sigma}^\dagger \rangle$ [115]. Under this approximation, the three coupled differential equations (equations 3.52–3.54) completely describe the system.

For notational ease, transform to a set of unit-less coordinates. First, define detunings $\theta = \delta_c/\kappa$ and $\Delta = \delta_0/\gamma_\perp$. Normalizing the cavity field to the saturation photon number n_{sat} and the pump to the saturation intensity [115], define

$$x = \frac{\langle \hat{a} \rangle}{\sqrt{n_{sat}}} \quad m = 2\sqrt{\frac{\gamma_\perp}{\gamma_\parallel}} \langle \hat{\sigma} \rangle \quad w = \langle \hat{\sigma}_z \rangle \quad y = \frac{2\eta}{\sqrt{\gamma_\perp\gamma_\parallel}} = \sqrt{s} \quad (3.55)$$

Then, the differential equations become (using $C = g^2/2\kappa\gamma_\perp$)

$$\kappa^{-1}\dot{x} = -(1 + i\theta)x - 2Cm \quad (3.56)$$

$$\gamma_\perp^{-1}\dot{m} = -(1 + i\Delta)m - xw + iyw \quad (3.57)$$

$$\gamma_\parallel^{-1}\dot{w} = -(1 + w) + \frac{1}{2}(xm^* + x^*m) + i\frac{1}{2}y(m - m^*) \quad (3.58)$$

These equations are in a similar form to those that describe optical bistability [115]. In these equations, the pump y drives the both the dipole and the inversion. In the bistability equations the pump is on the cavity mode.

Of interest is the steady state photon emission rate out of the cavity, $2\kappa\langle \hat{a}^\dagger\hat{a} \rangle = 2\kappa n_{sat}|x_{ss}|^2$ and out the side $\gamma_\parallel\langle \hat{\sigma}^\dagger\hat{\sigma} \rangle = \gamma(1 + w)/2$. Setting the time derivatives to zero and solving for the cavity field leads to

$$m = \frac{-1}{2C}(1 + i\theta)x \quad (3.59)$$

$$w = \frac{(1 + i\Delta)(1 + i\theta)}{2C} \frac{x}{x - iy} \quad (3.60)$$

$$0 = 1 + \frac{(1 + i\Delta)(1 + i\theta)}{2C} \frac{x}{x - iy} + \frac{|x|^2}{2C} + \frac{iy}{4C} [(x - x^*) + i\theta(x + x^*)] \quad (3.61)$$

When both the cavity and atom are resonant with the driving laser light, the imaginary part of the third equation shows that x must be purely imaginary. Using

this, one arrives at a cubic equation for the imaginary part of $x = ib$

$$b^3 - 2yb^2 + (y^2 + 1 + 2C)b - 2Cy = 0 \quad (3.62)$$

Since $x = ib$, b must be real. Solving this equation for the real roots gives the steady state electric field strength in the cavity, and thus the steady-state emission rate of photons from the cavity $2\kappa n_{sat}|x|^2$. Figure 3.7a plots the co-resonant emission rate versus saturation irradiance for both the solution to equation 3.62 and a full numerical solution to the master equation. The cavity QED parameters are for the cavity described in chapter V. It becomes apparent that for pump irradiances larger than 0.5, the semiclassical approximation breaks down.

The emission rate versus detuning is plotted in figure 3.7b where the pump is taken to be at saturation. While there is some deviation between the numerical solution of the master equation and the semiclassical approximation, they result in qualitatively similar behavior.

The collection efficiency is given by the ratio of emission out the cavity to all emissions (side plus cavity)

$$p_c = \frac{T_2}{\mathcal{L}} \frac{2\kappa n_{sat}|x_{ss}|^2}{2\kappa n_{sat}|x_{ss}|^2 + \gamma(1+w)/2} = \frac{T_2}{\mathcal{L}} \frac{x}{y} = \frac{T_2}{\mathcal{L}} \frac{|\langle \hat{\mathbf{E}}^{(+)} \rangle|}{\mathcal{E}_p} \quad (3.63)$$

where x_{ss} is the steady state cavity field given by equation 3.61 and w is the steady-state inversion given by equation 3.60. The last equality holds when the pump and cavity co-resonant with the atom (so x_{ss} is the solution to equation 3.62). Then the collection efficiency is the ratio of the cavity field to the pump field. Again this can be compared to the numerical solution of the master equation (figure 3.7c).

In the low saturation limit ($s < 0.1$), it is possible to further approximate the steady state inversion to be $w = -1$. In this case, equations 3.56 and 3.57 describe the system and can be easily solved. The steady state emission rate out the cavity

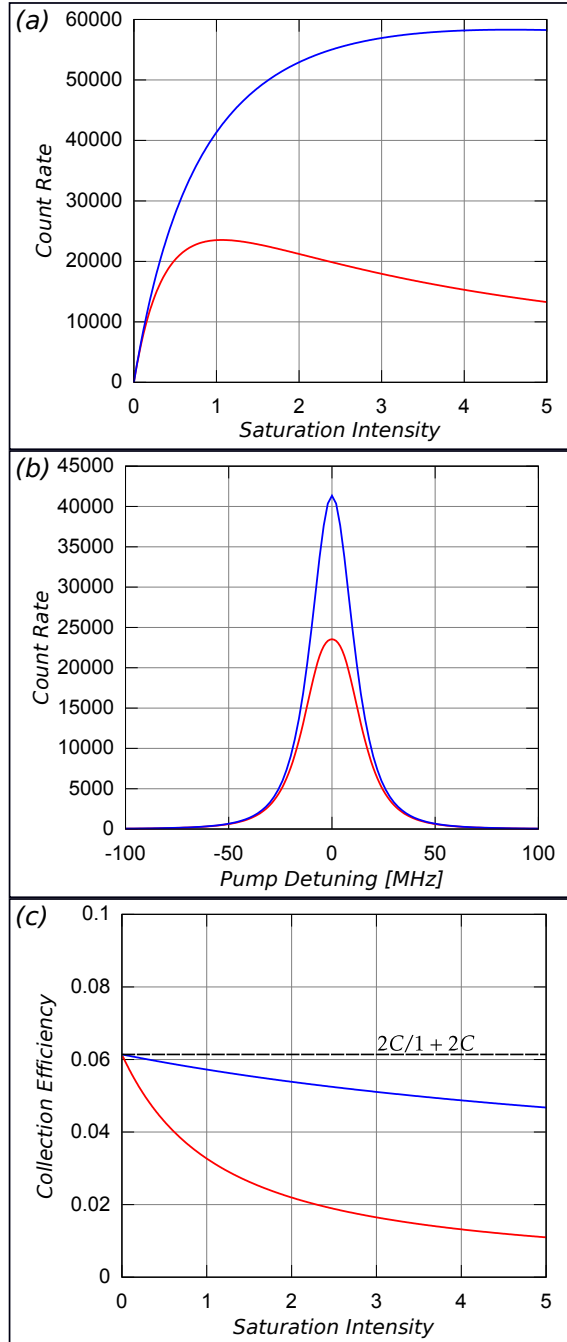


Figure 3.7: **(a)** Expected count rates on a PMT for a driven TLS versus pump irradiance. These rates include the detector efficiency of 10% and the cavity and pump are co-resonant with the atomic transition. The cavity QED parameters used are for the cavity realized in the experiment, $(g, \kappa, \gamma)/2\pi = (3.9, 24, 19.6)\text{MHz}$. **(b)** Expected count rates versus pump detuning. The cavity is resonant with the atomic transition ($\delta_c = \delta_0$). **(c)** The collection efficiency for resonant drive and cavity as a function of the saturation parameter. Note that as $s \rightarrow 0$, the efficiency approaches $2C/(1+2C)$. *Red curve:* The solution of the semiclassical model (equation 3.61). *Blue curve:* Numerical solution of the steady-state Master equation.

for the resonant case is

$$p_E = \frac{\gamma C s}{(1 + 2C)^2} = \Gamma_{sc} 2C$$

where $\Gamma_{sc} = (\gamma/2)(s/(1 + 2C)^2)$ is the maximum scatter rate times the effective saturation parameter. The photon collection efficiency reduces to the Purcell result

$$p_c = \frac{T_2}{\mathcal{L}} \frac{2C}{1 + 2C}$$

3.5.3 Generation of entangled photons Now consider an $^{171}\text{Yb}^+$ ion coupled to the cavity. The cavity mode is most amenable to polarization qubits, which is the main focus of this subsection. A few comments will be made at the end regarding the generation of other types of photonic qubits.

Similar to other methods of generating single photons [116, 74, 76, 73], the protocol to generate photons relies upon driving the atom from one hyperfine ground state to the other. While these rely upon a detuning of the cavity and pump from resonance to the P manifold for cavity-assisted Raman transitions, the protocol here is to use a resonant pump and cavity.

The setup for this protocol is shown in figure 3.8, where the cavity is locked to the $F = 1 \leftrightarrow F' = 1$ transition of the qubit and the quantization axis of the atom along the cavity. The ion, initialized to the $^2\text{S}_{1/2} |0, 0\rangle$ level is driven by a π -polarized CW laser to the $^2\text{P}_{1/2} |1, 0\rangle$ level (figure 3.8b). The $^2\text{P}_{1/2} |1, 0\rangle$ level is coupled through the two polarization modes of the cavity to the $^2\text{S}_{1/2} |1, \pm 1\rangle$ levels of the atom. The orientation of the quantization axis and the cavity linewidth ensure that only σ^\pm transitions are coupled. The atom-cavity system undergoes coherent evolution from $^2\text{P}_{1/2} |1, 0\rangle$ to $^2\text{S}_{1/2} |1, \pm 1\rangle$, resulting in the entangled state

$$|\psi\rangle = \frac{1}{\sqrt{2}} (|+1, \sigma_-\rangle - |-1, \sigma_+\rangle) \quad (3.64)$$

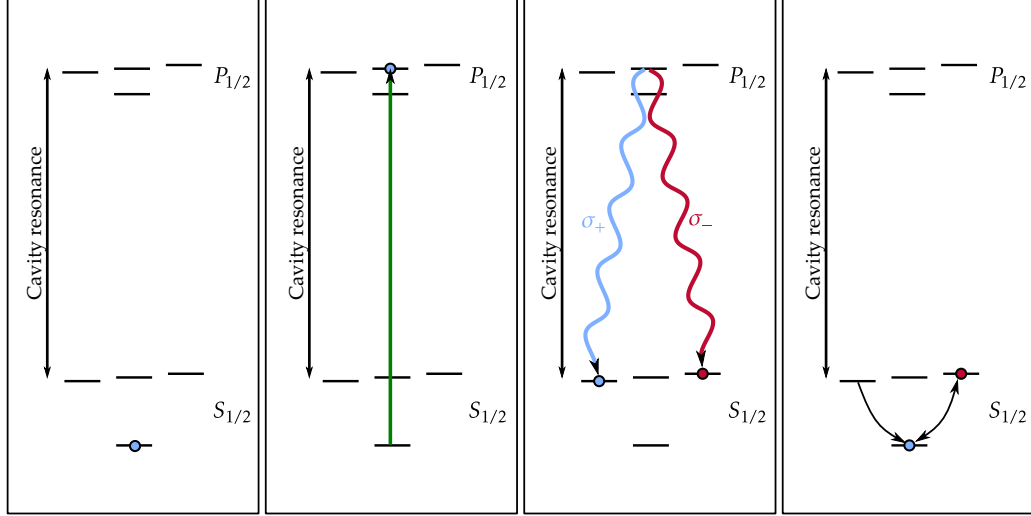


Figure 3.8: Protocol to generate polarization-entangled photons in a cavity. **(a)** Lock cavity to the $F = 1 \leftrightarrow F' = 1$ transition, and initialize the ion to ${}^2S_{1/2} |0, 0\rangle$. **(b)** Resonantly excite the ion with π -polarized cw light on the ${}^2S_{1/2} |0, 0\rangle \leftrightarrow {}^2P_{1/2} |1, 0\rangle$ transition. **(c)** When the ion emits a photon into the cavity it is either a σ_+ or σ_- photon, and is entangled with the m_F state of the ion. **(d)** The state of the ion is measured conditioned on the state of the detected photon. Microwaves transfer the ion qubit state to measurement basis. Additional microwaves are needed to measure the ion in a rotated basis.

where σ_{\pm} denotes the polarization of the photonic state, and ± 1 is the magnetic quantum number of the $F = 1$ manifold. Conditioned on a photon detection, the atomic state is projected onto either ${}^2S_{1/2} |1, 1\rangle$ or ${}^2S_{1/2} |1, -1\rangle$. Application of microwaves can map the state of the ion onto the measurement basis (figure 3.8d).

The dynamics of this protocol is rather complicated to solve in general as at least 6 atomic levels are involved (${}^2S_{1/2} |0, 0\rangle$, ${}^2S_{1/2} |1, \pm 1\rangle$, and the $F' = 1$ manifold of ${}^2P_{1/2}$), as well as two photonic modes. Numerical simulations of the system can be performed for the experimental regime of the system (figure 3.9). The output photon wavepacket is given by the emission profile, and is illustrated in figure 3.9, while the integrated emission probability asymptotes to $p_c = 0.04$ (figure 3.9b). This illustrates that the experimental setup could in principle create entangled ion–photon pairs with a higher success probability than free space implementations.

The excited state can spontaneously emit photons that are not in the cavity. The

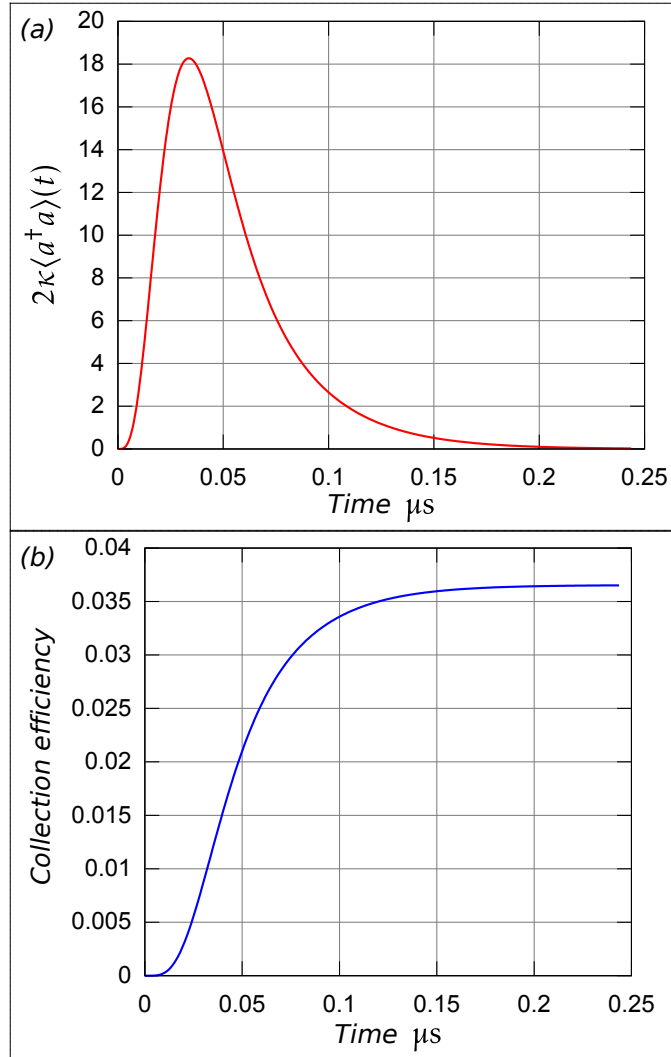


Figure 3.9: **(a)** Output photon wavepacket for the entanglement protocol. **(b)** Cumulative probability density to collect a photon emitted from the cavity. After several linewidths, the density asymptotes to a collection efficiency of 4%.

available states are $|1, \pm 1\rangle$ and $|0, 0\rangle$. The atom cannot emit light into the cavity and return to the $|0, 0\rangle$ state, as that transition is 12.642 GHz off-resonant from the cavity, which is well outside the linewidth of the cavity. Scattering to the other two states only reduces the overall success rate of the protocol, as those states are not driven by the pump.

Therefore, the presence of a single photon out of the cavity will be entangled with the atomic state. Infidelity of this state arises from three sources. The first is imperfect polarization of the pump light. This protocol requires the atom be driven from the ${}^2S_{1/2} |0, 0\rangle$ state to the ${}^2P_{1/2} |1, 0\rangle$ state with high fidelity. Without good polarization extinction, the ion can be driven to the ${}^2P_{1/2} |1, \pm 1\rangle$ levels, which can emit σ_{\pm} photons into the cavity. These photons are indistinguishable from the photons we desire to generate. Additionally, the resultant atom-photon state is not an entangled state, as the resultant atomic state is ${}^2S_{1/2} |1, 0\rangle$. Even though the excited states ${}^2P_{1/2} |1, \pm 1\rangle$ can emit π -polarized light leaving the atom in the final atomic states ${}^2S_{1/2} |1, \pm 1\rangle$, due to the orientation of the magnetic field for the quantization axis the radiation pattern of the ion is at a minimum along the cavity axis. The probability of this error is given by the extinction ratio of the polarization, which in principle can be on the order of 1×10^{-3} – 1×10^{-6} .

The second source of infidelity is the generation of cavity photons from the pump. However, as the cavity is locked to the other hyperfine level, the scatter into the cavity mode should be suppressed due to the frequency being in the wings of the lineshape. The scattering should be suppressed by $\sim (\Delta\nu_{fwhm}/\nu_{HF})^2 \sim 1 \times 10^{-6}$. Even with this suppression, care must be taken in order to ensure a low background.

The third source of infidelity occurs after the successful generation of an ion-photon entangled pair. Since the pump is driven by a continuous-wave source, it

is possible to off-resonantly drive the $S|1, 1\rangle \leftrightarrow P|1, 1\rangle$ and $S|1, -1\rangle \leftrightarrow P|1, -1\rangle$ transitions. Upon scattering, the frequency of the photon generated is the same as that of the laser, and hence will not be coupled into the cavity. However, the spontaneous emission will decohere the entangled state, lowering the fidelity of the entanglement. The probability of this error occurring is estimated as $\gamma_{sc}\tau$, where γ_{sc} is the photon scatter rate, and τ is the duration of the pump beam. As the pump is several gigahertz off-resonant, the occurrence of this error should be on the order of 10^{-4} .

Finally, this protocol can be extended to both frequency qubits and time-bin qubits. However, both of these extensions suffer from an increased error rate. Figure 3.10 illustrates the essential aspects of the two protocols. For frequency qubits, begin with the free-spectral range of the cavity equal to the hyperfine splitting of the ion. In this manner, both frequencies are supported by the cavity mode. For $^{171}\text{Yb}^+$, the separation must be at least $L = c/2\nu_{fsr} = 1.186$ cm. In order to maintain a large coherent coupling rate, g , the cavity would have to be in a near-concentric geometry.

For frequency qubits the atom would be prepared in the $S|1, -1\rangle$ state, and is driven by π -polarized light to the $P|1, -1\rangle$ state (figure 3.10a), where both σ^+ transitions are coupled to the cavity. Likewise, for time-bin qubits, the cavity would be locked on the $F = 1$ to $F' = 0$ transition. Excitation of the atom to generate the photon would be the same frequency and polarization as the cavity, and therefore more susceptible to scattered pump light (figure 3.10b).

Overall, entanglement protocols with optical cavities offer an enhancement in the collection of entangled light that can be used for quantum networks. Although the theoretical collection efficiency for the experimental cavity is near 4%, this is not an upper bound. In principle, photon generation with a cavity could be determinis-

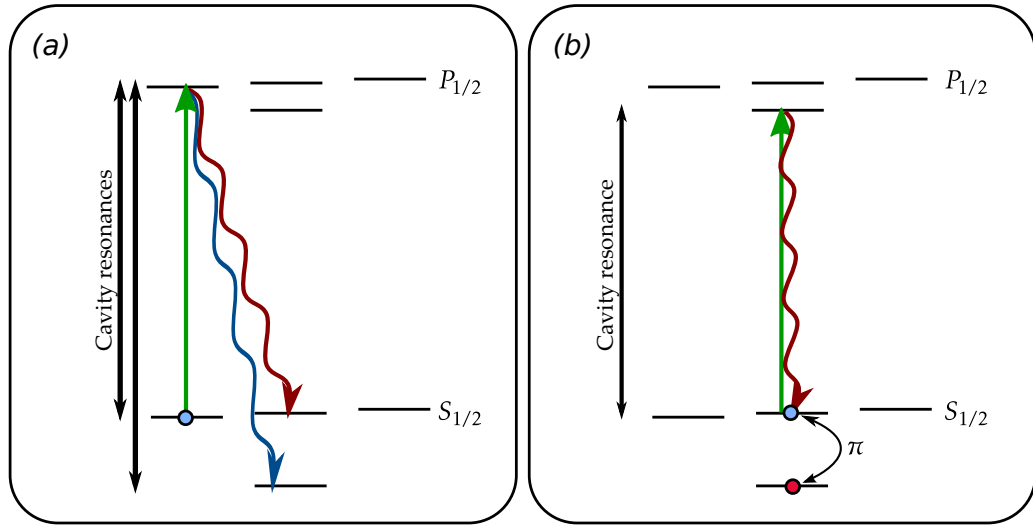


Figure 3.10: Illustration of generating frequency and time-bin qubits from an optical cavity. Both protocols suffer from errors that are naturally suppressed in the polarization qubit case. **(a) Frequency Qubits** The free-spectral range of the cavity is set to the hyperfine splitting of the ion. The ion is initially prepared in $S |1, -1\rangle$ and is driven by π -polarized light to the $P |1, -1\rangle$ level. The σ_- decays channels both couple to two different cavity modes, resulting in frequency qubits. However, the drive can scatter off a trap electrode into the cavity mode. **(b) Time-bin Qubits** The cavity is locked to the $S |1, 1\rangle \leftrightarrow P |1, 0\rangle$ transition, and the ion is initially prepared in a superposition of qubit states. The pump drives the $S |1, 1\rangle \leftrightarrow P |1, 0\rangle$ transition. In this case, the pump is the same frequency and polarization as the quantum mode of the cavity. Additionally, fast π rotations can create indistinguishable photons in the cavity.

tic [69]. Before this protocol can be implemented, we first need an ion trap capable of realizing this scheme. The next chapter describes such a trap.

CHAPTER IV

Ion trapping

Earnshaw's theorem states that a system of charged particles cannot be held in a stable equilibrium position with only electrostatic forces [117, 118]. This theorem is a corollary of Gauss' law for a charge-free region, $\nabla \cdot \mathbf{E} = 0$. The electric field lines entering a charge-free volume must leave the region, providing a field line along which charged particles can escape. However, confinement of charged particles can be achieved with dynamic fields. This is the basis for the radiofrequency ion trap.

The ion trap was invented by Wolfgang Paul, which was the subject of his 1989 Nobel prize [119]. The trap consists of electrodes held at a common RF voltage at frequency ω_{RF} . While at every single point in time, there exists an anti-trapping direction, there is a time-averaged effective potential due to the inhomogeneity of the field lines. Since the development of ion traps, they have been a workhorse for atomic physics experiments. The first laser cooling experiments were performed on trapped magnesium ions (Wineland et al. [120]) and trapped barium ions (Neuhauser et al [121]). Their use has found application in atomic clocks [122, 123, 124], mass spectroscopy [125], and quantum computation [126]. Additionally, they are being used to examine variations in the fundamental constants [127].

This chapter examines the quadrupole potential arising from the electrode con-

figuration. This quadrupole potential forms an effective potential that can be used to confine charged particles. The motion of such a trapped particle is essentially harmonic in nature. Finally, I present the design, fabrication and construction of an ion trap capable to be used in a cavity QED experiment.

4.1 Basis functions for the electric potential

The potential in a charge-free region is

$$\Phi(\mathbf{x}) = \frac{-1}{4\pi} \oint_S da' \Phi(\mathbf{x}') \frac{\partial G(\mathbf{x}, \mathbf{x}')}{\partial n'}, \quad (4.1)$$

where $G(\mathbf{x}, \mathbf{x}')$ is the appropriate symmetric Green's function that satisfies the Dirichlet boundary conditions [128]. The boundary surface consists of a set of electrodes each held at individual voltages U_k . Breaking the integral into a sum over the electrodes gives

$$\Phi(\mathbf{x}) = \sum_k V_k \left(-\frac{1}{4\pi} \oint_{S_k} \frac{\partial G}{\partial n'} da' \right) = \sum_k U_k \Theta_k(\mathbf{x}). \quad (4.2)$$

The finite set $\{\Theta_k(\mathbf{x})\}_k$ are the *basis functions* for the electric potential [129]. A particular Θ_k describes the potential in space due to 1 volt on the k -th electrode with all the other electrodes grounded. From superposition, the electrostatic potential can be reconstructed anywhere with the set of basis functions.

While it is difficult to analytically solve for the overall potential created in an ion trap, basis functions can easily be simulated. Each electrode is individually simulated to generate the set of basis functions. The results can be imported into MATHEMATICA or MATLAB for analysis.

A quadrupole ion trap has two electrodes of the same RF voltage, resulting in a potential

$$\Phi(\mathbf{x}, t) = \Phi_{RF}(\mathbf{x}, t) + \Phi_{DC}(\mathbf{x}) = V_{RF}(t)\Theta_0(\mathbf{x}) + \sum_{i \in DC} V_i \Theta_i(\mathbf{x}). \quad (4.3)$$

Here, Θ_0 is the basis function for the combined RF electrodes. In a quadrupole configuration, the RF potential has a nodal point where there is no electric field. Setting the RF node to be the origin, Taylor expand the RF potential about that point[128]. The RF and DC potentials are then

$$\Phi_{RF}(\mathbf{x}, t) = V_{RF}(t)\Theta_0(\mathbf{x}) \approx \frac{1}{2}V_{RF}(t) \left. \frac{\partial^2 \Theta_0}{\partial x_i \partial x_j} \right|_0 x_i x_j \quad (4.4)$$

$$\Phi_{DC}(\mathbf{x}) = \sum_{k \in DC} U_k \Theta_k \approx \left[\sum_{k \in DC} U_k \left. \frac{\partial \Theta_k}{\partial x_j} \right|_0 \right] x_j + \frac{1}{2} \left[\sum_{k \in DC} U_k \left. \frac{\partial^2 \Theta_k}{\partial x_i \partial x_j} \right|_0 \right] x_i x_j \quad (4.5)$$

Only up to the quadrupole moment has been kept, and the constant potential offset is dropped. In junction regions of linear traps higher order terms such as the hexapole moment are needed [130]. The linear term in the DC potential provides compensation for stray fields that offset the trap minimum from the RF node and give rise to excess micromotion. Compensation of the stray fields with the DC electrodes is important for a narrow atomic lineshape and optimal cooling [131].

Typical operation of ion traps has the RF and DC node aligned. The total potential can be written as

$$\Phi(\mathbf{x}, t) = \frac{1}{2}V_{RF}(t)Q_{ij}x_i x_j + \frac{1}{2}U_k D_{ij}^{(k)} x_i x_j$$

where $Q_{ij} = \partial_i \partial_j \Theta_0$ and $D_{ij}^{(k)} = \partial_i \partial_j \Theta_k$ are the quadrupole moments at the node.

The quadrupole moment Q is a symmetric, traceless, irreducible tensor of rank 2. Thus it is related to the spherical harmonics¹. In a basis where the tensor is diagonal, the RF potential is $\Phi_{RF} = \frac{1}{2}V_{RF}(Q_x x^2 + Q_y y^2 + Q_z z^2)$, where $Q_x + Q_y + Q_z = 0$. The equipotential surfaces at $\pm \frac{1}{2}V_{RF}$ are then described by the equation

$$Q_x x^2 + Q_y y^2 + Q_z z^2 = \pm 1,$$

¹Instead of Taylor expanding the potential about the node, one could perform a multipole expansion to get the moments $q_{\ell, m}$ and relate it to the non-zero elements of Q .

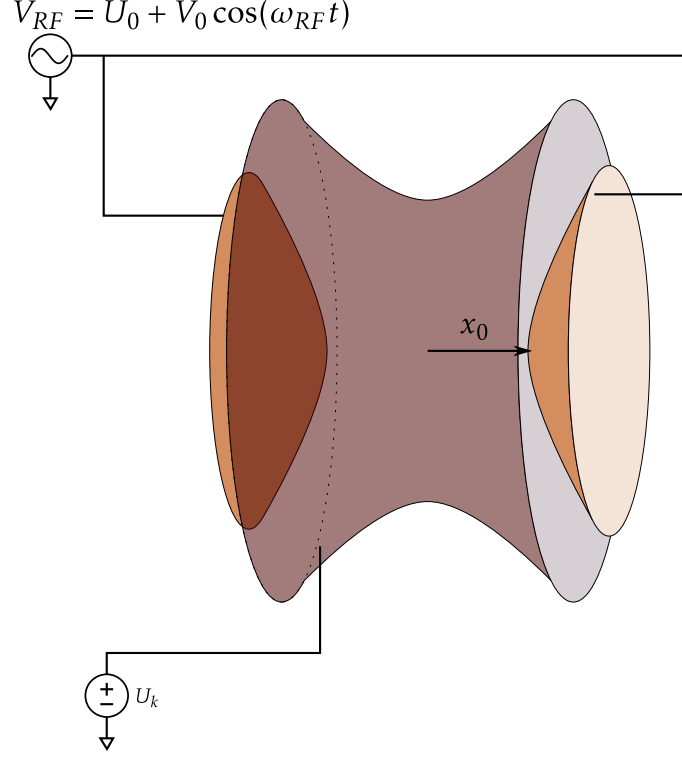


Figure 4.1: Figure for the ideal 3D quadrupole trap. The two endcaps have RF applied, while the ring is at ground. The distance from the RF node to the endcap is x_0 and $x_0\sqrt{2}$ to the ring (if cylindrically symmetric).

which is the equation for an hyperboloid. The coefficients define the characteristic distances of the hyperboloid $1/\sqrt{|Q_i|}$. We see that hyperboloidal electrodes satisfying the geometric constraints will give rise to a pure quadrupole field (Figure 4.1). This would be an ideal quadrupole ion trap with which we can compare a real trap. Take the x direction to be the direction toward the RF electrode as in Fig. 4.1 with x_0 the distance from the node to the RF electrode. Then the electrodes consist of a hyperbolic ring in the yz plane and hyperbolic endcaps along the x direction.

Ideally, the distance $1/\sqrt{|Q_x|}$ would be the distance from the RF node to the RF electrode. Define a factor $\eta = x_0^2 Q_x$ that rescales the real geometry of the trap to the ideal. Combining this result with an asymmetry factor $\alpha = Q_z/Q_x$, the potential

can be written as

$$\Phi_{RF} = \frac{\eta V_{RF}}{2x_0^2} [x^2 - (1 - \alpha)y^2 - \alpha z^2] \quad (4.6)$$

Here, η can be interpreted as the *voltage efficiency factor*. It tells us that a voltage V_{RF} on our (real) ion trap is *equivalent* to a voltage ηV_{RF} on an ideal hyperbolic electrode ion trap *of the same characteristic distance* x_0 . We can relate η to the RF basis function as:

$$\eta = x_0^2 Q_x = x_0^2 \left. \frac{\partial^2 \Theta_0}{\partial x^2} \right|_{\mathbf{x}_{\min}} \quad (4.7)$$

The asymmetry factor, α , describes how close the trap is to being symmetric in the yz -plane. If $Q_y = Q_z$, then $\alpha = 1/2$, and the trap would exhibit cylindrical symmetry. The diagonalized quadrupole tensor is then

$$Q = \frac{\eta}{z_0^2} \begin{pmatrix} 1 & 0 & 0 \\ 0 & -(1 - \alpha) & 0 \\ 0 & 0 & -\alpha \end{pmatrix} \quad (4.8)$$

The main purpose of simulation of the ion trap is to have an estimate of these two parameters, η and α . The voltage efficiency gives an indication of the amount of RF power is needed for a strong trap. The asymmetry is an indication of how close to degenerate the trapping frequencies are.

4.2 Motion of a charged particle in an ion trap

By driving the RF electrodes at radiofrequencies, a charged particle can be confined. To show this, we solve the equations of motion for an ion in this RF quadrupole field. To lowest order, the motion of the ion is equivalent to motion of a particle in a ponderomotive potential.

For a singly charged ion, the equation of motion is given by Newton's law, $m\ddot{\mathbf{x}} =$

$-e\nabla\Phi(\mathbf{x}, t)$. This leads to:

$$\ddot{x}_i + \frac{e}{m} \left[V_{RF}(t)Q_{ij} + U_k D_{ij}^{(k)} \right] x_j = 0 \quad (4.9)$$

where the (implicit) sum over k is over the DC electrodes, $D^{(k)}$ and Q are the quadrupole moments for the k -th DC basis function and the RF basis function.

We take the RF voltage to be $V_{RF}(t) = U_0 + V_0 \cos(\omega_{RF}t)$. In this case, the equation of motion becomes

$$\ddot{x}_i + \frac{e}{m} \left[V_0 Q_{ij} \cos(\omega_{RF}t) + U_0 Q_{ij} + U_k D_{ij}^{(k)} \right] x_j = 0 \quad (4.10)$$

It is useful to use a unit-less time $\tau = \frac{\omega_{RF}t}{2}$, as well as tensors a_{ij} and q_{ij} :

$$a_{ij} = \frac{4e}{m\omega_{RF}^2} \left[U_k D_{ij}^{(k)} + U_0 Q_{ij} \right] \quad (4.11)$$

$$q_{ij} = \frac{-2eV_0}{m\omega_{RF}^2} Q_{ij} \quad (4.12)$$

Then, the equations of motion are in a form similar to that of the Mathieu equation [132]:

$$\frac{d^2 x_i}{d\tau^2} + [a_{ij} - 2q_{ij} \cos(2\tau)] x_j = 0 \quad (4.13)$$

The matrices a_{ij} and q_{ij} couple the different degrees of freedom in our voltages. The DC voltages (including the DC on the RF electrodes) only appear in a_{ij} ; the RF voltage only appears in q_{ij} . If a_{ij} and q_{ij} were *both* diagonal, then the equation would be decoupled and the equations of motion will be the Mathieu equations. However, it is quite possible that the DC component (a_{ij}) will be diagonal in one particular basis, and the RF (q_{ij}) in another. This is the case when the DC electrodes are at a non-zero voltage.

4.2.1 The Mathieu equation Consider the case where the DC electrodes are all grounded. The matrix a_{ij} then only has the DC offset on the RF electrodes. Thus,

the RF quadrupole moment Q_{ij} is common to both a_{ij} and q_{ij} , allowing us to simultaneously diagonalize both a_{ij} and q_{ij} . In this diagonal basis, the different spatial degrees of freedom decouple and equation of motion becomes the Mathieu equation

$$\frac{d^2 x_i}{d\tau^2} + [a_i - 2q_i \cos(2\tau)] x_i = 0 \quad (4.14)$$

where $a_i = a_{ii} = 4eU_0 Q_i / m\omega_{\text{RF}}^2$, $q_i = q_{ii} = -2eV_0 Q_i / m\omega_{\text{RF}}^2$, and $Q = (\eta/x_0^2) \text{Diag}\{1, -(1-\alpha), -\alpha\}$. The Mathieu equation is a member of a general class of linear ODEs with periodic coefficients. By use of the Floquet theorem, the general solution to the Mathieu equation can be written as

$$x(\tau) = Ae^{\mu\tau} P(\tau) + Be^{-\mu\tau} P(-\tau) \quad (4.15)$$

where $P(\tau) = P(\tau + \pi)$ is a periodic function. Since it is periodic of period π , express it as a Fourier series $P(\tau) = \sum_n C_n \exp(i2n\tau)$. Hence, the general form for the solution is [133]

$$x(\tau) = Ae^{\mu\tau} \sum_{n \in \mathbb{Z}} C_n e^{i2n\tau} + Be^{-\mu\tau} \sum_{n \in \mathbb{Z}} C_n e^{-i2n\tau} \quad (4.16)$$

From this form, we see that the Mathieu exponent μ must be purely imaginary in order to have bound solutions. Plugging in $\mu = i\beta$ and equation 4.16 into the Mathieu equation (equation 4.14) yields the following difference equation

$$C_{n+1} - D_n C_n + C_{n-1} = 0 \quad (4.17)$$

where $D_n = \frac{a - (\beta + 2n)^2}{q}$. Dividing by C_n and solving for C_n/C_{n+1} and C_n/C_{n-1} , one finds

$$\frac{C_n}{C_{n+1}} = \frac{1}{D_n - \frac{C_{n-1}}{C_n}} \quad \frac{C_n}{C_{n-1}} = \frac{1}{D_n - \frac{C_{n+1}}{C_n}} \quad (4.18)$$

Noting that the denominator contains the left hand side shifted by one, the equation can be plugged into itself recursively to find

$$\frac{C_n}{C_{n+1}} = \frac{1}{D_n - \frac{1}{D_{n-1} - \frac{1}{\dots}}} \quad \frac{C_n}{C_{n-1}} = \frac{1}{D_n - \frac{1}{D_{n+1} - \frac{1}{\dots}}} \quad (4.19)$$

Using this in an expression for D_0 yields

$$D_0 = \frac{C_1}{C_0} + \frac{C_{-1}}{C_0} = \frac{1}{D_1 - \frac{1}{D_2 - \frac{1}{D_3 - \dots}}} + \frac{1}{D_{-1} - \frac{1}{D_{-2} - \frac{1}{D_{-3} - \dots}}} \quad (4.20)$$

Solving to lowest order in q , one finds

$$\beta \approx \sqrt{a + \frac{q^2}{2}} \quad (4.21)$$

and the motion is

$$x(t) \simeq X_0 \cos(\omega_s t) \left[1 - \frac{q}{2} \cos(\omega_{RF} t) \right] \quad (4.22)$$

where $\omega_s = \beta\omega_{RF}/2$ is the secular frequency. In terms of voltages and the RF quadrupole moment Q_i , the secular frequency is

$$\omega_i = \sqrt{\frac{eU_0 Q_i}{m} + \frac{1}{2} \left(\frac{eV_0 Q_i}{m\omega_{RF}} \right)^2} \rightarrow \omega_x = \sqrt{\frac{eU_0 \eta}{m x_0^2} + \frac{1}{2} \left(\frac{eV_0 \eta}{m\omega_{RF} x_0^2} \right)^2} \quad (4.23)$$

Stability of the motion is ensured in the regions of the (a, q) plane bounded by $\beta(a, q) \equiv 0, 1$. For the 3D quadrupole trap, there are two sets of curves: one pair for the radial motion, the other for motion along the trap axis (x). The total region of stability is plotted in figure 4.2.

4.2.2 Ponderomotive solution Despite the inability to (generally) diagonalize both a_{ij} and q_{ij} simultaneously, it is nevertheless possible to define principal axes for the ion trap where the motion is decoupled in a ponderomotive potential. Intuitively, the equation of motion appears like a parametrically driven oscillator. However, the parametric force is much stronger than the natural frequency. We still expect there to be two motional timescales—one at the RF frequency and one much slower. Thus, we look for solutions that have a large motion much slower than the RF plus some small motion that changes rapidly at the RF frequency [134].

Write the position as a sum of the slow (secular) motion and the micromotion, $x_j = u_j + \mu_j$. The micromotion term is assumed to be much smaller in magnitude

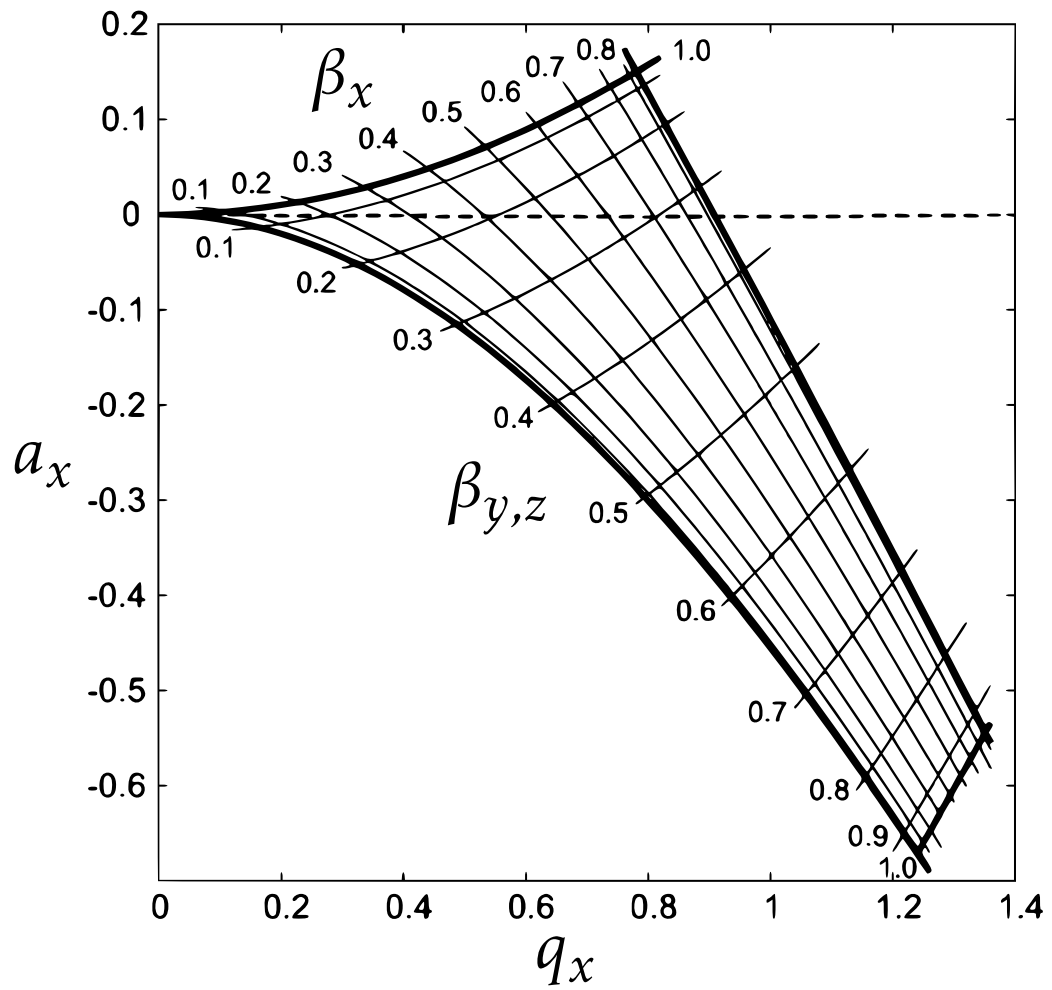


Figure 4.2: Stability diagram in the (a_x, q_x) plane for a 3D quadrupole ion trap. This figure here assumes cylindrical symmetry [133].

and oscillate much faster than the secular motion, so $\mu_j \ll u_j$ and $\ddot{\mu}_j \gg \ddot{u}_j$. With these two assumptions, break the equation of motion (equation 4.13) into a secular term and a micromotion term:

$$\frac{d^2 u_i}{d\tau^2} + a_{ij}(u_j + \mu_j) - 2q_{ij} \cos(2\tau)\mu_j = 0 \quad (4.24)$$

$$\frac{d^2 \mu_i}{d\tau^2} - 2q_{ij} \cos(2\tau)u_j = 0 \quad (4.25)$$

Equation 4.25 can be solved by assuming that u_j does not deviate appreciably in the time it takes μ_i to change. This is quite a valid assumption, as we have defined u_j as much slower than the RF frequency. Integrating equation 4.25 gives

$$\mu_i(\tau) = -\frac{1}{2}q_{ij} \cos(2\tau)u_j \quad (4.26)$$

Plugging this into equation 4.24 gives

$$\frac{d^2 u_i}{d\tau^2} + a_{ij}u_j - \frac{1}{2}a_{im}q_{mj} \cos(2\tau)u_j + q_{im}q_{mj} \cos^2(2\tau)u_j = 0 \quad (4.27)$$

Since the secular motion is assumed to be much slower than the RF frequency, we take the time averaged motion over a period of RF. Then, the equation of motion for the secular motion is that of a harmonic oscillator,

$$\left\langle \frac{d^2}{d\tau^2} u_i \right\rangle + \left[a_{ij} + \frac{1}{2}q_{im}q_{mj} \right] \langle u_j \rangle = 0 \quad (4.28)$$

The secular motion is then confined by an effective harmonic potential

$$U_{\text{eff}}(\mathbf{x}) = \frac{1}{2}mW_{ij}x_i x_j \quad (4.29)$$

where $W_{ij} = (\omega_{RF}^2/4)(a_{ij} + q_{ik}q_{kj}/2)$. The harmonic motion is decoupled along the eigenvectors of W . The corresponding eigenvalues of W are the square of the trapping frequency. Along the principal axes, the secular frequencies can be written as

$$\omega_i = \frac{\omega_{RF}}{2} \sqrt{a_i + \frac{1}{2}q_i^2} = \sqrt{\frac{e}{m} (U_n D^{(n)} + U_0 Q) + \frac{1}{2} \left(\frac{eV_0}{m\omega_{RF}} \right)^2} \quad (4.30)$$

With the DC electrodes grounded, this results in the same secular frequencies listed in equation 4.23. Hence, the ponderomotive solution is equivalent to the Mathieu solution for small stability parameters.

Using equations 4.5,4.4,4.11, and 4.12 the effective potential can be written as

$$U_{\text{eff}}(\mathbf{x}) = e\Phi_{DC}(\mathbf{x}) + \frac{e^2}{4m\omega_{RF}^2} |\nabla\Phi_{RF}(\mathbf{x})|^2. \quad (4.31)$$

This effective potential is the potential that provides confinement of ions. When designing a new trap we would like to know the shape of the effective potential—particularly the trapping frequencies, the weakest direction, and the voltage efficiency factor.

4.3 Ion trap for enhanced light collection

The light collection models described in the previous chapter III require an optically open ion trap that does not obscure the light. Additionally, the ion position must be precisely placed inside the cavity mode. The ion trap described in this section accomplishes this goal.

The ion trap consists of two identical laser machined alumina substrates with lithographically patterned electrodes. Each substrate is mounted on a linear positioner inside the vacuum chamber such that the position of the ion trap can be placed *in situ* [135].

Figure 4.3a is a photograph of a finished substrate. Each substrate is laser machined to a narrow finger approximately 300 μm wide. This finger is further machined into three individual tines, as illustrated in figure 4.3b. The outer tines are approximately 100 microns wide and the center tine is approximately 50 micron wide. The gaps between the tines are about 25 μm , and the tips are beveled on both sides to provide a small face to the ion. The back portion of the electrodes pro-

vides enough space for onboard RF filters, allowing DC compensations voltages to be applied for micromotion compensation .

Initially, the edges of the substrates came to relatively sharp corners (see figure 4.3a). However, these corners provided a stress point whereby the substrates routinely fractured in fabrication and assembly. In the second iteration, we had large rounded corners that aided the structural strength of the substrate.

4.3.1 Simulations Prior to fabrication and assembly, the basis functions of the trap design were extracted from electrostatic simulations of the trap. The simulations were performed in CPO, a charged particle optics simulation program. The program provides a boundary element modeling of the electrostatic potential due to the electrode configuration. Electrostatic simulations are justified as the trap size (100–200 μm) is much smaller than the wavelength of the radiofrequency voltage applied (typically 5–10 meters).

These simulations provide us with basis functions for the trap that can be used to estimate parameters such as the secular frequency, the voltage efficiency factor, and the trap depth. MATLAB functions parse the output files of CPO, extracting the RF pseudopotential and the basis functions of the DC compensation electrodes. Figure 4.4 illustrates the resultant RF pseudopotential generated from the RF basis functions for an electrode spacing of $2x_0 = 180 \mu\text{m}$. From these simulations, the designed ion trap has a voltage efficiency factor of $\eta_{rf} = 0.451$, which peaks at an ion–electrode spacing of $50 \mu\text{m}$. Figure 4.8 illustrates the results of the simulations and comparison with the experimentally derived values.

The influence of nearby dielectrics on the trapping potential can be seen in the simulations. Due to the electromagnetic boundary conditions, the normal component of the electric flux density is continuous given no surface charges. Therefore, given

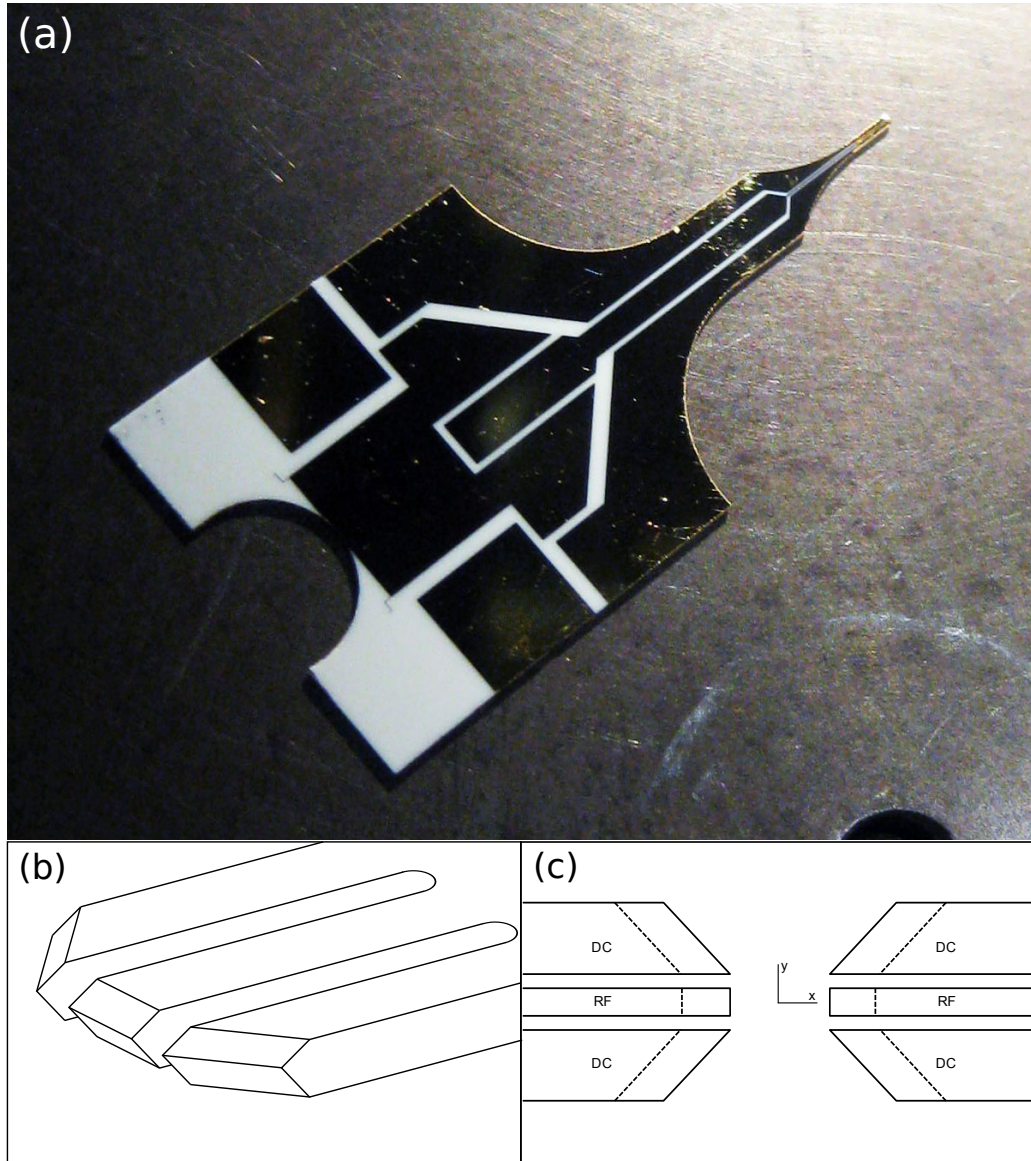


Figure 4.3: Here is the geometry for the double-fork ion trap that has been engineered to place an ion within a small optical mode volume. **(a)** Photograph of a gold-pattered substrate. This is the initial design of the substrate with sharp corners. These were the main failure points. **(b)** Sketch of the relative placement of the ion trap. The two substrates have three small tines at the very edge. The two electrodes are placed facing tip to tip approximately $200\ \mu\text{m}$ apart.

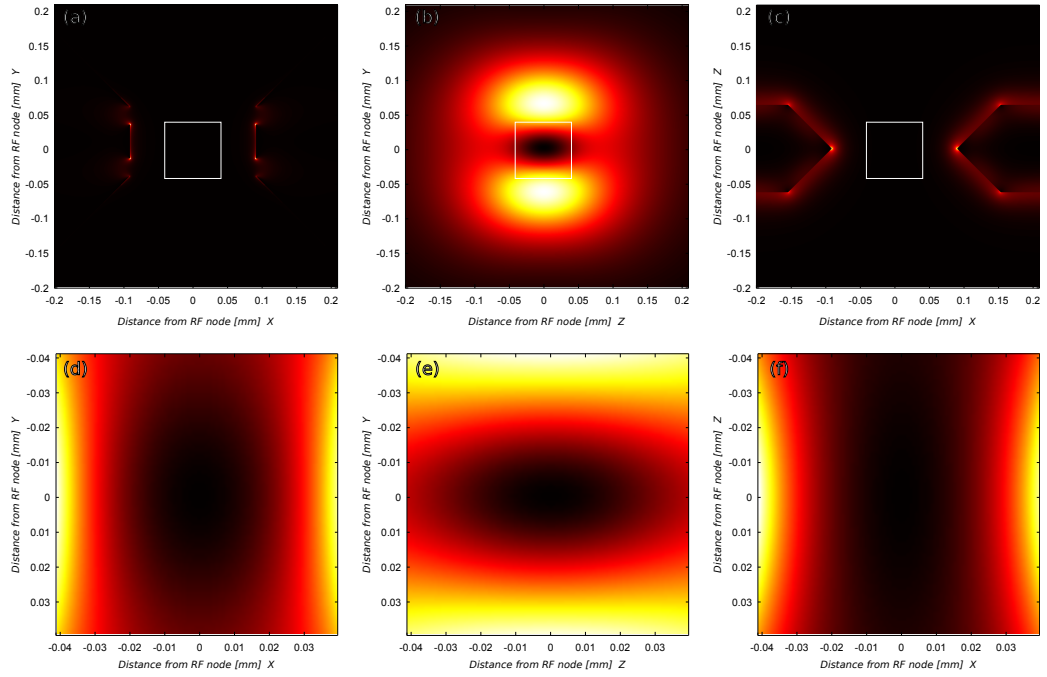


Figure 4.4: RF Ponderomotive potential for electrode spacing $2x_0 = 180 \mu\text{m}$. The coordinate system for the experiment is as follows: trap axis is x , imaging direction is y , and cavity axis is z . (a)–(c) Large view of the ponderomotive potential in the xy , zy , and the xz plane, respectively. The RF node is located at the origin. (d)–(f) Zoom in plot of the ponderomotive potential, showing the harmonic trap. The zoomed in region is denoted by the square in the above image.

a relative dielectric constant ϵ_r , the electric field from the trap along the cavity axis is increased. CPO, however, does not provide the influence of charge buildup on the mirrors, which is the main concern about nearby dielectrics [136].

4.3.2 Fabrication and Construction After laser machining of the ion trap substrate, they must be processed in a clean room in order to lithographically define the gold electrodes. The laser machining process utilizes a CO₂ laser for rough cutting of the shape and an excimer laser for the fine details such as the tines. The CO₂ cuts can leave burrs on the substrate, which must be removed prior to processing. To remove the burrs, drag a razor blade across the surface.

Additionally, there typically is a residual emulsion layer on the substrate from the machining process. Ostensibly the emulsion is water soluble, however experience has shown that the one must spend time cleaning the substrate with acetone, methanol, and isopropanol to remove the residue. Delicate scrubbing with swabs must be performed on the substrate as well to ensure the cleanliness. Always swab from the center of the substrate outwards.

While it is unknown if this next step is necessary, the substrate is then placed in a plasma RIE with an O₂ descum to clean any unseen organic residue. The next step is to perform the lithography. The first side that is coated is the backside of the substrate, where only part of the tines are exposed for gold coating. The backside is coated in order to ensure a gold coating around the tip of the substrate that faces the ion.

Since the features of interest in the lithography are at the tips of the fine tines, a process must be developed in order to surmount the difficulty of edge beading from the photoresist. The recipe to pattern the electrodes is outlined in table 4.1.

First the substrate needs to be affixed to a wafer. The wafer provides a large

Step	Description
1	Heat Si wafer at 120 °C
2	Spin NR7-3000PY on wafer, recipe 6 (4000rpm/60s)
3	Place substrate on wafer
4	Bake at 120 °C for 120 sec
5	Spin NR7-3000PY on wafer+substrate, recipe 6 (4000rpm/60s)
6	Bake at 120 °C for 120 sec
7	Expose for 30 sec
8	Bake at 120 °C for 120 sec
9	Develop in RD6 for 90 sec–120 sec (backside) or 25 sec (topside)
10	Run DescumRG on the RIE for 60 sec
11	Evaporate 200 Å Titanium, then 5000 Å–10.000 Å Gold
12	Liftoff with RR2
13	Clean substrate
14	Package

Table 4.1: Steps for the lithographic process in order to pattern gold on one side of the substrate.

surface for holding the substrate, protection of the delicate tip, as well as means for the resist to move off the tip. A clean wafer is warmed on a hot plate at 120 °C for several seconds. A layer of Futurrex NR7-3000PY is spun onto the wafer at 4000 rpm for 60 sec². The substrate is placed on top of the resist and then the wafer is baked on a hot plate at 120 °C for 2 min. Next several drops of resist (NR7-3000PY) are placed on the surface of the substrate, and then the wafer is spun at 4000 rpm for 60 sec. Afterwards the resist is baked again at 120 °C for 2 min.

The resist used is a negative resist, which means that the portions that are exposed to UV light under to contact aligner stay after development. The wafer is exposed for 30 sec and then baked on the hotplate again for 2 min at 120 °C.

For the backside, the mask used is simply a shard of a wafer, and can be aligned over part of the tines by hand with tweezers while looking under the microscope of the contact aligner. The topside uses a mask. Be sure to use the aligner in soft contact setting. This will prevent the contact aligner from creating a vacuum between the mask and the wafer to physically contact the two. Otherwise, there is

²This photoresist is no longer being manufactured by Futurrex. The replacement, NR71-3000PY does *not* work with this process. From what I've been told, avoid this resist as it does not work very well at all. I've been told to try the NR9 photoresist, which should have better adhesion [137].

a possibility that a substrate will crack (usually on a tine). Because the features of the lithography are large, the mask doesn't have to be very close to the substrate.

After the post-bake, the wafer is then developed in Futurrex resist developer RD6. For the backside, I found that leaving the wafer in the resist for 1.5 min resulted in most of the resist at the tip of the tine to be developed, allowing gold deposition. The drawback is that gold will get stuck between the tines and the edges. For the topside, development only needs to last for 25 sec, as we are only interested in developing the top. Next rinse the wafer under water for 2 min, and blow dry.

The wafer is then placed in a plasma RIE and another descum is run in order to remove organic residue. Afterwards, the trap is placed in the evaporator, where 200 Å of titanium is deposited, followed by 10 000 Å of gold (5000 Å of gold has also been done).

After the evaporation, the wafer is placed into a hot bath of Futurrex resist remover RR2. The bath is heated on a hotplate to above 75 °C. Although the remover works faster at high temperatures, 89 °C is the flashpoint and therefore care must be taken. While the surface of the wafer will be cleaned quickly, it takes time for the remover to eat through the layer of resist bonding the substrate to the wafer.

Once the substrate and wafer are clean of resist, they are cleaned in water and organic solvents in a similar manner to the beginning. Often, there is some gold stuck between the tines of the trap. These are removed with a combination of the acetone airbrush and light swabbing.

The trap is checked for shorts and then packaged. Back at the lab, it is prepared for cavity installation. A resistive π -filter is wirebonded onto the substrate. The two capacitors have a 1000 pF capacitance, and the resistor is 1 k Ω . Gold ribbons with kapton wires spot-welded together are then wirebonded to the substrate. The

substrate is then ready for installation.

4.3.3 Testing of the ion trap The trap RF is generated from an HP8640, and is amplified by a MiniCircuits amplifier ZHL-5W-1, which can deliver up to 5 W to the resonator and trap. Typical operation of the trap is at 480 mW of RF at 39.6 MHz. The RF is sent to a bifilar helical resonator attached directly to the RF feedthrough on the chamber [138, 139, 122].

The resonator is formed from a copper tube with a helical coil inside (figure 4.5). One end of the coil is attached to the can (or DC supply) and the other end is attached to the chamber. The resonator is excited inductively with an antenna and is adjusted to be critically coupled. The lowest order resonant frequency provides a high voltage at the tips of the trap electrodes.

We initially used a bifilar helical resonator of resonant frequency 39.6 MHz which had a loaded Q of 225. The trap characterization was performed with this resonator. Later, we found the ion had large excess micromotion which was mitigated by changing the resonator. The second resonator was a monofilar resonator with a resonant frequency 27.6 MHz and had a loaded Q of 150.

The voltage on the trap is $V \propto \sqrt{PQ}$, where the proportionality constant depends on the geometry of the resonator. Typically it is on the order of $20 \Omega^{1/2}$.

We monitor both the input and reflected RF powers with a directional coupler. The coupled ports have negative crystal detectors (HP8472B) which convert the RF power into a DC voltage. The voltage levels have been calibrated for both power to voltage (Figure 4.6a), and for power delivered to the load to voltage from the coupled port (Figure 4.6b).

The trap was first tested under vacuum with $^{174}\text{Yb}^+$ ions. In order to load reliably, a negative bias voltage of -15 V was applied to the RF electrodes. The secular

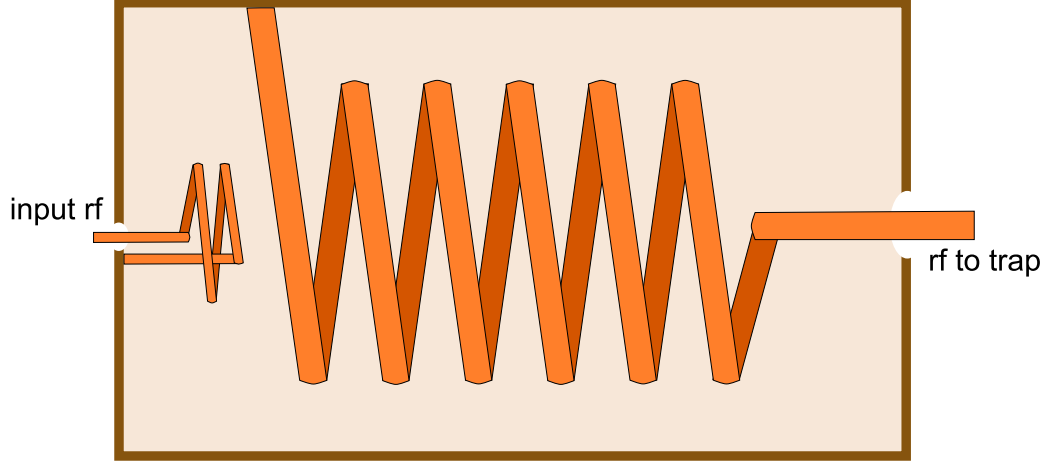


Figure 4.5: Drawing of a monofilar helical resonator. The input RF is coupled to the large coil through their mutual inductance. Since the resonator is at a quarter-wave, the low voltage at the input side is maximal at the trap. In our experiments, we used both a bifilar and monofilar resonator.

frequencies of the trap were then measured by applying an AC voltage on one of the compensation electrodes. The frequency of the AC voltage is slowly swept across several megahertz while the ion is observed on a CCD camera. When the frequency hits a resonance, the ion gets hot and is observable on the camera.

We measure the secular frequencies of the trap in the x and z direction versus the bias voltage. From equation 4.23, the square of the secular frequency is linear with the bias voltage. By performing this measurement for various bias voltages the secular frequency, RF voltage, and trap asymmetry can be extracted.

Figure 4.7 illustrates the result of the secular frequency measurements for bias voltage, ion–electrode distance x_0 , and direction (x or z). By fitting to the model in equation 4.23, we extract the voltage efficiency factor η_{RF} versus trap separation and compare it to the CPO simulations (Figure 4.8).

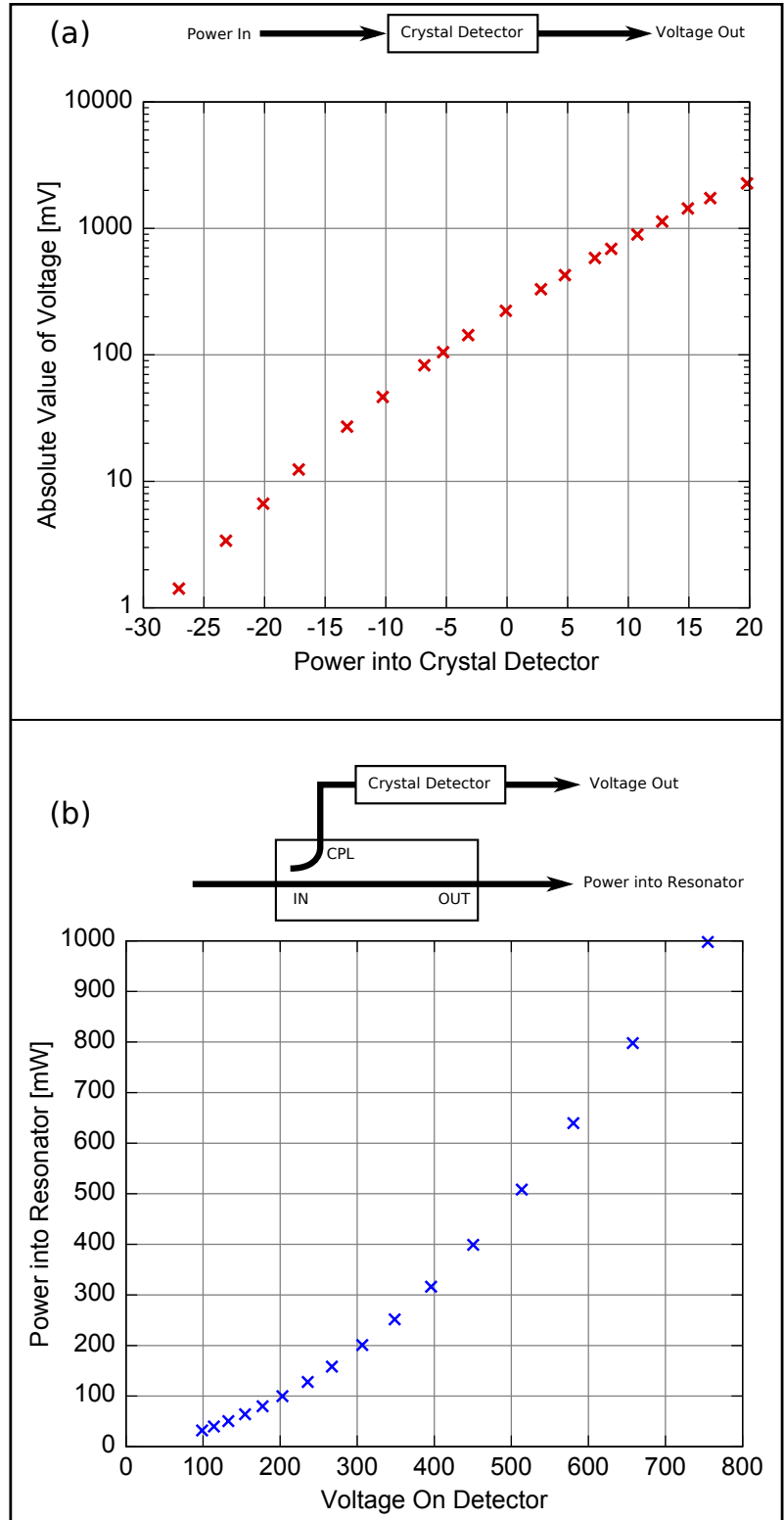


Figure 4.6: Calibration of the HP8472B Crystal detector. (a) Voltage output of the detector as a function of the input power. (b) Power on the output of directional coupler versus measured voltage from the RF on the coupled port.

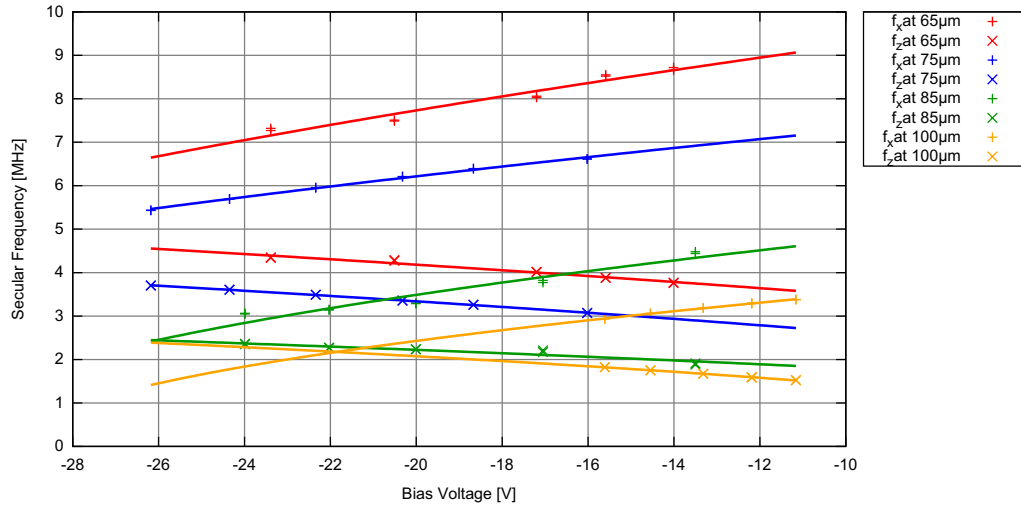


Figure 4.7: Measured secular frequency versus bias voltage. Linear fits to the square of the frequency measurement allow extraction of quadrupole parameters.

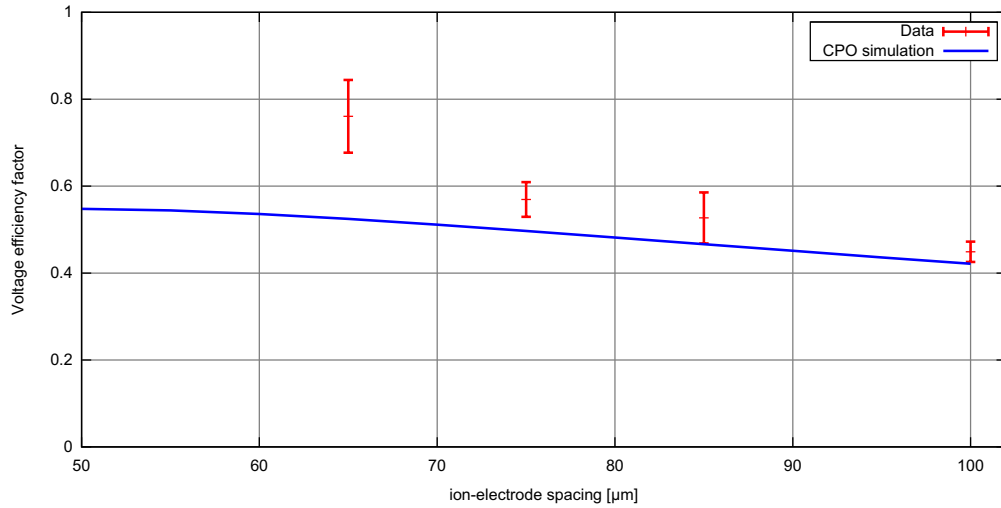


Figure 4.8: Measured and simulated values for the voltage efficiency factor versus trap separation. Typical operation point for the trap is at $x_0 = 90 \mu\text{m}$, which is larger than the size of the cavity mode.

CHAPTER V

Experimental System

The experimental apparatus was designed around the use of an optical cavity in order to collect photons from a single trapped ion. The ion must be placed inside the optical mode, which is defined by the line between the centers of curvature of the two mirrors. For the ion to reside in the mode, its position must lie along this line.

From chapter III, a large cooperativity is highly desirable. This can be accomplished with a small mode volume and a high finesse cavity. To achieve this highly reflective dielectric mirrors would have to be close to the ion. The size of the cavity is limited by charging of nearby dielectrics. Harlander et al. have observed charging influences when the distance from the ion to the dielectric is within an order of magnitude of the characteristic ion–electrode distance x_0 [136]. Our adjustable ion trap will allow us to have ion trap sizes much smaller than the ion–mirror spacing.

This chapter presents the current efforts towards an improved collection efficiency with a trapped ion in a cavity. After detailing the design, fabrication, and testing of our trapped ion cavity QED system, we demonstrate enhancement of scattering of photons into the cavity solid angle.

5.1 UHV Chamber

The ion trap is housed in an ultrahigh vacuum chamber, where the pressure is less than 100 pTorr (13 nPa) at the ion gauge. Electrical feedthroughs allow the application of voltages and current to the chamber. The chamber is a Kimball Physics 4 inch spherical octagon (Figure 5.1). The cavity and the linear positioners for the trap occupy half the available ports on the side of the chamber (figure 5.1b). RF is applied from a separate feedthrough, isolating it from the DC compensation voltages to avoid pickup and accidental shorting. With one of the small 1 1/3 inch ports to pull vacuum, there remains two feedthroughs to pull out the 10 wires—6 for compensation, two ovens, two for the piezo.

To achieve an optimal image with the microscope objective, a re-entrant viewport is used above the trap for imaging (figure 5.1c). The viewport has been designed to allow beams at nearly 45 degrees pass through the center of the chamber, skimming past the objective. On the bottom, a regular viewport is used, as it provides the extra room needed to fit the ytterbium ovens.

The main part of the chamber is assembled according to a particular order of operations. First, the ovens are installed. Next are the big copper wires for the RF. These wires take the RF from the feedthrough and take it most of the way to the delicate substrates. Constantan flags are spot-welded onto the wires, providing a good surface for spot-welding.

The substrates, after wirebonding, are then attached to the linear positioner *outside* the octagon. A rig consisting of 8020 and a Teflon surface is used to hold the linear positioners in place while the substrates are attached *outside* the octagon. The rig stabilizes the positioner while the substrate is slowly inserted into the octagon.

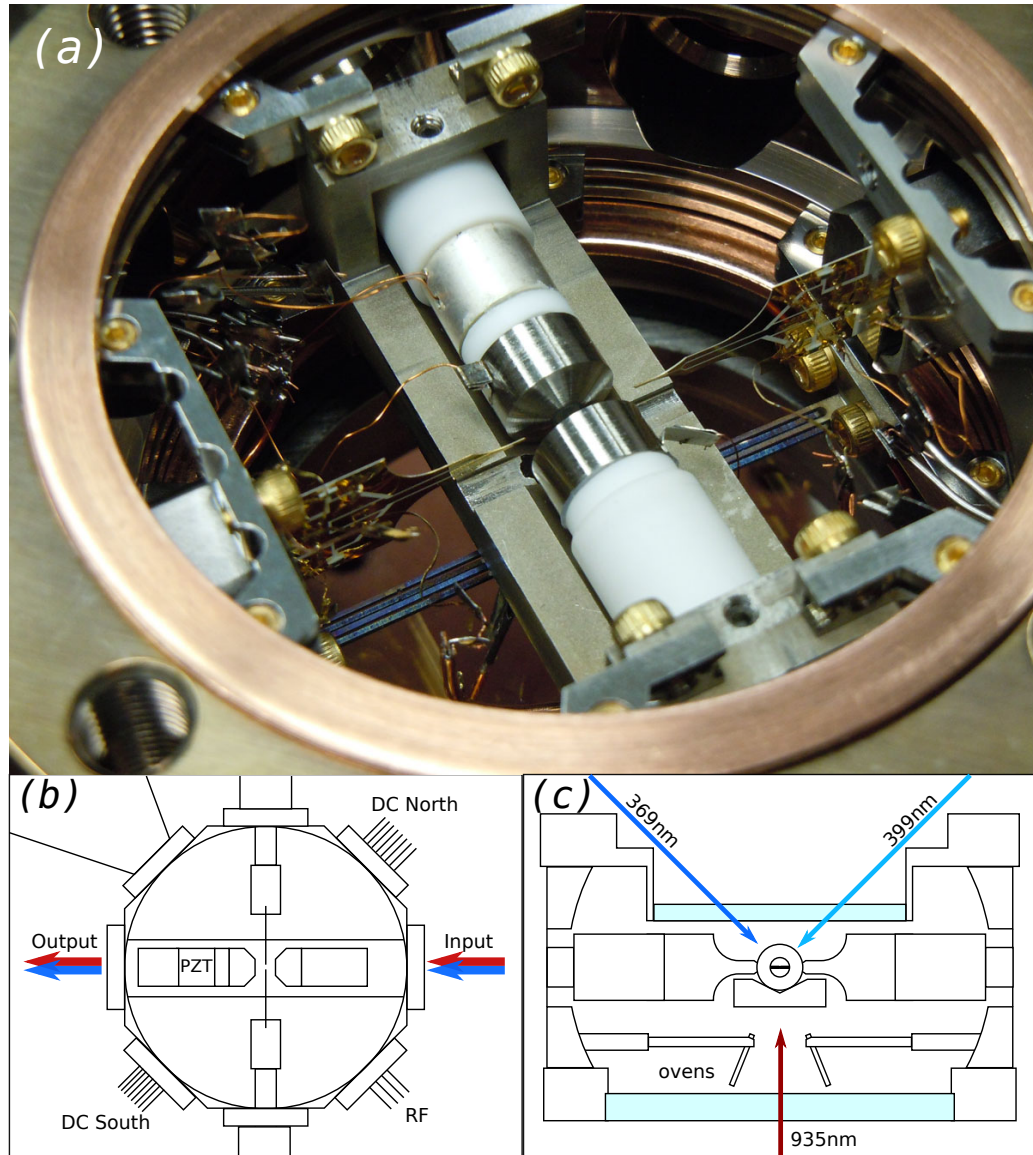


Figure 5.1: The ion-cavity vacuum chamber. **(a)** Photograph of the interior of the spherical octagon housing the ion-cavity system. The ion trap is held by linear positioners so it can be placed inside the cavity. **(b)** Top view schematic of the ports on the spherical octagon. **(c)** Side view schematic looking down the cavity axis. A re-entrant viewport is used on the top for imaging. The extra room provided by the regular viewport is needed for the ytterbium ovens

Materials	Pulse 1	Pulse 2
Gold to Constantan	13%	10%
Constantan to 34 AWG kapton wire	30%	25%
Constantan to 32 AWG Copper wire	30%	25%
Constantan to 18 AWG Copper wire	50%	75%
Constantan to feedthrough	30%	25%

Table 5.1: Spot-welding parameters

Once inside the octagon, the arms can be attached. As the substrate is inserted, the wires must be inserted into the port first. The reason for attaching the substrate outside the chamber is because it is quite difficult to insert the substrate into its clamp inside the octagon without breaking it. Once the substrate is installed, then the wires are spot-welded to the feedthroughs, and the ground wire is attached to the chamber. Finally, with the substrates retracted (leaving a two-inch gap), the V-block containing the cavity is installed. This is the last step so that there is room to maneuver the wires of the substrate for spotwelding. Once the V-block and cavity are in place, the piezo and sheath wires are spot-welded. Final adjustments to the cavity position and length are made at this point. We ensure that the cavity resides in the center of the chamber, and estimate the cavity length with a reticle.

Table 5.1 lists the various power settings used for the various spot welds. The two power settings are for the two pulses used in the weld. The surface of the weld must be clean in order to have a good weld. The quality of the weld relies upon the cleanliness of the surfaces and welding electrodes, as well as the power and the force used.

After closing up the chamber, it is inserted into the oven and pumped down on a turbo pump (which also has a roughing pump for the first stage). Final checks of electrode connectivity is made. Capacitances and resistances of each feedthrough pin are measured with respect to ground and the RF, as well as any other suspicious inter-pin connection. To ensure that the feedthrough pin is connected to the substrate, a

rise-time measurement is performed. A 1 V square wave is applied to the pins, and the rise time is measured. Given the resistive π -filter on the substrate, the rise time should be 11 μ sec. If the rise time is not around this value, then there is an issue with the connection.

After verification of the wiring the ovens, sublimation pump, and ion gauge are degassed. To degas the ovens, a 2 A current is applied to each oven for 90 sec. The ion gauge can simply be degassed by pressing the degas button on the controller. The gauge should automatically turn off after several minutes. The gauge can only be degassed if the local pressure is below 1 μ Torr. Finally, the sublimation pump is degassed. The method of degassing is to apply 15 A for 90 sec on each filament, then stepping up to 30 A and finally 45 A.

The oven is then turned on to 82 °C (180 °F, the lowest temperature the oven can regulate. It is slowly brought up to temperature over several hours. Typical chambers are baked at 200 °C for approximately one or more weeks. Due to the presence of mirrors, the cavity chamber was initially baked at 150 °C. However, we found that at this temperature, the piezo failed. In the second iteration, the chamber was baked at a more modest 110 °C for several weeks.

Once the temperature of the oven gets above the boiling point of water, the valve on the large ion pump is opened and the turbo pump is valved off. After the oven has been on the final temperature for several days and the pressure has equilibrated, the internal pump is turned on. When the chamber is ready to be brought back to room temperature, the bakeable valve is closed hand-tight. At this point, the large pump can be valved off. Again, the temperature is brought down slowly.

Since the oven cannot regulate temperatures below 82 degrees, it is usually turned off at that point. With the oven door closed, the air temperature of the oven drops

by 0.16 degrees Celsius per minute ($9.6\text{ }^{\circ}\text{C h}^{-1}$). Often, the point to turn off the oven is late at night so that the next morning the chamber is mostly at room temperature (usually it is warm to the touch). At this point the doors are opened until the chamber is fairly cool. The bakeable valve is finally closed with a torque wrench to the previous torque value. The chamber can then be disconnected and removed from the oven and placed on the optical table.

5.2 Laser system

The laser system is illustrated in figure 5.2. A Toptica TA100 tapered amplifier diode laser at 739 nm outputs 300 mW of optical power at 405 645.7 GHz. There is a 2 mW leakage beam between the master oscillator and the tapered amplifier, which is coupled into a fiber and sent to the High Finesse wavemeter. Additionally, the light for a monitor cavity, the Pound–Drever–Hall cavity, and the ion-cavity are all leakage beams from mirrors in the setup. These typically have powers less than 1 mW. A half-wave plate and a polarizing beam cube serve as a pickoff of 5 mW for our iodine setup. The rest of the beam is coupled into a Spectra-Physics Wavetrain doubler, which typically generates 10 mW of ultraviolet light at 369 nm.

The TA100 is locked to a passive Invar cavity through the Pound–Drever–Hall technique. The current of the diode laser is modulated at 29.8 MHz, generating the sidebands necessary for locking the laser to this cavity. The passive cavity is stabilized for slow drifts to an iodine line 12.070 GHz from the desired frequency. To reach the iodine resonance, we modulate the light going into the iodine setup with a fiber electro-optic phase modulator. More details of this scheme are presented in references [17, 140].

The Wavetrain generates vertically polarized ultraviolet light. Using a waveplate

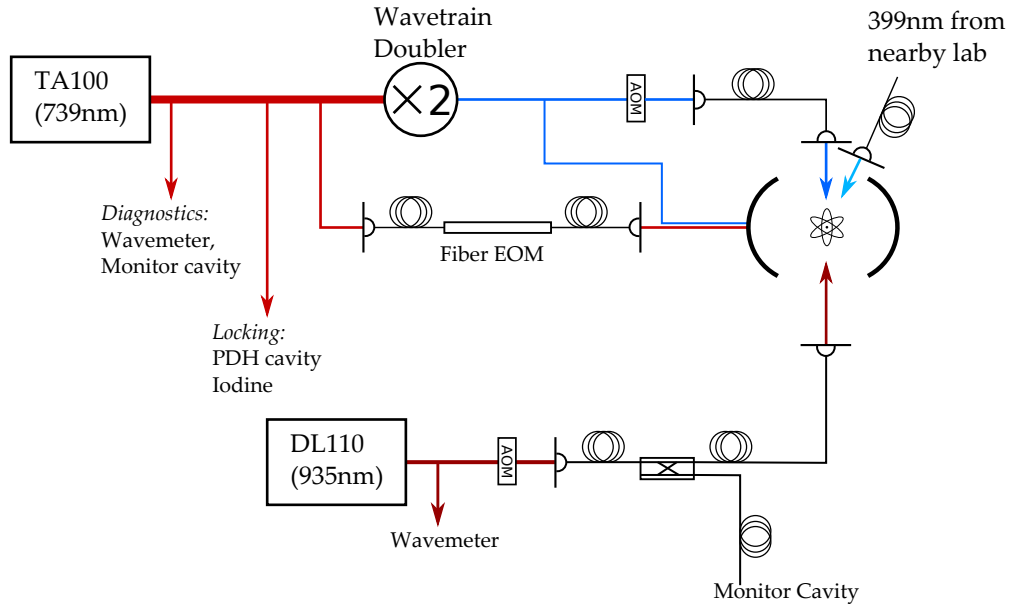


Figure 5.2: Schematic of laser layout for the cavity experiment. Testing the trap at the focus of the mirror did not have the cavity coupling light.

and polarizing beam splitter, a small fraction of the light is sent to the cavity. This light is coupled to the cavity to ensure that the cavity is locked to the proper line as well as to occasionally provide cooling in the cavity direction. The rest of the light is sent to an Isomet acousto-optic modulator where it is upshifted by 130 MHz and coupled into a single mode fiber and sent to the trap. The output of the fiber is a MicroLaser Systems fiber collimator FC-10, which has a 10 mm output lens. The position of the lens can be adjusted to collimate or focus the beam. With this lens, the UV light is focused to a spot size of $\approx 10 \mu\text{m}$. This light is used to excite the ion from the side of the cavity.

The 935 nm repump light is generated from a Toptica DL110 and is locked to the wavemeter at 320 571.74 GHz. After a small pickoff for the wavemeter, the beam is sent through an acousto-optic modulator, where it is upshifted by 225 MHz, and coupled into a fiber beamsplitter. Here, it is combined with the 639 nm light sent from another lab, which is used to depopulate the F state of the ion. The beamsplitter

couples sends approximately half the light to the trap and the rest to a monitor cavity. Typical operation sends 2 mW of infrared light into the chamber, which is slowly focused through the trap region.

The final laser used is a 399 nm diode laser, which also comes from a nearby lab across a fiber. Around 700 μ W is necessary in order to load an ion in 3–5 min.

5.3 Imaging System

The imaging system means to observe the ion as well as detect scattered photons. The first instrument is a microscope objective from CVI Laser. It is an infinity corrected objective with a numerical aperture $NA = 0.23$ ($f/\# = 2.1$). The effective focal length is 20.8 mm. In our configuration, the front focal length is 14.9 mm, with a working distance of 13 mm. The back focal length is 15.6 mm. These values are found using the index of refraction of air and fused silica at 369.5 nm: $n_{air} = 1.000275$, $n_{fs} = 1.473906$. Due to the relatively large numerical aperture, the location of the best image can be quite different from the paraxial solution. The imaging system is therefore simulated in OSLO, an optics design program. The imaging system design is to get the best point-spread function. Figure 5.3 illustrates the imaging system used in the experiments.

The objective is in an infinite-conjugate ratio, meaning that the best image occurs with the object at the front focal plane, and the image at infinity. The viewport on the vacuum chamber is several millimeters thick and resides between the object (ion) and the objective. This naturally introduces spherical aberrations, which can be compensated by the position of the objective. The optimal point is then pulled in from infinity. For the re-entrant viewport, the thickness of the glass is about 3.3 mm, and the optimal point forms an image approximately 500 mm away from the back

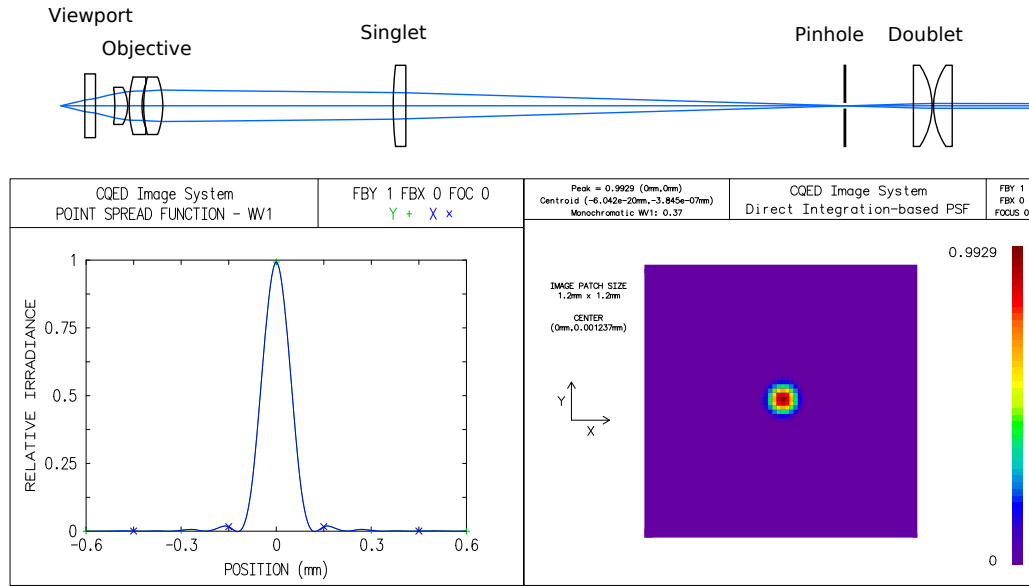


Figure 5.3: Imaging system used in the experiments. The ion is imaged through a 3.3mm reëntrant viewport by an infinite conjugate ratio objective. Due to space constraints, a singlet lens is used to pull the intermediate image plane to a reasonable distance. At the intermediate image is a 400 μm pinhole to spatially filter the background light. The intermediate image is then imaged by a doublet lens onto the CCD (not shown). The bottom illustrates the calculated point-spread functions for the imaging system.

face of the objective. Due to space constraints, a singlet lens ($f = 20\text{ cm}$) is placed after the objective to pull the image plane to a reasonable position. The distance between the ion and the objective as well as objective to singlet can be adjusted for an optimal point-spread-function.

At the image plane is a pinhole for spatial filtering. When adjusting the geometry of the trap, a 900 μm pinhole is used. However, when looking at photon counts from the ion, a 400 μm pinhole is used. This smaller pinhole cuts down on the background counts that come from laser scatter off the trap electrodes. The field of view for the 900 μm pinhole is 110 μm , giving a magnification of 8 for the first stage.

A doublet is placed 22 mm from the pinhole, and images it onto the CCD camera. The doublet is formed from two stock 50 mm lenses from Precision Photonics. The effective focal length of the doublet is 24.4 mm, with a FFL of 20.2 mm. The overall

magnification of the imaging system is ≈ 50 .

The imaging system is constructed out of ThorLabs lens tubes to minimize the background light entering imaging system. The objective is attached to a 3 in lens tube with at stock Precision Photonics 20 cm plano-convex lens at the end. After a 6 in tube, a zoom mount is attached containing the pinhole. This mount allows the adjustment of the distance from the pinhole to the doublet. The doublet is housed in a 1 in lens tube attached directly to the zoom mount. Attached to this tube is a SemRock 370 nm band-pass filter to help filter out the 935 nm light that is directed along the optic axis. This whole setup is attached to an XYZ translation stage to adjust the position and focus of the viewing area. The rest of the imaging system consists of a couple of mirrors in a lens tube system to direct the image onto a CCD camera. One of the mirrors is on a flip mount so the light can be directed onto a Hamamatsu H8259-01 PMT. The PMT is used to detect the number of photons emitted by the ions and has a quantum efficiency of $\approx 20\%$.

5.4 Mirror Experiment

Before attempting experiments with the cavity, the ion trap was first tested with a 5 mm radius of curvature mirror. The mirror was placed 2.5 mm away from the trap, allowing the ion to reside near the focus of the mirror. The numerical aperture of the mirror is $NA = 0.8$.

We were able to trap ions and test the ion trap, performing the trap characterization measurements. However, we were unable to observe any fluorescence from the ion along the mirror axis, due to significant laser scatter off the electrodes (Figure 5.4).

The main issue for this experiment was that both the ion trap and mirror were

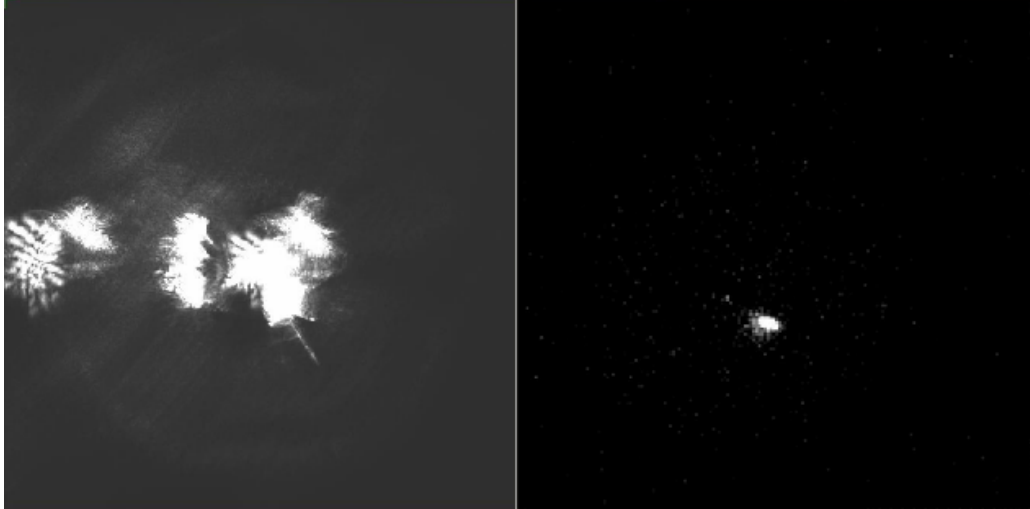


Figure 5.4: Image of the mirror on a CCD camera looking down the optic axis of the mirror (*left*). The dominant source of light is laser scatter from the trap electrodes. This image was taken while an ion was trapped as evidenced by the image on the right. The scatter from the electrodes could not be minimized.

not designed for this particular experiment. The ion trap was designed to be very small as it would be near dielectrics. However, for this experiment, the mirror was significantly far away, and the trap did not behave well at larger separations. The main limitation for the trap was most likely the amount of RF power that can be applied. At larger distances, both the depth and voltage efficiency suffer, and hence demand a much larger voltage. Therefore, the trap was limited in size, creating a lot of laser scatter. This laser scatter was efficiently collected by the mirror, blinding our detector.

5.5 Optical Cavity

Photon extraction for quantum networks does not require the ion-cavity system to be in the strong coupling regime. In fact, it is desirable to work in the bad-cavity limit, where $\kappa \gg g \gg \gamma$. In this regime, the rate of scattering into the cavity mode is greater than out the side of the cavity, implying a large single-atom cooperativity is desirable. Additionally, a large κ ensures that any photon in the

cavity will exit the cavity before being reabsorbed by the atom. To reach this regime experimentally, the cavity mirrors must be fairly transmissive, and the mode volume must be small. Additionally, since the collection efficiency is proportional to the ratio of the outcoupling transmission to the total losses, the outcoupling mirror is designed to have a larger transmission.

There are three design parameters for an optical cavity: the losses (or finesse), the cavity length, and the curvature of the mirrors. The losses only influence κ , while the other two affect the mode volume V . The length is limited by the ion trap and dielectric charging, while the other two are technical issues with the dielectric materials and the coating methods.

The highest quality coatings we could find were from Advanced Thin Films, which had absorption and scattering losses at 369 nm of ≈ 300 ppm. This limits the finesse to $\mathfrak{F} < 10\,000$. The target transmissions for the optical coatings were 200 ppm and 700 ppm at 369 nm, which would give an outcoupler efficiency $T_2/\mathcal{L} \approx 47\%$ and a finesse of $\mathfrak{F} \approx 4000$. Because our ultraviolet light is derived from frequency doubling infrared light at 739 nm, the mirrors were coated at 739 nm as well such that we could lock the cavity with the fundamental beam.

The smallest radius of curvature ATFilms was willing to coat was 25 mm. The mirrors are 7.75 mm in diameter, and 4 mm thick when they were coated. After the optical coating, they were coned down to a 2 mm diameter reflective surface, and 4 mm in the outer diameter. We requested the mirrors to be coned so that metallic sheaths can be placed on them to provide shielding and compensation of stray fields in the cavity direction. Test cavities were first made from the mirrors in order to estimate the losses of the mirrors [141], which resulted in estimates confirming the cavity transmissions and losses to an order of magnitude.

With these mirrors, the cavity length was initially chosen to be $400\ \mu\text{m}$ (which corresponds to a free spectral range of $\nu_{fsr} \approx 375\ \text{GHz}$). At this spacing, the relevant cavity QED parameters would have been $(g, \kappa, \gamma)/2\pi = (13.6, 44.7, 19.6)\text{MHz}$. These parameters give us a saturation photon number $n_{sat} = 0.26$ and a cooperativity of $C = 0.21$. From the simple calculation given for an initially excited ion, the collection probability is $p_c = \frac{T_2}{\mathcal{L}} \frac{2\kappa}{2\kappa + \gamma} \frac{2C}{1 + 2C} = 0.11$ (equation 3.50). This is the probability that an initially excited emits a photon into the cavity mode and it exits the cavity.

5.5.1 Characterization of the cavity The ion trap never loaded at the spacing of $400\ \mu\text{m}$, as both the ion trap and the piezo failed. The gold on the trap seemed to have evaporated off, leaving small balls of gold on the RF tine. Additionally, we were unable to couple light into the cavity with the coupling setup used earlier.

The second attempt was a more conservative cavity separation of approximately $2\ \text{mm}$, as we were worried about charging effects of the mirror. The coherent coupling rate would drop to $g/2\pi \approx 4\ \text{MHz}$. The simulations of the single photon source indicated that the cavity ought to produce single photons in the cavity at a reasonable rate for this separation (see Chapter III).

The piezo has mechanical resonances that appear on the electrical impedance of the piezo, Z_{pzt} . Measurement of the piezo impedance versus frequency would allow us to characterize the piezo to observe if there are any effects from baking the chamber.

To measure the impedance of the piezo before and after the bake we probed the voltage across the piezo in a voltage divider configuration. This measurement provides the transfer function of the voltage divider H_{div} , where we could extract the impedance of the piezo:

$$H_{div} = \frac{Z_{pzt}}{R + Z_{pzt}} \implies Z_{pzt} = \frac{RH}{1 - H}, \quad (5.1)$$

When we performed this measurement on the failed piezo, no resonances were ob-

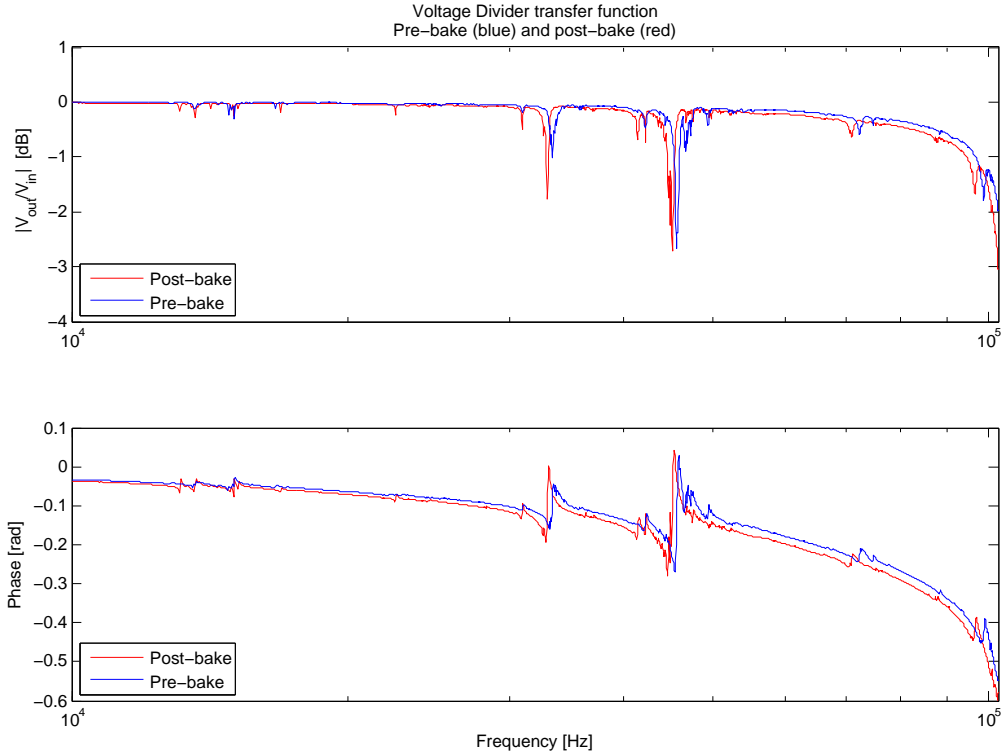


Figure 5.5: Measured transfer function of the piezo in a voltage divider configuration. Plotted is both the pre-bake transfer function (blue) and the post-bake at 110° (red). There are no significant changes in the response

served. Figure 5.5 is a Bode plot of the voltage divider transfer function before and after the bake. Clear mechanical resonances can be seen. From the transfer function, the magnitude of the piezo impedance is plotted in figure 5.6. From the 110°C bake, there was no significant change in the piezo response.

Once under vacuum, the cavity parameters were measured. At a cavity spacing of 2 mm, the free spectral range should be ≈ 75 GHz, which can be scanned across with a diode laser. In order to measure the actual value, zero bias was applied to the piezo and the 739 nm laser was tuned to find a resonance. Then the laser was tuned to the next adjacent resonance. We estimate based upon this method the free spectral range to be 70.5 GHz, corresponding to a cavity length of 2.126 mm.

The full width at half-maximum was measured by putting two frequencies into

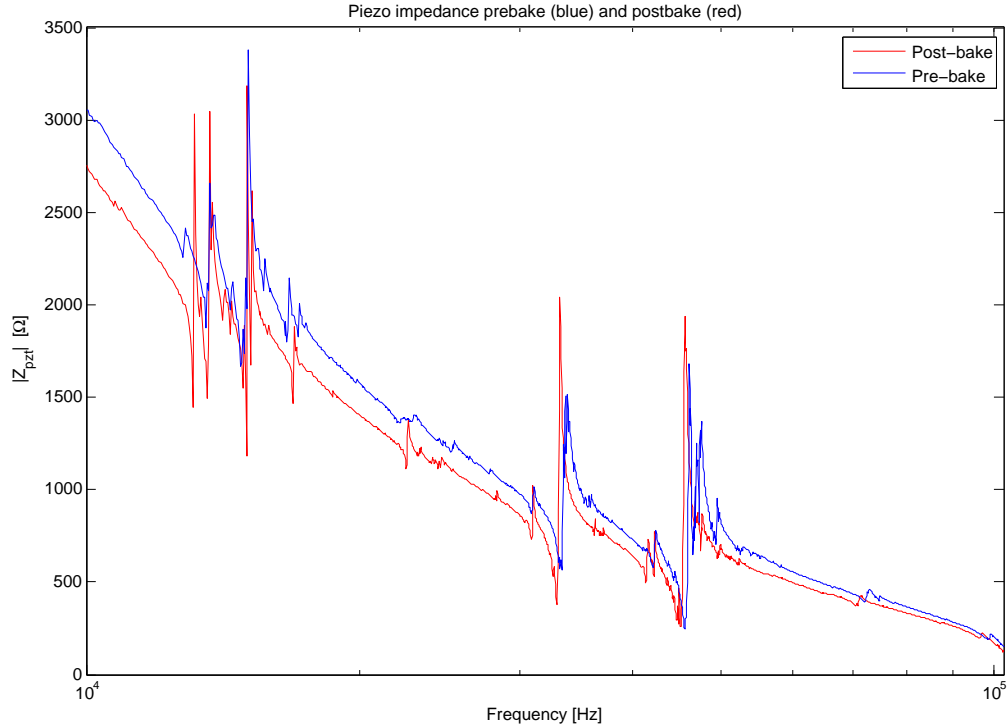


Figure 5.6: Magnitude of the piezo impedance versus frequency. Plotted is both before the bake (blue), and after the 110° bake.

the cavity and scanning across the resonance. At 739 nm, the current of the diode laser was modulated with a bias-T at 29 MHz. Figure 5.7a shows the transmission of the cavity as the cavity scans across resonance. The sideband serves as a frequency marker to which the full-width was measured to be 5.6 MHz, giving a finesse of $\mathfrak{F}_{739} = 12.600$. The same procedure was performed with UV light. The frequency marker in this case was a 100 MHz frequency shift from an acousto-optic modulator (the 0th and 1st orders were coupled into the cavity). The full width at half-maximum was measured to be 18.7 MHz, corresponding to a finesse of $\mathfrak{F}_{369} = 3790$. This measurement agrees with the final values given to us by ATFilms, and has a outcoupler efficiency of $T_2/\mathcal{L} \approx 60\%$.

5.5.2 Cavity coupling optics and locking The setup to couple light into the cavity is illustrated in Figure 5.8a. Both the infrared at 739 nm and ultraviolet at 369 nm

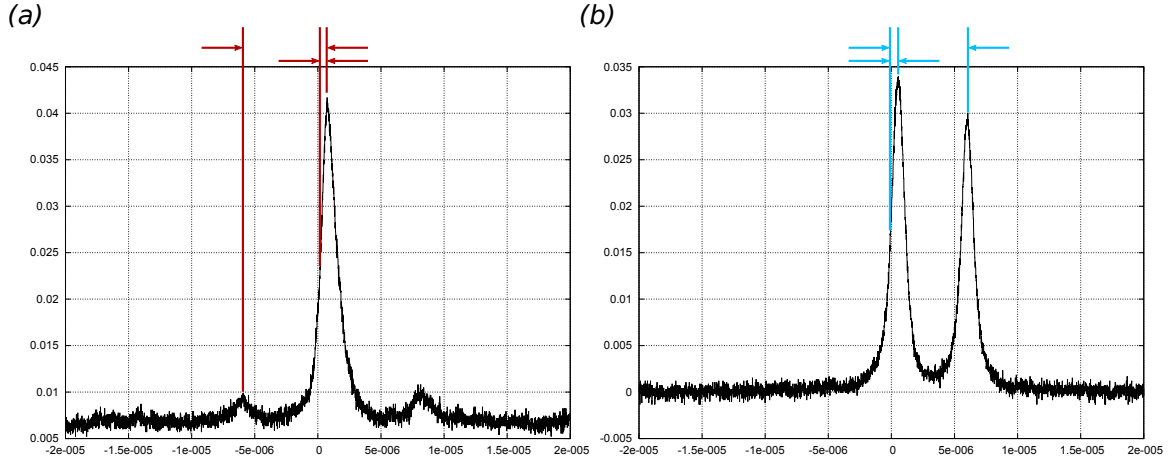


Figure 5.7: Transmission of the cavity with two similar laser frequencies to measure the full width at half-max. The lines indicate the distance to the frequency markers and the half-width. **(a)** Cavity transmission of the 739 nm with bias-T sidebands. **(b)** 369 nm cavity transmission with the 0th and 1st orders of an AOM coupled into the cavity

are coupled into the cavity. A 369 nm mirror acts as a dichroic and allows the two beams to be combined. Since the infrared light is used to lock the cavity and the ultraviolet is a weak probe, the mode matching optics were optimized for the infrared. Further upstream before combining the beams are the mode matching optics for the ultraviolet.

Approximately 200 μW of 739 nm light is sent to the cavity for locking. The spatial mode of the beam is cleaned by fiber coupling the light. The fiber has an electro-optic phase modulator, allowing the cavity length to be tuned with respect to the atom without changing the laser frequency.

We noticed that when scanning the cavity and observing both the ultraviolet and infrared independently, the cavity peaks were not overlapped even though the UV was exactly twice the frequency of the infrared. Applying a 2.323 GHz modulation on the red light with the fiber EOM aligned the peaks. This corresponds to a cavity length difference between the ultraviolet and infrared of ≈ 20 nm and can be accounted for by the manner in which the coatings were placed on the mirrors.

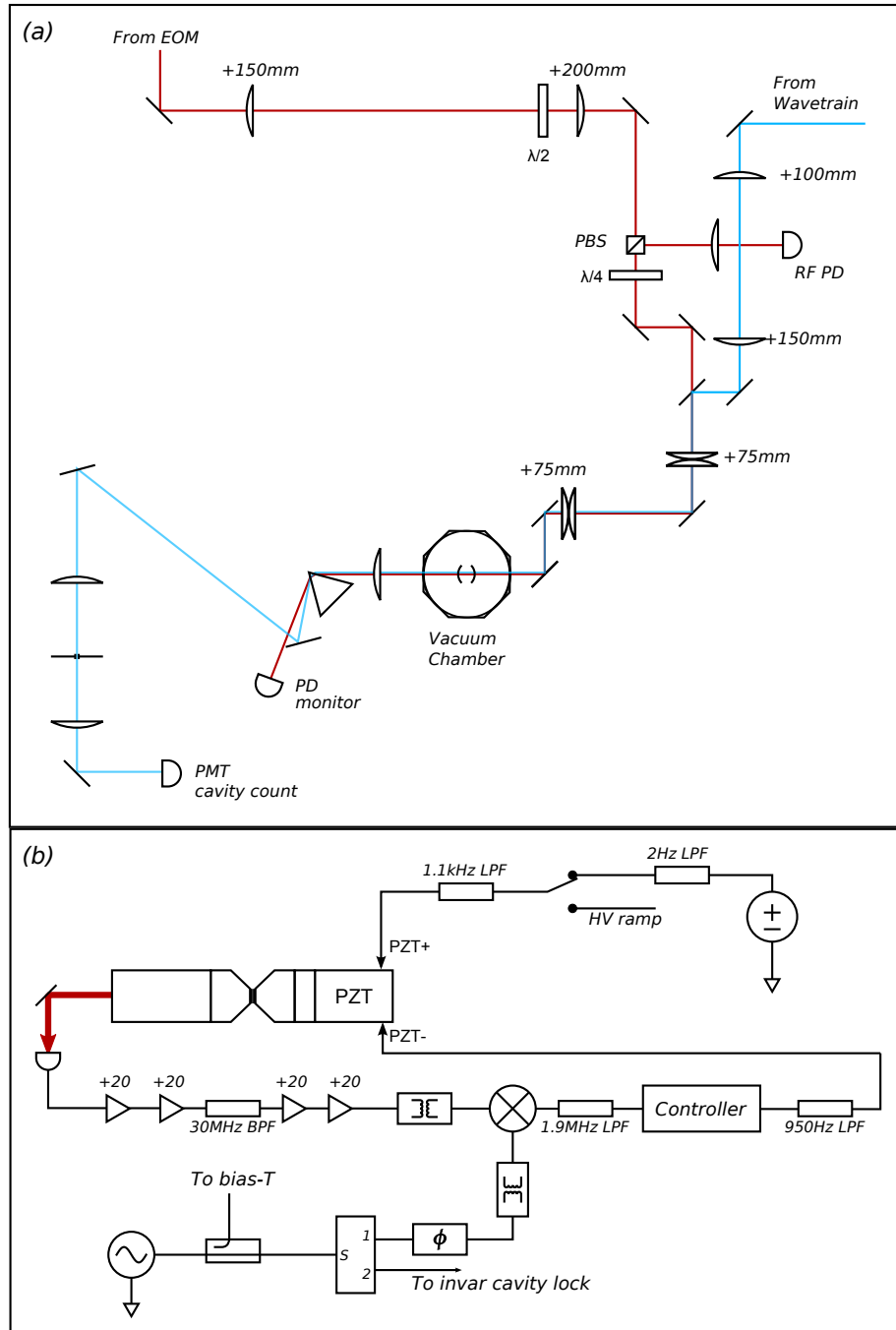


Figure 5.8: **(a)** Cavity coupling optics for both the UV and infrared light. On the output side of the chamber is the detection scheme. After collimation, there is a Brewster prisms to separate the UV from the infrared. The infrared is monitored on a photodiode while the UV is spatially filtered and detected on a PMT. **(b)** Electronic layout of the locking scheme. The fast photodiode outputs a very small signal and needs 80 dB of gain. To cut down on the noise in the signal there are a myriad of filters. To keep the noise on the lock low, we apply the control signal to the negative side of the piezo with a static HV offset on the positive side.

The error signal to lock the cavity is derived from the reflection of the 739 nm beam off the cavity (figure 5.8). The sidebands for the Pound–Drever–Hall locking scheme are derived from the bias-T modulation used for locking the laser to the passive Invar cavity. The RF photodiode is a Menlo Systems FPD 510-FV. The signal is sent through four MiniCircuits low-noise amplifiers (MiniCircuits ZFL-500HLN) which results in a 100 mV error signal. Between the second and third amplifier, there is a 30 MHz band-pass filter. This signal is then routed through a balancer (FTB-1-1) and then mixed with the local oscillator. On the local oscillator is a voltage controlled phase shifter (Pulsar SO-02-411), allowing us to maximize the error signal for both the Invar cavity and the ion-cavity. The IF port of the mixer is sent through a 1.9 MHz low pass filter and input onto a Precision Photonics servo controller (LB1005). The output of the controller is sent through a home-built 950 Hz low pass filter and applied to the negative side of the piezo. The positive side of the piezo has a static high voltage offset that is used to find the proper resonance of the cavity. The high voltage is derived from a DC power supply and is filtered by a home-built 2 Hz low pass filter. The DC output of the servo controller is monitored and the high voltage is offset accordingly to keep the DC output near zero. This allows us to correct for drifts in the cavity length due to temperature fluctuation while loading.

5.6 Ion Cavity Experiment

With the cavity separation of 2 mm, we reliably loaded $^{174}\text{Yb}^+$ ions in the trap. However, after running the trap for several weeks, we found a degradation in the finesse of the cavity. We measured the cavity linewidth by locking the cavity and tuning the cavity length with the fiber EOM. Using an ultraviolet probe beam in the

	$L = 400 \mu\text{m}$ $\mathfrak{F} = 1469$	$L = 400 \mu\text{m}$ $\mathfrak{F} = 3790$	$L = 2126 \mu\text{m}$ $\mathfrak{F} = 1469$	$L = 2126 \mu\text{m}$ $\mathfrak{F} = 3790$
$g/2\pi$	13.61 MHz	13.61 MHz	3.92 MHz	3.92 MHz
$\kappa/2\pi$	127.6 MHz	49.4 MHz	24 MHz	9.3 MHz
$\gamma/2\pi$	19.6 MHz	19.6 MHz	19.6 MHz	19.6 MHz
n_{sat}	0.26	0.26	3.12	3.12
C	0.074	0.19	0.0327	0.0844
$2C/(1 + 2C)$	0.129	0.277	0.061	0.144
T_2/\mathcal{L}	0.234	0.603	0.234	0.603

Table 5.2: Cavity QED parameters for the initial finesse and degraded finesse.

cavity, we were able to measure a lineshape. The full width at half-maximum had increased to 48 MHz. Measuring the output irradiance of UV beam on resonance is consistent with only an increase of absorption/scattering losses. From what we could determine, the transmissions had not changed.

Table 5.2 lists the various cavity QED parameters for the initial finesse as well as the degraded finesse. For comparison, the parameters at a 400 μm cavity are also listed. The simulations performed in Chapter III used the degraded finesse. The probability for collecting a single photon using the entanglement protocol with the degraded finesse is $\approx 4\%$, indicating an improvement of the collection efficiency over free space.

This section details our efforts to observe enhancement of fluorescence into the cavity mode with a single trapped $^{174}\text{Yb}^+$ ion. We observe a cavity count rate of 2200 s^{-1} .

5.6.1 Placement of the ion in the mode Prior to loading the trap and looking for enhancement of fluorescence, the ion must be placed at an anti-node of the cavity. To accomplish this, the cavity is scanned while the trap is moved. The ion trap is first moved across the mirror face such that we can ensure that the cavity mode will be cut-off by the substrate finger. Move the trap vertically until it starts cutting off the mode. At this point, we know that the ion trap is partially in the mode. The

ion trap is then slowly retracted while the cavity transmission is monitored. When the tip of the trap exits the cavity mode, the transmission increases. In this manner, the trap can roughly locate the cavity mode.

Next, the ion is loaded, and the cavity is locked. The ultraviolet probe beam for the cavity is unblocked and fluorescence of the ion is observed out the side of the cavity. By adjusting the ion position mechanically with the trap, the ion can be saturated with 5 μW of ultraviolet light.

The final method of improvement of ion-cavity coupling is an iterative process where the fluorescence out the cavity is monitored and peaked-up.

5.6.2 Output detection With the cavity locked, both ultraviolet light from the ion or cavity probe as well as infrared light exit the cavity. After an initial collimating lens, the output of the cavity is sent through a prism to separate the colors (figure 5.8a). The red light is sent onto a photodiode to monitor the cavity transmission. The ultraviolet beam is directed onto a flip mirror (not shown in figure). With the mirror down, the ultraviolet light is spatially filtered and directed onto a Hamamatsu PMT (H8259-01). The overall efficiency of our detection system (including detector quantum efficiency) is 10%.

With the flip mirror up, the light is directed onto a photodiode to monitor the transmission. This is primarily used to ensure the cavity is locked to a transmission peak that is resonant with the ultraviolet light.

5.6.3 Observation of fluorescence out the cavity A $^{174}\text{Yb}^+$ ion is subsequently loaded and the cavity is locked to near-resonance with the ion. Throughout our detection window of 20 ms, we measure both a signal and background scattered light. The first half of the detection window (10 ms) detects the raw count rate of the ion plus the background light. The next 10 ms, we turn off the AOM in our 935 nm beam path.

Without the repump light, the ion quickly goes dark. The 52.7 ms lifetime of the $^2D_{3/2}$ state ensures that we will rarely have ion fluorescence during the background measurement.

The PMT signal is switched between the two counters for the signal and the background, and is triggered slightly after the AOM is turned off and slightly before the AOM is turned back on.

Between each detection window, there is a 50 ms Doppler cooling stage. This ensures the ion is cool if it had heated up during our background measurement.

For the ion-cavity system, there are three relevant frequencies: the atomic resonance ν_0 , the laser pump frequency ν_p , and the cavity frequency ν_c . We are able to control the infrared laser frequency ν_L by adjustment of our laser frequency lock. Since $\nu_p = 2\nu_L + f_{AOM}$, we are able to control the pump frequency. Additionally, the cavity is locked to $\nu_c = 2\nu_L + 2(f_E - f_{E0})$, where f_E is the frequency of the cavity lock fiber EOM and f_{E0} is the frequency offset to have the ultraviolet probe resonant. The relevant detunings are

$$\delta_0/2\pi = \nu_0 - \nu_p = \nu_0 - 2\nu_L - f_{AOM} \quad (5.2)$$

$$\delta_{0c}/2\pi = \nu_0 - \nu_c = \nu_0 - 2\nu_L - 2(f_E - f_{E0}) \quad (5.3)$$

$$\delta_c/2\pi = \nu_c - \nu_p = 2(f_E - f_{E0}) - f_{AOM} \quad (5.4)$$

where δ_0 and δ_c are the detunings present in equation 3.51.

Our initial attempt at observing fluorescence from the ion resulted in tens of counts per second. By adjusting the position of the ion with respect to the mode while looking at this signal, we were able to improve the count rate to 1000 sec^{-1} . Figure 5.9 shows a resolved ion fluorescence rate above the background. The laser was detuned from resonance by 40 MHz, and the power was close to saturation. On

figure 5.9a, each point is a successive run of 10 detection windows. The plotted point is the average number of counts amongst those 10 windows. None of the parameters were changed in this first attempt. Taking this raw data, figure 5.9b is a histogram of the counts for every experiment.

An observed count rate of 1000 counts per second corresponds to an enhancement of 60 over the free-space scatter rate into the cavity solid angle. We estimate based upon a Purcell enhancement our coherent coupling rate, g , to be off its maximal value by an order of magnitude. The main limitation was the large amount of excess micromotion of the ion that could not be minimized.

The solution to the micromotion compensation was to change to a monofilar helical resonator with a lower resonance frequency. With this modification, we were able to minimize micromotion along the pumping beam from the side of the cavity. Figure 5.10 is a measurement of the fluorescence versus cavity length. The laser was set to slightly above saturation and held at a constant detuning of 15 MHz from the atomic resonance. The cavity length was scanned with the fiber EOM across the atomic resonance. We observe a full width of 55 MHz. The count rate we observe at resonance is 2200 counts per second. Since micromotion was not fully minimized along the cavity direction, the count rate is not as high and there is a broadening of the lineshape.

The data are indicative of modulation of the fluorescence and thus a sum of Lorentzians is fit to the lineshape. Each Lorentzian is offset by a frequency $\pm n f_{sb}$. The linewidth of the underlying Lorentzian is 53 MHz, and the shoulders are at 110 MHz. The data is consistent with amplitude modulation of the pump beam at 110 MHz, which is the resonant frequency of the acousto-optic modulator in the pump beam path. Nevertheless, the enhancement has increased to 130. With further

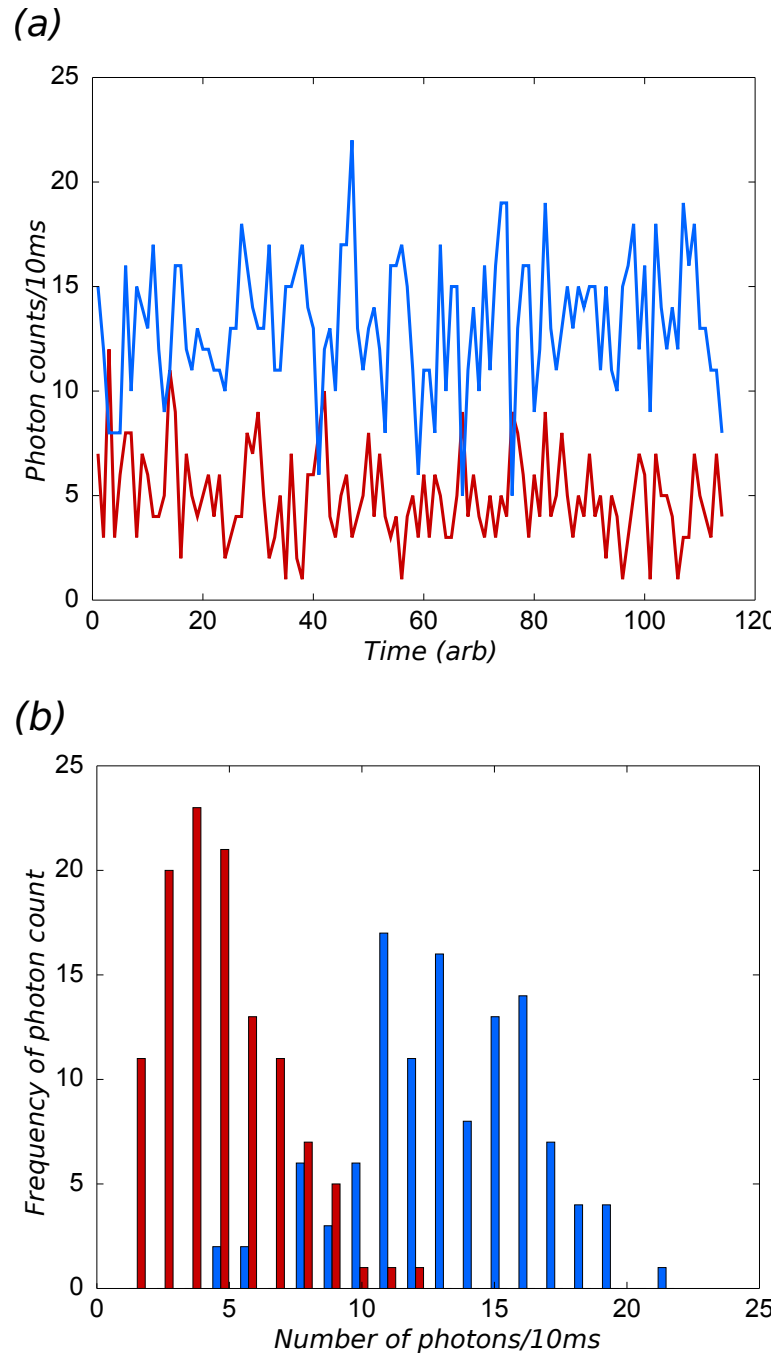


Figure 5.9: Initial observation of ion fluorescence from a cavity. **(a)** Time series of average number of counts per detection window. Each point in the series is an average of 5 experiments. **(b)** A histogram of the count rates for the signal and background illustrate a resolved number of counts.

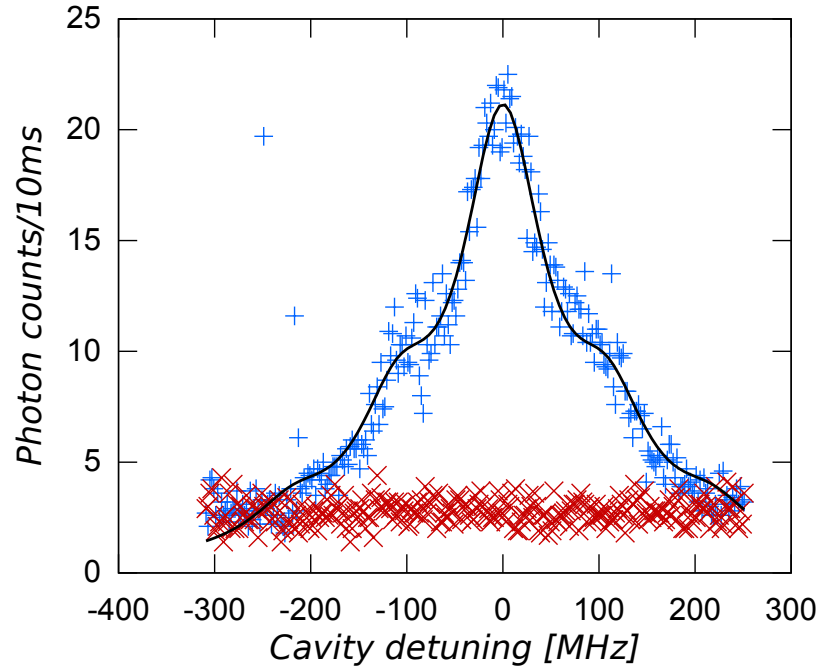


Figure 5.10: We measure a lineshape of the fluorescence versus cavity detuning. Resonance is at a cavity offset of 2255 MHz. Since micromotion wasn't completely minimized along the cavity axis the lineshape is broader and not as bright.

minimization of micromotion and a cleaner pump beam, we expect the enhancement to increase and the line shape to narrow.

Figure 5.10 indicates an enhancement of photon scatter into the cavity solid angle, demonstrating that improved collection of photons from single trapped ions. Our observation of an enhancement of 130 is not the fundamental limit, and can be improved with positioning and micromotion minimization. Smaller cavities with higher finesses can further the efficiency of light collection.

CHAPTER VI

Outlook and Conclusions

The observation of enhanced light collection from a single $^{174}\text{Yb}^+$ ion is the starting point for practical quantum networks. Although the absolute count rate of photons is much smaller than what can be achieved with a microscope objective, we are currently observing an enhancement over the free space scatter rate into the solid angle subtended by the cavity mode. There are two limitations to the current enhancement: the outcoupling efficiency and the mode volume.

The outcoupling efficiency, given by T_2/\mathcal{L} , is the fraction of light that is scattered in the cavity mode that exits the cavity towards the detector. With the initial measured cavity finesse and the transmission of the outcoupling mirror, this efficiency would be approximately 60%. However, since the cavity finesse has degraded this efficiency is now 20%. Higher quality ultraviolet coatings where the absorptive and scattering losses are negligible would be highly desirable.

From the simple Purcell model described in Chapter refchap:model, the enhancement of scattering into the cavity is given by the cooperativity, C . Equation 3.37 shows that the cooperativity is inversely proportional to the cavity losses and the mode area. Smaller mode volume cavities can create larger scatter rates into the cavity mode. With a 400 μm cavity separation, the cavity QED parameters are

$(g, \kappa, \gamma)/2\pi = (13.6, 125.9, 19.6)\text{MHz}$, which gives $(C, n_{\text{sat}}) = (0.074, 0.26)$. The coöperativity increases by a factor of two. The large cavity linewidth is primarily dominated by the absorption and scattering losses.

In principle, these are technological limitations. Lower loss mirrors, smaller radius of curvature mirrors, and shorter cavities will increase the collection efficiency.

So far we have only observed the fluorescence of a single trapped ion through a cavity. The next step would be to generate single photons and polarization entanglement with the protocol described in Chapter III and compare the success probabilities for generating atom–photon entanglement, P_{ap} .

6.0.4 Integrated Quantum Photonics One future direction would be the use of integrated optics with microfabricated ion traps [142]. Such possible schemes could include the use of microfabricated mirrors [65] or fiber based Fabry–Perot cavities [143, 144]. Microfabricated mirrors are attractive as the ion can be lithographically defined to be placed at the focus of the mirror. Multi-scale optics can be used for imaging large arrays of ions with high detection fidelity [65].

The combination of a microfabricated mirror and a fiber tip or a fiber Fabry–Pérot cavity could give rise to single atom coöperativities $C \sim 100$ [142]. This could allow for deterministic generation of entangled photons [69].

6.0.5 Entanglement of Hybrid Systems Another possible scheme is to build an optical cavity for 935 nm light and generate single infrared photons entangled with the $^2D_{3/2}$ level of $^{171}\text{Yb}^+$. Such entanglement schemes could be used for a loophole free Bell-inequality measurement [], or to entangle an ion with a quantum dot [145].

6.0.6 Practical Quantum Networks With larger collection efficiencies it becomes feasible to create large scale quantum networks. Modest improvements to the collection efficiency scale quadratically. Currently the success probability is 2.2×10^{-8} and the

experiment is run at 70 k/sec [34]. This results in a successful entanglement every 12 sec. If the collection efficiency were to be improved by an order of magnitude and have 50% fiber coupling due to the Gaussian output of the cavity, the entanglement generation rate could be 1 s^{-1} . At this point, the entanglement generation rate is faster than the coherence time of the qubits allowing the generation of multiple qubit entangled pairs.

With an entanglement rate faster than the coherence time of the qubit, connection of arbitrary nodes in a quantum network can be realized and quantum information can be shared across the network. Trapped ion quantum processors at each node can perform distributed quantum computation—a sort of quantum internet [82]. To send information across long distances quantum repeaters can be generated. Finally, two-dimensional cluster states can be efficiently generated with these entanglement protocols [146, 147, 28].

APPENDICES

APPENDIX A

Simulation Code

This appendix catalogues the MATLAB code used to numerically solve the master equation. The code uses the Quantum Optics Toolbox for MATLAB [148].

The script `cavityCalc.m` is the first set of code run. It generates the values of γ , κ , g and the rest of the cavity QED parameters.

```
% Constants
c = 299792458;
nu0 = 2*405645750;
lambda = c/nu0;

% Define cavity parameters
fsr = 70.503e3;           % measured fsr
kappa = 2*pi*24;         % measured hwhm for uv
T = 1000e-6;             % estimated transmission

% More cavity parameters
L = c/(2*fsr);           % Cavity Length
roc = 25000;             % Radius of curvature
```

```

zR = (0.5)*sqrt(L*(2*roc - L)); % Rayleigh Range
w0 = sqrt(lambda*zR/pi);      % Mode waist
V = (pi/4)*L*w0^2;           % Mode volume
dOmega = 4*pi*(1-cos(w0/zR)); % Cavity solid angle

finesse = fsr/(kappa/pi);    % finesse
loss = 2*pi/finesse;        % Cavity Losses

eff = (T/loss)*(0.1);       % Output Efficiency

gamma = 1e3/8.12;          % gamma = gamma_parallel
g = sqrt(gamma*(3*pi*c^3)/(2*V*(2*pi*nu0)^2));

N = 30;                    % Number of photon excitations in system

% Radiatively broadened
gammaperp = gamma/2;
gammapar = gamma;

% Saturation photon number and cooperativity
nsat = (gammaperp*gammapar)/(4*g^2);
C = g^2/(2*kappa*gammaperp);

```

The script `resonantTLS` calculates the steady-state photon scatter rate out both the cavity and the side for the case where the pump is resonant with both the cavity and the atom ($\omega_c = \omega_0 = \omega_p$). It numerically solves the master equation as well as the semiclassical approach. The script steps through various pump strengths $s = I/I_{sat}$.

```

cavityCalc;      % Setup cavity parameters

% Detunings
da = 2*pi*0;      % Atom
dc = 2*pi*0;      % Cavity

% Drive
smax = 5;
s = 0:.01:smax;
nloop = length(s);

yy = sqrt(s);
drive = sqrt(gamma_perp*gamma_par)*yy/2;

cavitycount = zeros(nloop,1);
sidecount = zeros(nloop,1);

xx = zeros(3,nloop);

% Set up the Quantum Operators
ida = identity(N);
idatom = identity(2);
a = tensor(destroy(N),idatom);
sm = tensor(ida,sigmam);
Cp = sqrt(2*kappa)*a;      %Cavity collapse
Ca = sqrt(gam)*sm;        %Side collapse

% Dissipator
dis = @(X) spre(X)*spost(X') - 0.5*spre(X'*X) -0.5*spost(X'*X);

```

```

for k = 1:nloop

    %Hamiltonian and Liouvillian

    H = deltaC*a'*a + deltaA*sm'*sm + ...
        i*g*(a'*sm-a*sm') + drive(k)*(sm'+sm);
    L = -i*(spre(H) - spost(H)) + dis(Cp) + dis(Ca);

    %Steady state solution

    rhoss = steady(L);

    % Count rates

    cavitycount(k) = expect(Cp'*Cp,rhoss);
    sidecount(k) = expect(Ca'*Ca,rhoss);

    %Solve the analytic bistability equations

    pp = [1 2*yy(k) (yy(k)^2+1+2*C) 2*C*yy(k)];
    xx(:,k) = roots(pp);

end

    %Now determine the solution from bistability equation.

    rr = find(imag(xx)==0);
    cfield = xx(rr);
    cout = 2*kappa*nsat*(cfield.^2);

    % Normal photon scatter rate

    Gsc = (gamma*(1+2*C)/2)*(s./(1+s + 4*(da/(gamma*(1+2*C)))^2));
    Gsc2 = (gamma/2)*(s./(1+s + 4*(da/gamma)^2));

```

```

cavityOutMeas = eff*real(cavitycount)*1e6;
semiOutMeas = eff*cout*1e6;
scattOutMeas = eff*Gsc*2*C*1e6;
scattOutMeas2 = eff*Gsc2*2*C*1e6;

```

Likewise, the script `saturationTLS` numerically solves the master equation for both the steady-state photon count rate out the cavity as a function of the detuning of the cavity from the atomic resonance $\omega_0 - \omega_c$. Additionally, the spectrum of fluorescence out the side of the cavity is calculated for zero detuning. The intensity of the pump light is held constant.

```

% First generate the cavity parameters
cavityCalc;

% Detunings
delta = 2*pi*(-200:1:200);      % omega_atom - omega_cavity
deltaA = 2*pi*0;                % omega_atom - omega_pump
deltaC = deltaA - delta;        % omega_cavity - omega_pump

nloop = length(delta);         % Number of loops

% Drive
s = 35;                          % Saturation parameter I/Isat
drive = (0.5)*gamma*sqrt(0.5*s); % Rabi frequency

% Define Output variables
cavitycount = zeros(nloop,1);
sidecount = zeros(nloop,1);

```

```

% Operators
ida = identity(N); idatom = identity(2);
a = tensor(destroy(N), idatom);
sm = tensor(ida, sigmam);

Cp = sqrt(2*kappa)*a;
Ca = sqrt(gamma)*sm;

% Dissipator
dis = @(X) spre(X)*spost(X') - 0.5*spre(X'*X) -0.5*spost(X'*X);

% Generate the steady state photon count rate versus detuning
for k = 1:nloop

    %Hamiltonian
    H = deltaC(k)*a'*a + deltaA*sm'*sm + i*g*(a'*sm - a*sm') + ...
        drive*(sm' + sm);

    % Liouvillian
    L = -i*(spre(H) - spost(H)) + dis(Cp) + dis(Ca);

    % Steady state
    rhoss = steady(L);

    % Steady-state photon counts
    cavitycount(k) = expect(Cp'*Cp, rhoss);
    sidecount(k) = expect(Ca'*Ca, rhoss);
end

```

```

% Measured count rate
cavityOutMeas = eff*real(cavitycount)*1e6;

% Let's look at the spectrum of emitted photons when cavity is resonant
H = deltaA*sm'*sm + i*g*a'*sm - i*g*a*sm' + drive*(sm' + sm);
L = -i*(spre(H) - spost(H)) + dis(Cp) + dis(Ca);

% Steady state
rhoss = steady(L);
smss = expect(sm,rhoss);

smrho = sm*rhoss; % Initial condition for regression theorem

% Solve differential equation with this initial condition
solESs = ode2es(L,smrho);

% Find trace(a' * solution)
corrESs = expect(sm',solESs);

% Calculate the covariance by subtracting product of means
covESs = corrESs - smss'*smss;

PSD = esspec(covESs,delta);

```

Finally, the probability of collecting single photons using $^{171}\text{Yb}^+$ is computed in the function `photonemission2`. The script outputs the probability density function for a photon to be emitted out the cavity in the interval $[t, t + dt)$ as well as the integrated density. Additionally, it outputs the same information for a photon being

emitted out the side of the cavity.

```
function [count, Pe, tlist, scount, Ps] = ...
    photonemission2(drive, kappa, gamma, g, N, delta)
% This function determines the total probability of emitting a photon
% out of a cavity. The system under consideration is that of a three-
% level atom coupled to a single mode cavity. The atom is driven from
%  $g \rightarrow a$  by a semiclassical beam of strength  $\Omega$ . This auxilliary
% state is coupled at a rate  $g$  to a cavity mode, taking it from  $a \rightarrow e$ ,
% an excited ground state. The cavity decays at a rate  $kappa$ , and the
% auxillary state decays at a rate  $gamma$  to each of the two ground
% states.

% Identity operators
iatom = identity(4);
iphot = identity(N);

% I can't think of an easier/ more clever way of generating all
% possible pairs of  $|i\rangle\langle j|$ 
v = basis(4, 1:4);
for iy = 1:4
    for jy = 1:4
        A{iy, jy} = tensor(v{iy}* (v{jy})', iphot, iphot);
    end
end

% Photon annihilation operator
a = tensor( iatom, destroy(N), iphot);
b = tensor( iatom, iphot, destroy(N));
```

```

% Hamiltonian
H = delta*A{2,2} + drive*(A{2,1}+A{1,2}) + i*g*(a'*A{3,2}-a*A{2,3}) - ...
    i*g*(b'*A{4,2}-b*A{2,4});

% Dissipator
dis = @(x) spre(x)*spost(x') - 0.5*spre(x'*x) - 0.5*spost(x'*x);

% Liouvillian:
L = -i*(spre(H) - spost(H)) + dis(sqrt(2*kappa)*a) + ...
    dis(sqrt(gamma)*A{1,2}) + dis(sqrt(gamma)*A{3,2}) + ...
    dis(sqrt(gamma)*A{4,2}) + dis(sqrt(2*kappa)*b);

%rhoss = steady(L);

% Initial state:
psi0 = tensor(v{1},basis(N,1),basis(N,1));
rho0 = psi0*psi0';

% Time series of rho(t)
rhoES = ode2es(L,rho0);

% Photon count rate
tlist = linspace(0,10/gamma,500);
count = 2*kappa*esval(expect(a'*a,rhoES),tlist) + ...
    2*kappa*esval(expect(b'*b,rhoES),tlist);
count = real(count);

% Side counts
scount = 2*gamma*real(esval(expect(A{2,2},rhoES),tlist));

```

```
% Integrate the density function
Pe(1) = 0;
Ps(1) = 0;
for ey=2:length(tlist)
    Pe(ey) = trapz(tlist(1:ey),count(1:ey));
    Ps(ey) = trapz(tlist(1:ey),scount(1:ey));
end
```

BIBLIOGRAPHY

BIBLIOGRAPHY

- [1] T. D. Ladd et al., “Quantum computers”, *Nature* **464**, 45 (2010).
- [2] N. Gisin, G. Ribordy, W. Tittel, and H. Zbinden, “Quantum cryptography”, *Rev. Mod. Phys.* **74**, 145 (2002).
- [3] V. Giovannetti, S. Lloyd, and L. Maccone, “Quantum Metrology”, *Phys. Rev. Lett.* **96**, 010401 (2006).
- [4] P. Shor, “Algorithms for quantum computation: discrete logarithms and factoring”, in *Proc. 35th Ann. Sym. Found. Comp. Sci.*, page 124, 1994.
- [5] J. I. Cirac and P. Zoller, “Quantum Computation with Cold Trapped Ions”, *Phys. Rev. Lett.* **74**, 4091 (1995).
- [6] C. Monroe, D. M. Meekhof, B. E. King, W. M. Itano, and D. J. Wineland, “Demonstration of a Fundamental Quantum Logic Gate”, *Phys. Rev. Lett.* **75**, 4714 (1995).
- [7] I. H. Deutsch, G. K. Brennen, and P. S. Jessen, “Quantum Computing with Neutral Atoms in an Optical Lattice”, *Fortschritte der Physik* **48**, 925 (2000).
- [8] J. Porto, S. Rolston, B. Tolra, C. Williams, and W. Phillips, “Quantum information with neutral atoms as qubits”, *Philosophical Transactions of the Royal Society of London Series A-Mathematical Physical and Engineering Sciences* **361**, 1417 (2003).
- [9] D. Jaksch, “Optical lattices, ultracold atoms and quantum information processing”, *Contemporary Physics* **45**, 367 (2004).
- [10] Y. Makhlin, G. Schön, and A. Shnirman, “Quantum-state engineering with Josephson-junction devices”, *Rev. Mod. Phys.* **73**, 357 (2001).
- [11] M. H. Devoret, A. Wallraff, and J. M. Martinis, “Superconducting Qubits: A Short Review”, *ArXiv Condensed Matter e-prints* (2004).
- [12] R. Hanson, L. P. Kouwenhoven, J. R. Petta, S. Tarucha, and L. M. K. Vandersypen, “Spins in few-electron quantum dots”, *Rev. Mod. Phys.* **79**, 1217 (2007).
- [13] D. Press, T. D. Ladd, B. Zhang, and Y. Yamamoto, “Complete quantum control of a single quantum dot spin using ultrafast optical pulses”, *Nature* **456**, 218 (2008).
- [14] E. Knill, R. Laflamme, and G. J. Milburn, “A scheme for efficient quantum computation with linear optics”, *Nature* **409**, 46 (2001).
- [15] A. Gilchrist et al., “Schrödinger cats and their power for quantum information processing”, *Journal of Optics B: Quantum and Semiclassical Optics* **6**, 828 (2004).
- [16] D. P. Divincenzo, “The Physical Implementation of Quantum Computation”, *Fortschritte der Physik* **48**, 771 (2000).

- [17] S. Olmschenk et al., “Manipulation and Detection of a Trapped Yb^+ Ion Hyperfine Qubit”, *Physical Review A* (2007).
- [18] A. H. Myerson et al., “High-Fidelity Readout of Trapped-Ion Qubits”, *Phys. Rev. Lett.* **100**, 200502 (2008).
- [19] D. Kielpinski, C. Monroe, and D. J. Wineland, “Architecture for a large-scale ion-trap quantum computer”, *Nature* **417**, 709 (2002).
- [20] D. Stick et al., “Ion Trap in a Semiconductor Chip”, *Nature Physics* **2**, 36 (2006).
- [21] S. Seidelin et al., “A Microfabricated Surface-Electrode Ion Trap for Scalable Quantum Information Processing”, *Phys. Rev. Lett.* **96**, 253003 (2006).
- [22] J. Britton et al., “A microfabricated surface-electrode ion trap in silicon”, *ArXiv Quantum Physics e-prints* (2006).
- [23] D. R. Leibbrandt et al., “Demonstration of a scalable, multiplexed ion trap for quantum information processing”, *Quantum Information & Computation* **9**, 901 (2009).
- [24] D. Stick et al., “Demonstration of a microfabricated surface electrode ion trap”, *ArXiv e-prints* (2010).
- [25] W. K. Hensinger et al., “T-junction ion trap array for two-dimensional ion shuttling, storage, and manipulation”, *Applied Physics Letters* **88**, 034101 (2006).
- [26] D. Hucul et al., “On the transport of atomic ions in linear and multidimensional ion trap arrays”, *Quantum Information and Computation* **8**, 501 (2008).
- [27] R. B. Blakestad et al., “High-Fidelity Transport of Trapped-Ion Qubits through an X-Junction Trap Array”, *Physical Review Letters* **102**, 153002 (2009).
- [28] L.-M. Duan and C. Monroe, “Colloquium: Quantum networks with trapped ions”, *Rev. Mod. Phys.* **82**, 1209 (2010).
- [29] B. B. Blinov, D. L. Moehring, L. M. Duan, and C. Monroe, “Observation of entanglement between a single trapped atom and a single photon”, *Nature* **428**, 153 (2004).
- [30] P. Maunz et al., “Quantum interference of photon pairs from two remote trapped atomic ions”, *Nature Physics* **3**, 538 (2007).
- [31] D. L. Moehring, “Entanglement of single-atom quantum bits at a distance”, *Submitted* (2007).
- [32] D. N. Matsukevich, P. Maunz, D. L. Moehring, S. Olmschenk, and C. Monroe, “Bell Inequality Violation with Two Remote Atomic Qubits”, *Phys. Rev. Lett.* **100**, 150404 (2008).
- [33] S. Olmschenk et al., “Quantum Teleportation between Distant Matter Qubits”, *Science* **323**, 486 (2009).
- [34] P. Maunz et al., “A heralded quantum gate between remote quantum memories”, (2009), arXiv:quant-ph/0902.2136.
- [35] L. Luo et al., “Protocols and Techniques for a Scalable Atom–Photon Quantum Network”, *Fortschritte der Physik* **57**, 1133 (2009).
- [36] D. L. Moehring et al., “Quantum Networking with Photons and Trapped Atoms”, *J. Opt. Soc. Am. B* **24**, 300 (2007).
- [37] M. Acton et al., “Near-Perfect simultaneous measurement of a qubit register”, *Quantum Information and Computation* **6**, 465 (2006).

- [38] J. E. Sansonetti, W. C. Martin, and S. L. Young, *Handbook of Basic Atomic Spectroscopic Data*, Number 1.1.2, National Institute of Standards and Technology, Gaithersburg, MD, 2005, Available: <http://physics.nist.gov/Handbook>.
- [39] T. Kuwamoto, K. Honda, Y. Takahashi, and T. Yabuzaki, “Magneto-optical trapping of Yb atoms using an intercombination transition”, *Phys. Rev. A* **60**, R745 (1999).
- [40] C. J. Bowers et al., “Experimental investigation of excited-state lifetimes in atomic ytterbium”, *Phys. Rev. A* **53**, 3103 (1996).
- [41] M. Gustavsson, H. Lundberg, L. Nilsson, and S. Svanberg, “Lifetime measurements for excited states of rare-earth atoms using pulse modulation of a cw dye-laser beam”, *J. Opt. Soc. Am.* **69**, 984 (1979).
- [42] C. W. Hoyt et al., “Observation and Absolute Frequency Measurements of the 1S_0 - 3P_0 Optical Clock Transition in Neutral Ytterbium”, *Phys. Rev. Lett.* **95**, 083003 (2005).
- [43] P. Taylor et al., “Investigation of the $^2S_{1/2} - ^2D_{5/2}$ clock transition in a single ytterbium ion”, *Phys. Rev. A* **56**, 2699 (1997).
- [44] N. Yu and L. Maleki, “Lifetime measurements of the $4f^{14}5d$ metastable states in single ytterbium ions”, *Phys. Rev. A* **61**, 022507 (2000).
- [45] R. W. Berends, E. H. Pinnington, B. Guo, and Q. Ji, “Beam-laser lifetime measurements for four resonance levels of Yb II”, *Journal of Physics B* **26**, L701 (1993).
- [46] M. Roberts, P. Taylor, G. P. Barwood, W. R. C. Rowley, and P. Gill, “Observation of the $^2S_{1/2} - ^2F_{7/2}$ electric octupole transition in a single $^{171}\text{Yb}^+$ ion”, *Phys. Rev. A* **62**, 020501(R) (2000).
- [47] E. Biémont, J.-F. Dutrieu, I. Martin, and P. Quinet, “Lifetime calculations in Yb II”, *J. Phys. B: At. Mol. Opt. Phys.* **31**, 3321 (1998).
- [48] J. M. Raimond, M. Brune, and S. Haroche, “Manipulating quantum entanglement with atoms and photons in a cavity”, *Rev. Mod. Phys.* **73**, 565 (2001).
- [49] S. Gleyzes et al., “Quantum jumps of light recording the birth and death of a photon in a cavity”, *Nature* **446**, 297 (2007).
- [50] P. Domokos, J. M. Raimond, M. Brune, and S. Haroche, “Simple cavity-QED two-bit universal quantum logic gate: The principle and expected performances”, *Phys. Rev. A* **52**, 3554 (1995).
- [51] P. Grangier, G. Reymond, and N. Schlosser, “Implementations of Quantum Computing Using Cavity Quantum Electrodynamics Schemes”, *Fortschritte der Physik* **48**, 859 (2000).
- [52] L.-M. Duan and H. J. Kimble, “Scalable Photonic Quantum Computation through Cavity-Assisted Interactions”, *Phys. Rev. Lett.* **92**, 127902 (2004).
- [53] L.-M. Duan, “Scaling ion trap quantum computation through fast quantum gates”, *Phys. Rev. Lett.* **93**, 100502 (2004).
- [54] B. Yurke, S. L. McCall, and J. R. Klauder, “SU(2) and SU(1,1) interferometers”, *Phys. Rev. A* **33**, 4033 (1986).
- [55] S. J. van Enk, N. Lütkenhaus, and H. J. Kimble, “Experimental procedures for entanglement verification”, *Phys. Rev. A* **75**, 052318 (2007).
- [56] U. Eichmann et al., “Young’s interference experiment with light scattered from two atoms”, *Phys. Rev. Lett.* **70**, 2359 (1993).

- [57] W. M. Itano et al., “Complementarity and Young’s interference fringes from two atoms”, *Phys. Rev. A* **57**, 4176 (1998).
- [58] C. Cabrillo, J. I. Cirac, P. García-Fernández, and P. Zoller, “Creation of entangled states of distant atoms by interference”, *Phys. Rev. A* **59**, 1025 (1999).
- [59] S. L. Braunstein and A. Mann, “Measurement of the Bell operator and quantum teleportation”, *Phys. Rev. A* **51**, R1727 (1995).
- [60] L. Mandel, “Quantum effects in one-photon and two-photon interference”, *Rev. Mod. Phys.* **71**, S274 (1999).
- [61] C. K. Hong, Z. Y. Ou, and L. Mandel, “Measurement of Subpicosecond Time Intervals between Two Photons by Interference”, *Phys. Rev. Lett.* **59**, 2044 (1987).
- [62] Y. H. Shih and C. O. Alley, “New type of Einstein-Podolsky-Rosen-Bohm experiment using pairs of light quanta produced by optical parametric downconversion”, *Phys. Rev. Lett.* **61**, 2921 (1988).
- [63] G. Shu, M. R. Dietrich, N. Kurz, and B. B. Blinov, “Trapped ion imaging with a high numerical aperture spherical mirror”, *Journal of Physics B: Atomic, Molecular and Optical Physics* **42**, 154005 (2009).
- [64] G. Shu, N. Kurz, M. R. Dietrich, and B. B. Blinov, “Efficient fluorescence collection from trapped ions with an integrated spherical mirror”, *Phys. Rev. A* **81**, 042321 (2010).
- [65] R. Noek et al., “Multiscale optics for enhanced light collection from a point source”, *Opt. Lett.* **35**, 2460 (2010).
- [66] A. P. VanDevender, Y. Colombe, J. Amini, D. Leibfried, and D. J. Wineland, “Efficient Fiber Optic Detection of Trapped Ion Fluorescence”, *Phys. Rev. Lett.* **105**, 023001 (2010).
- [67] N. Lindlein et al., “A new 4π geometry optimized for focusing on an atom with a dipole-like radiation pattern”, *Laser Physics* **17**, 927 (2007), 10.1134/S1054660X07070055.
- [68] A. Kuhn, M. Hennrich, and G. Rempe, “Deterministic Single-Photon Source for Distributed Quantum Networking”, *Phys. Rev. Lett.* **89**, 067901 (2002).
- [69] J. McKeever et al., “Deterministic Generation of Single Photons from One Atom Trapped in a Cavity”, *Science* **303**, 1992 (2004).
- [70] M. Keller, B. Lange, K. Hayasaka, W. Lange, and H. Walter, “Continuous generation of single photons with controlled waveform in an ion-trap cavity system”, *Nature* **431**, 1075 (2004).
- [71] H. Walther, B. T. H. Varcoe, B.-G. Englert, and T. Becker, “Cavity quantum electrodynamics”, *Reports on Progress in Physics* **69**, 1325 (2006).
- [72] M. Hijlkema et al., “A single-photon server with just one atom”, *Nature Physics* **3**, 253 (2007).
- [73] H. G. Barros et al., “Deterministic single-photon source from a single ion”, *New Journal of Physics* **11**, 103004 (2009).
- [74] B. Sun, M. S. Chapman, and L. You, “Atom-photon entanglement generation and distribution”, *Phys. Rev. A* **69**, 042316 (2004).
- [75] D. L. Zhou, B. Sun, C. P. Sun, and L. You, “Generating entangled photon pairs from a cavity-QED system”, *Phys. Rev. A* **72**, 040302 (2005).

- [76] T. Wilk, S. C. Webster, A. Kuhn, and G. Rempe, “Single-atom single-photon quantum interface.”, *Science* **317**, 488 (2007).
- [77] B. Weber et al., “Photon-Photon Entanglement with a Single Trapped Atom”, *Phys. Rev. Lett.* **102**, 030501 (2009).
- [78] G. Guthohrlein, M. Keller, K. Hayasaka, W. Lange, and H. Walther, “A single ion as a nanoscopic probe of an optical field”, *NATURE* **414**, 49 (2001).
- [79] M. Keller, B. Lange, K. Hayasaka, W. Lange, and H. Walther, “Stable long-term coupling of a single ion to a cavity mode”, *Journal of Modern Optics* **54**, 1607 (2007).
- [80] A. B. Mundt et al., “Coupling a Single Atomic Quantum Bit to a High Finesse Optical Cavity”, *Physical Review Letters* **89**, 103001 (2002).
- [81] D. G. Norris, L. A. Orozco, P. Barberis-Blostein, and H. J. Carmichael, “Observation of Ground-State Quantum Beats in Atomic Spontaneous Emission”, *Phys. Rev. Lett.* **105**, 123602 (2010).
- [82] H. J. Kimble, “The quantum internet”, *Nature* **453**, 1023 (2008).
- [83] E. M. Purcell, “Spontaneous Emission Probabilities at Radio Frequencies”, *Physical Review* **69**, 681 (1946).
- [84] A. E. Siegman, *Lasers*, Stanford University Press, Stanford, 1986.
- [85] S. Ramo, J. R. Whinnery, and T. V. Duzer, *Fields and Waves in Communication Electronics*, Wiley, third edition, 1994.
- [86] D. Kleppner, “Inhibited Spontaneous Emission”, *Phys. Rev. Lett.* **47**, 233 (1981).
- [87] G. Gabrielse and H. Dehmelt, “Observation of inhibited spontaneous emission”, *Phys. Rev. Lett.* **55**, 67 (1985).
- [88] D. J. Heinzen, J. J. Childs, J. E. Thomas, and M. S. Feld, “Enhanced and Inhibited Visible Spontaneous Emission by Atoms in a Confocal Resonator”, *Physical Review Letters* **58**, 1320 (1987).
- [89] A. A. Houck et al., “Controlling the Spontaneous Emission of a Superconducting Transmon Qubit”, *Phys. Rev. Lett.* **101**, 080502 (2008).
- [90] Bloembergen and Pound, “Radiation Damping in Magnetic Resonance Experiments”, *Physical Review* **95**, 8 (1954).
- [91] E. A. Power, *Introductory Quantum Electrodynamics*, Elsevier, New York, 1965.
- [92] H. Morawitz, “Self-Coupling of a Two-Level System by a Mirror”, *Physical Review* **187**, 1792 (1969).
- [93] G. Barton, “Quantum Electrodynamics of Spinless Particles between Conducting Plates”, *Proceedings of the Royal Society of London. A. Mathematical and Physical Sciences* **320**, 251 (1970).
- [94] P. Stehle, “Atomic Radiation in a Cavity”, *Physical Review A* **2**, 102 (1970).
- [95] G. Feher, J. P. Gordon, E. Buehler, E. A. Gere, and C. D. Thurmond, “Spontaneous Emission of Radiation from an Electron Spin System”, *Phys. Rev.* **109**, 221 (1958).
- [96] K. H. Drexhage, H. Kuhn, and F. P. Schafer, “Variation of fluorescence decay time of a molecule in front of a mirror”, *Berichte der Bunsen-Gesellschaft für Physikalische Chemie* **72**, 329 (1968).

- [97] S. D. Brorson, H. Yokoyama, and E. P. Ippen, “Spontaneous Emission Rate Alteration in Optical Waveguide Structures”, *IEEE Journal of Quantum Electronics* **26**, 1492 (1990).
- [98] P. W. Milonni and P. L. Knight, “Spontaneous emission between mirrors”, *Optics Communications* **9**, 119 (1973).
- [99] J. P. Dowling, M. O. Scully, and F. Demartini, “Radiation pattern of a classical dipole in a cavity”, *Optics Communications* **82**, 415 (1991).
- [100] A. Einstein, “Zur Quantentheorie der Strahlung”, *Physik Z* **18**, 121 (1917).
- [101] V. S. Weisskopf and E. Wigner, “Berechnung der natürlichen linienbreite auf grund der Diracschen lichttheorie”, *Z. Physik* **63**, 54 (1930).
- [102] D. J. Heinzen and M. S. Feld, “Vacuum Radiative Level Shift and Spontaneous-Emission Linewidth of an Atom in an Optical Resonator”, *Physical Review Letters* **59**, 2623 (1987).
- [103] J. P. Woerdman, M. P. Van Exter, and N. J. Van Druten, *Quantum Noise of Small Lasers*, volume 47 of *Advances in Atomic, Molecular, and Optical Physics*, pages 205–248, Academic Press, 2001.
- [104] H. J. Carmichael, *Statistical Methods in Quantum Optics 2: Non-classical fields*, Springer, New York, 2008.
- [105] E. Jaynes and F. Cummings, “Comparison of Quantum and Semiclassical Radiation Theories with Application to the Beam Maser”, *Proceedings of the IEEE* **51**, 89 (1963).
- [106] L. Mandel and E. Wolf, *Optical Coherence and Quantum Optics*, Cambridge University Press, 1st edition, 1995.
- [107] L. Allen and J. H. Eberly, *Optical Resonance and Two-Level Atoms*, Wiley, New York, 1975.
- [108] H. J. Carmichael, *Statistical Methods in Quantum Optics 1: Master Equations and Fokker–Planck Equations*, Springer, New York, 1999.
- [109] P. R. Rice and H. J. Carmichael, “Single-Atom Cavity-Enhanced Absorption I: Photon Statistics in the Bad-Cavity Limit”, *IEEE Journal of Quantum Electronics* **24**, 1351 (1988).
- [110] P. Drummond, “Optical bistability in a radially varying mode”, *Quantum Electronics, IEEE Journal of* **17**, 301 (1981).
- [111] H. J. Kimble, “Strong Interactions of Single Atoms and Photons in Cavity QED”, *Physica Scripta* **T76**, 127 (1998).
- [112] R. J. Thompson, G. Rempe, and H. J. Kimble, “Observation of normal-mode splitting for an atom in an optical cavity”, *Phys. Rev. Lett.* **68**, 1132 (1992).
- [113] P. Maunz et al., “Normal-Mode Spectroscopy of a Single-Bound-Atom–Cavity System”, *Phys. Rev. Lett.* **94**, 033002 (2005).
- [114] J. Bochmann et al., “Fast Excitation and Photon Emission of a Single-Atom-Cavity System”, *Phys. Rev. Lett.* **101**, 223601 (2008).
- [115] L. A. Lugiato, “Theory of Optical Bistability”, *Progress in Optics* **21**, 69 (1984).
- [116] C. Law and H. Kimble, “Deterministic generation of a bit-stream of single-photon pulses”, *Journal of Modern Optics* **44**, 2067 (1997).
- [117] S. Earnshaw, “On the Nature of the Molecular Forces which Regulate the Consitution of the Luminiferous Ether”, *Transactions of the Cambridge Philosophical Society* **7**, 97 (1842).

- [118] M. A. Heald and J. B. Marion, *Classical Electromagnetic Radiation*, Saunders College Publishing, New York, 3rd edition, 1995.
- [119] W. Paul, “Electromagnetic traps for charged and neutral particles”, *Rev. Mod. Phys.* **62**, 531 (1990).
- [120] D. J. Wineland, R. E. Drullinger, and F. L. Walls, “Radiation Pressure Cooling of Bound Resonant Absorbers”, *Phys. Rev. Lett.* **40**, 1639 (1978).
- [121] W. Neuhauser, M. Hohenstatt, P. Toschek, and H. Dehmelt, “Optical-Sideband Cooling of Visible Atom Cloud Confined in Parabolic Well”, *Phys. Rev. Lett.* **41**, 233 (1978).
- [122] S. R. Jefferts, C. Monroe, E. Bell, and D. J. Wineland, “Coaxial-Resonator Driven rf (Paul) Trap for Strong Confinement”, *Phys. Rev. A* **51**, 3112 (1995).
- [123] P. T. H. Fisk, M. J. Sellars, M. A. Lawn, and C. Coles, “Accurate Measurement of the 12.6 GHz “Clock” Transition in Trapped $^{171}\text{Yb}^+$ Ions”, *IEEE Trans. Ultrasonics, Ferroelectrics, and Frequency Control* **44**, 344 (1997).
- [124] T. Rosenband et al., “Frequency ratio of Al^+ and Hg^+ single-ion optical clocks; Metrology at the 17th decimal place”, *Science* **319**, 1808 (2008).
- [125] R. E. March, “Quadrupole ion trap mass spectrometry: theory, simulation, recent developments and applications”, *Rapid Comm. in Mass Spect.* **12**, 1543 (1998).
- [126] R. Blatt and D. J. Wineland, “Entangled states of trapped atomic ions”, *Nature* **453**, 1008 (2008).
- [127] T. M. Fortier et al., “Precision atomic spectroscopy for improved limits on variation of the fine structure constant and local position invariance”, *Phys. Rev. Lett.* **98**, 070801 (2007).
- [128] J. D. Jackson, *Classical Electrodynamics*, Wiley, 3rd edition, 1998.
- [129] D. Hucul et al., “On the Transport of Atomic Ions in Linear and Multidimensional Ion Trap Arrays”, *Quantum Information and Computation* **8**, 501 (2008).
- [130] J. H. Wesenberg, “Ideal intersections for radio-frequency trap networks”, *Phys. Rev. A* **79**, 013416 (2009).
- [131] D. J. Berkeland, J. D. Miller, J. C. Bergquist, W. M. Itano, and D. J. Wineland, “Minimization of ion micromotion in a Paul trap”, *Journal of Applied Physics* **83**, 5025 (1998).
- [132] M. Abramowitz and I. A. Stegun, *Handbook of Mathematical Functions*, U.S. Gov’t. Printing Office, Washington, D.C., 1964.
- [133] D. Leibfried, R. Blatt, C. Monroe, and D. Wineland, “Quantum dynamics of single trapped ions”, *Rev. Mod. Phys.* **75**, 281 (2003).
- [134] H. G. Dehmelt, “Radiofrequency Spectroscopy of Stored Ions I: Storage”, *Adv. Atom. Mol. Phys.* **3**, 53 (1967).
- [135] L. Deslauriers et al., “Scaling and Suppression of Anomalous Heating in Ion Traps”, *Phys. Rev. Lett.* **97**, 103007 (2006).
- [136] M. Harlander, M. Brownnutt, W. Hänsel, and R. Blatt, “Trapped-ion probing of light-induced charging effects on dielectrics”, *New Journal of Physics* **12**, 093035 (2010).
- [137] V. Zaretsky, “private communication”.
- [138] W. W. Macalpine, “Coaxial resonators with helical inner conductor”, *Proceedings of the IRE* (1959).

- [139] A. Zverev and H. Blinichikoff, “Realization of a Filter with Helical Components”, *Component Parts, IRE Transactions on* **8**, 99 (1961).
- [140] S. Olmschenk, *Quantum Teleportation Between Distant Matter Qubits*, PhD thesis, University of Michigan, 2009.
- [141] C. J. Hood, H. J. Kimble, and J. Ye, “Characterization of high-finesse mirrors: Loss, phase shifts, and mode structure”, *Phys. Rev. A* **64**, 033804 (2001).
- [142] J. Kim and C. Kim, “Integrated Optical Approach to Trapped Ion Quantum Computation”, *Quantum Information and Computation* **9**, 181 (2009).
- [143] T. Steinmetz et al., “Stable fiber-based Fabry-Pérot cavity”, *Applied Physics Letters* **89**, 111110 (2006).
- [144] D. Hunger et al., “A fiber Fabry-Perot cavity with high finesse”, *New Journal of Physics* **12**, 065038 (2010).
- [145] E. Waks and C. Monroe, “Protocol for hybrid entanglement between a trapped atom and a quantum dot”, *Physical Review A* **80**, 062330 (2009).
- [146] R. Raussendorf and H. J. Briegel, “A One-Way Quantum Computer”, *Physical Review Letters* **86**, 5188 (2001).
- [147] L.-M. Duan and C. Monroe, *Robust Probabilistic Quantum Information Processing with Atoms, Photons, and Atomic Ensembles*, volume 55 of *Advances in Atomic, Molecular, and Optical Physics*, pages 419–464, Academic Press, 2007.
- [148] S. M. Tan, “A computational toolbox for quantum and atomic optics”, *Journal of Optics B: Quantum and Semiclassical Optics* **1**, 424 (1999).